

AD-A239 329

## MENTATION PAGE

Form Approved  
OMB No. 0704-0188

estimated to average 1 hour per response, including the time for reviewing instructions, searching existing data sources, gathering and reviewing the collection of information. Send comments regarding this burden estimate or any other aspect of this collection of information, including suggestions for reducing this burden, to Washington Headquarters Services, Directorate for Information Operations and Reports, 1215 Jefferson Avenue, Washington, DC 20540.

1. AGENCY USE ONLY (Leave blank)		2. REPORT DATE May 1991	3. REPORT TYPE AND DATES COVERED THESIS/DISSERTATION	
4. TITLE AND SUBTITLE A Time Dependent Transport Equation Solver			5. FUNDING NUMBERS	
6. AUTHOR(S) Lennard W. Lee, Jr., Captain				
7. PERFORMING ORGANIZATION NAME(S) AND ADDRESS(ES) AFIT Student Attending: University of New Mexico			8. PERFORMING ORGANIZATION REPORT NUMBER AFIT/CI/CIA-91-001d	
9. SPONSORING/MONITORING AGENCY NAME(S) AND ADDRESS(ES) AFIT/CI Wright-Patterson AFB OH 45433-6583			10. SPONSORING/MONITORING AGENCY REPORT NUMBER	
11. SUPPLEMENTARY NOTES				
12a. DISTRIBUTION/AVAILABILITY STATEMENT Approved for Public Release IAW 190-1 Distributed Unlimited ERNEST A. HAYGOOD, 1st Lt, USAF Executive Officer			12b. DISTRIBUTION CODE	
13. ABSTRACT (Maximum 200 words)				
30 91-07338 				
14. SUBJECT TERMS			15. NUMBER OF PAGES 137	
			16. PRICE CODE	
17. SECURITY CLASSIFICATION OF REPORT	18. SECURITY CLASSIFICATION OF THIS PAGE	19. SECURITY CLASSIFICATION OF ABSTRACT	20. LIMITATION OF ABSTRACT	

Title of Dissertation: A Time Dependent Transport Equation Solver

Performed by: Lennard Woodrow Lee, Junior  
Captain, USAF

Degree Awarded: May, 1991

University: The University of New Mexico

Number of pages of dissertation: 137

Degree Awarded: Doctor of Philosophy in Nuclear Engineering

Sub 1 A new time dependent neutron and photon transport code was developed. The code, FMP2DT (Finite element, Multigroup,  $P_n$ , 2-Dimensional, Time dependent), was discretized in space using finite elements, discretized in energy using a multi-group approximation, and discretized in time using Euler's backward differencing scheme. Its angular flux dependency was discretized using spherical harmonics. A  $P_1$  angular flux approximation allows some modeling of both anisotropic flux behavior and wave behavior. FMP2DT can model radiation transport in XZ slab or RZ cylindrical geometry. An inherently stable iteration solution scheme, an incomplete Cholesky conjugate gradient algorithm, calculates the total flux coefficients. FMP2DT was benchmarked against exact flux calculations in infinite XZ and RZ geometries. Two problems were solved by FMP2DT which involved the observation of the flux decay after injection of an inhomogeneous pulsed source to the configurations. A nuclear reactor, initially critical, had a pulsed source introduced at its center. This is typically done in so called Rossi-alpha experiments. FMP2DT showed that time must be allowed so that only the fundamental mode is dominant or the flux data will not yield credible information to calculate alpha. A uranium borehole problem was solved where FMP2DT showed that a counting instrument must be calibrated for different distances from a pulsed source because the flux decays with a different decay constant for each spatial point. Previous models did not account for this diffusion effect.



Acquisition For	
DTIC	<input checked="" type="checkbox"/>
DTIC	<input type="checkbox"/>
DTIC	<input type="checkbox"/>
Distribution/	
Availability Codes	
Avail and/or	
Dist	Special
A-1	

## A Time Dependent Transport Equation Solver

Lennard Woodrow Lee, Junior

B.S. Nuclear Engineering, Mississippi State Univ., 1983

M.S. Nuclear Engineering, Univ. of New Mexico, 1987

Ph.D. Nuclear Engineering, Univ. of New Mexico, 1991

The need for a new time dependent neutron and gamma radiation transport code that can model some anisotropic flux characteristics, have a flexible spatial discretization for different geometries, have the ability to model strong energy dependency, possess an inherently stable scheme for time discretization, and use a stable iteration algorithm led to the development of FMP2DT (Finite element, Multigroup,  $P_n$ , 2-Dimensional, Time dependent). Using spherical harmonics to discretize the flux's angular dependency, a  $P_1$  angular flux approximation was made to model anisotropic flux behavior. Finite elements were used to discretize its spatial dependency. The Galerkin procedure was used to develop the finite element equations for both XZ slab and RZ cylindrical geometries. An implicit method, Euler's backward differencing scheme, was used to discretize in time to insure time step stability. A multigroup approximation allows modeling systems that have a strong energy dependency. The source options include fission, inhomogeneous sources, and delayed neutrons. Gamma sources may be independent inhomogeneous sources or the result of particle interactions. The solution algorithm used invokes an incomplete Cholesky conjugate gradient method, which has inherent numerical stability. FMP2DT was benchmarked for both slab and cylindrical geometries. Two problems were selected to demonstrate FMP2DT's applicability. Both involved the observation of the neu-

tron flux decay after pulsing a source. First, the UNM AGN-201 reactor, initially at a critical state, was subjected to a pulsed neutron source at its center. The spatial decay of the neutron flux was observed to determine the time in which the fundamental mode begins to dominate. This information is important for what is called Rossi-alpha experiments because it indicates the proper time to gate counters so that data is not influenced by higher modes. Second, a uranium logging problem was addressed. A 14 MeV neutron source was turned on for 10 microseconds and the flux decay at differing spatial points was observed. This information showed that the counters need to be calibrated for different distances from the source because a distinct flux decay behavior was observed at each spatial calculation. For both problems, FMP2DT showed that knowledge of the flux decay physics is important to obtain accurate counting data.

## Abstract

The need for a new time dependent neutron and gamma radiation transport code that can model some anisotropic flux characteristics, have a flexible spatial discretization for different geometries, have the ability to model strong energy dependency, possess an inherently stable scheme for time discretization, and use a stable iteration algorithm led to the development of FMP2DT (Finite element, Multigroup,  $P_n$ , 2-Dimensional, Time dependent). Using spherical harmonics to discretize the flux's angular dependency, a  $P_1$  angular flux approximation was made to model anisotropic flux behavior. Finite elements were used to discretize its spatial dependency. The Galerkin procedure was used to develop the finite element equations for both XZ slab and RZ cylindrical geometries. An implicit method, Euler's backward differencing scheme, was used to discretize in time to insure time step stability. A multigroup approximation allows modeling systems that have a strong energy dependency. The source options include fission, inhomogeneous sources, and delayed neutrons. Gamma sources may be independent inhomogeneous sources or the result of particle interactions. The solution algorithm used invokes an incomplete Cholesky conjugate gradient method, which has inherent numerical stability. FMP2DT was benchmarked for both slab and cylindrical geometries. Two problems were selected to demonstrate FMP2DT's applicability. Both involved the observation of the neutron flux decay after pulsing a source. First, the UNM AGN-201 reactor, initially at a critical state, was subjected to a pulsed neutron source at its center. The spatial decay of the neutron flux was observed to determine the time in which the fundamental mode begins to dominate. This information is important for what is called Rossi-alpha experiments because it indicates the proper time to gate counters so that data is not influenced by higher modes. Second, a uranium logging problem

was addressed. A 14 MeV neutron source was turned on for 10 microseconds and the flux decay at differing spatial points was observed. This information showed that the counters need to be calibrated for different distances from the source because a distinct flux decay behavior was observed at each spatial calculation. For both problems, FMP2DT showed that knowledge of the flux decay physics is important to obtain accurate counting data.

### CERTIFICATION OF FINAL FORM

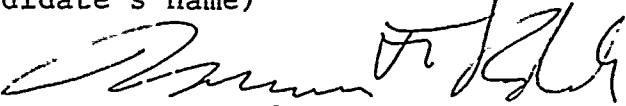
Each thesis or dissertation, when submitted to the Graduate School, must be accompanied by this form, signed by the director or other person designated by the dissertation or thesis committee.

The signature on this certification affirms that the dissertation or thesis is in proper final form, with any suggested changes having been incorporated, and is in essentially perfect condition as regards its physical presentation, ready for binding and microfilming. The dissertation or thesis is complete, properly arranged, without errors in the use of language (grammar, spelling, punctuation), and without flaws in typing and reproduction (i.e., it is accurate, clean, uniform, with adequate margins, etc.).

---

To the Graduate Dean:

I have read, in its final form, the \_\_\_\_\_ Ph.D. dissertation/  
~~Master's thesis~~ of Lennard W. Lee Jr., and certify  
(candidate's name)  
it as described above.

  
\_\_\_\_\_  
Signature

15 Aug 91  
\_\_\_\_\_  
Date

Lennard Woodrow Lee, Junior

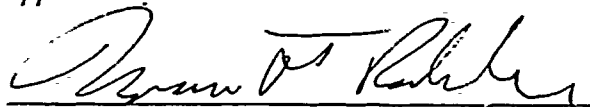
*Candidate*

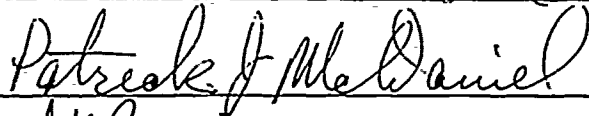
Chemical and Nuclear Engineering

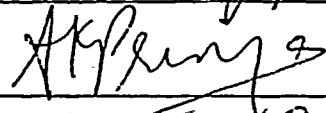
*Department*

This dissertation is approved, and it is acceptable in quality and form for publication on microfilm:

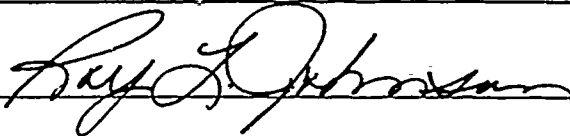
*Approved by the Dissertation Committee:*

 , Chairperson









Accepted:

*Dean, Graduate School*

*Date*



A TIME DEPENDENT TRANSPORT EQUATION SOLVER

BY

LENNARD WOODROW LEE, JUNIOR

B.S., Mississippi State University, 1983

M.S., University of New Mexico, 1987

DISSERTATION

Submitted in Partial Fulfillment of the  
Requirements for the Degree of  
Doctor of Philosophy in Engineering

The University of New Mexico  
Albuquerque, New Mexico

May, 1991

## Acknowledgements

When I attempt to take inventory of the individuals that have been helpful with this effort, the list seems to grow endlessly. However, I would like to take this time to express my sincere appreciation to some of those individuals. First, and most important, my thanks goes to my wife, Sabrina, whose support and encouragement was invaluable. While I sweated by a computer terminal or was doing some other endless computation, she took upon herself to bear many domestic duties that normally would have been mine. Without her contributions and love, this work would not have been completed. My children were the paramount reason I attempted this. It is my hope that Matthew, Michael, Mark, and John will have their lives enhanced somehow because of their father's achievements. If so, this work will be more than worth it.

My thanks go to all my committee members. They are Dr. Norman Roderick, Dr. Anil Prinja, Dr. Robert Busch, Dr. Roy Johnson, and Dr. Patrick J. McDaniel. Special thanks to Dr. Norman Roderick, my committee chairman. There is no way I can express my thanks to Dr. Patrick McDaniel, who was my principal advisor for both my Master's and Ph.D. research. He made invaluable resources available to me at Sandia National Laboratories. Dr. McDaniel has a special commitment to academic achievement, and I appreciate that very much.

I would also like to thank both Dr. John I. Paulk and Dr. Charles S. Sparrow at Mississippi State University, because, if it were not for them, my education would have terminated years ago. Dr. Sparrow also provided some encouragement and support for my Master's and Ph.D. work, and has become a special friend to my family and myself over the years.

I know that my parent's prayers were significant. I would like thank my mother,

Mrs. Bobbie Lee, for her countless periods of encouragement. For my father, who has been very sick for many years, I hope that this achievement will cheer him up, and make him somewhat better. To my sister, Deborah Lee, I hope this will encourage her to continue her drive for more formal education. My mother-in-law, Mrs. Carman Rodriguez, has also been a source of encouragement, and I appreciate it.

Two very important organizations deserve thanks. It is without saying that this work could not have been done without the sponsorship of the United States Air Force through the Air Force Institute of Technology's Civilian Institution Program. To the United States Department of Energy and Sandia National Laboratories, a special thanks for use of their resources.

Finally, it is my opinion, that there was help beyond people and their organizations. My belief is that a Being greater than all was with me throughout. As a result of this work, my faith in Him has grown, and my hope is to use all of this wisely for Him. I know that God has truly blessed me. Taking a thought from a song I heard lately; *He must increase, and I must decrease; in my own eyes.* This is my continuing prayer.

A TIME DEPENDENT TRANSPORT EQUATION SOLVER

BY

LENNARD WOODROW LEE, JUNIOR

ABSTRACT OF DISSERTATION

Submitted in Partial Fulfillment of the  
Requirements for the Degree of

Doctor of Philosophy in Engineering

The University of New Mexico  
Albuquerque, New Mexico

May, 1991

## A Time Dependent Transport Equation Solver

Lennard Woodrow Lee, Junior

B.S. Nuclear Engineering, Mississippi State Univ., 1983

M.S. Nuclear Engineering, Univ. of New Mexico, 1987

Ph.D. Nuclear Engineering, Univ. of New Mexico, 1991

The need for a new time dependent neutron and gamma radiation transport code that can model some anisotropic flux characteristics, have a flexible spatial discretization for different geometries, have the ability to model strong energy dependency, possess an inherently stable scheme for time discretization, and use a stable iteration algorithm led to the development of FMP2DT (Finite element, Multigroup,  $P_n$ , 2-Dimensional, Time dependent). Using spherical harmonics to discretize the flux's angular dependency, a  $P_1$  angular flux approximation was made to model anisotropic flux behavior. Finite elements were used to discretize its spatial dependency. The Galerkin procedure was used to develop the finite element equations for both XZ slab and RZ cylindrical geometries. An implicit method, Euler's backward differencing scheme, was used to discretize in time to insure time step stability. A multigroup approximation allows modeling systems that have a strong energy dependency. The source options include fission, inhomogeneous sources, and delayed neutrons. Gamma sources may be independent inhomogeneous sources or the result of particle interactions. The solution algorithm used invokes an incomplete Cholesky conjugate gradient method, which has inherent numerical stability. FMP2DT was benchmarked for both slab and cylindrical geometries. Two problems were selected to demonstrate FMP2DT's applicability. Both involved the observation of the neu-

tron flux decay after pulsing a source. First, the UNM AGN-201 reactor, initially at a critical state, was subjected to a pulsed-neutron source at its center. The spatial decay of the neutron flux was observed to determine the time in which the fundamental mode begins to dominate. This information is important for what is called Rossi-alpha experiments because it indicates the proper time to gate counters so that data is not influenced by higher modes. Second, a uranium logging problem was addressed. A 14 MeV neutron source was turned on for 10 microseconds and the flux decay at differing spatial points was observed. This information showed that the counters need to be calibrated for different distances from the source because a distinct flux decay behavior was observed at each spatial calculation. For both problems, FMP2DT showed that knowledge of the flux decay physics is important to obtain accurate counting data.

# Contents

Acknowledgements	iii
Abstract	vi
List of Figures	x
List of Tables	xii
Nomenclature	xiii
<b>1 Introduction</b>	<b>1</b>
1.1 Research Objectives . . . . .	1
1.2 Literature Search . . . . .	3
1.3 Importance . . . . .	5
<b>2 The Time Dependent Transport Equation</b>	<b>6</b>
<b>3 Solution in XZ Geometry</b>	<b>9</b>
3.1 The $P_1$ Approximation . . . . .	14
3.2 The Multigroup Approximation . . . . .	16
3.3 Time Discretization: Euler's Backward Differencing . . . . .	17
3.4 Finite Element Implementation . . . . .	20
3.5 Finite Element Discretization for XZ Geometry . . . . .	22
3.6 Coefficient Matrix Example . . . . .	35
<b>4 Solution in RZ Geometry</b>	<b>39</b>
4.1 RZ Finite Element Discretization . . . . .	42
<b>5 Solution Technique</b>	<b>50</b>

<b>6</b>	<b>Calculation of <math>\chi_k^g</math></b>	<b>52</b>
<b>7</b>	<b>Code Benchmark</b>	<b>58</b>
7.1	TWIGL Comparison . . . . .	58
7.1.1	Transient Calculations . . . . .	65
7.2	Slab Geometry Benchmark . . . . .	73
7.3	Infinite Cylindrical Geometry Benchmark . . . . .	84
7.4	Benchmark Conclusions . . . . .	93
<b>8</b>	<b>FMP2DT Applications</b>	<b>95</b>
8.1	AGN-201 Rossi-Alpha Problem . . . . .	95
8.1.1	AGN Calculation Description . . . . .	96
8.1.2	AGN Results . . . . .	97
8.2	Uranium Logging Problem . . . . .	100
8.2.1	Logging Calculation Description . . . . .	101
8.2.2	Logging Problem Results . . . . .	101
<b>9</b>	<b>Conclusions</b>	<b>104</b>
9.1	Future Research . . . . .	105
	<b>Appendix A: Vector and Matrix Definitions</b>	<b>107</b>
	<b>Appendix B: Integrating Summaries</b>	<b>111</b>
	<b>Appendix C: TWIGL Cross Section Data</b>	<b>118</b>



## List of Figures

1	Linear $B$ Splines . . . . .	23
2	Two Dimensional Slab Geometry . . . . .	25
3	Two Dimensional Slab Mesh Point Layout Example . . . . .	37
4	Spatial Matrix Example . . . . .	38
5	Cylindrical Geometry . . . . .	39
6	Prompt Group $\chi$ for $^{235}\text{U}$ . . . . .	56
7	Delay Group $\chi$ for $^{235}\text{U}$ . . . . .	57
8	TWIGL Slab Geometry . . . . .	59
9	Initial TWIGL Flux . . . . .	62
10	Initial FEMP2D Flux Using TWIGL Mesh Spacing . . . . .	63
11	Initial FEMP2D Flux Using 2X TWIGL Mesh Spacing . . . . .	64
12	Time Dependent Thermal Absorption . . . . .	65
13	TWIGL Flux at Time $t = 0.01$ sec . . . . .	70
14	FMP2DT Flux With TWIGL Mesh; $t = 0.01$ sec . . . . .	71
15	FMP2DT Flux With 2X TWIGL Mesh; $t = 0.01$ sec . . . . .	72
16	FMP2DT and Exact Flux, XZ Geometry 1 MFP From Boundary . .	78
17	FMP2DT and Exact Flux, XZ Geometry 2 MFPs From Boundary .	79
18	FMP2DT and Exact Flux, XZ Geometry 3 MFPs From Boundary .	80
19	FMP2DT and Exact Flux, XZ Geometry 4 MFPs From Boundary .	81
20	FMP2DT and Exact Flux, XZ Geometry 5 MFPs From Boundary .	82
21	FMP2DT and Exact Flux, XZ Geometry 6 MFPs From Boundary .	83
22	FMP2DT and Exact Flux, RZ Geometry 1 MFP From Boundary . .	87
23	FMP2DT and Exact Flux, RZ Geometry 2 MFPs From Boundary .	88
24	FMP2DT and Exact Flux, RZ Geometry 3 MFPs From Boundary .	89

25	FMP2DT and Exact Flux, RZ Geometry 4 MFPs From Boundary .	90
26	FMP2DT and Exact Flux, RZ Geometry 5 MFPs From Boundary .	91
27	FMP2DT and Exact Flux, RZ Geometry 6 MFPs From Boundary .	92
28	AGN Geometry . . . . .	98
29	Flux Decay for the AGN-201 Reactor . . . . .	99
30	Logging Geometry . . . . .	102
31	Flux Decay for the Logging Problem . . . . .	103
32	Piece-Wise Material Matrix Example . . . . .	113

## List of Tables

1	Part 1: 47 Neutron Group Structure . . . . .	54
2	Part 2: 47 Neutron Group Structure . . . . .	55
3	TWIGL and FMP2DT Initial Fast Fluxes . . . . .	60
4	Material Mean Free Paths . . . . .	61
5	Coolant Temperatures by Zone . . . . .	66
6	TWIGL Flux at Time $t = 0.01$ sec . . . . .	67
7	FMP2DT Run Summary for TWIGL Comparison . . . . .	68
8	Exact Flux Due to an Isotropic Pulsed Plane Source at $x = 0$ in a Nonabsorbing Infinite Medium For Slab Geometry . . . . .	75
9	FMP2DT Flux Due to an Isotropic Pulsed Plane Source at $x = 0$ in a Nonabsorbing Medium For Slab Geometry . . . . .	76
10	The Percent Relative Error for the FMP2DT Slab Calculations . . . .	77
11	Run Summary for the Infinite Slab and Cylindrical Geometries . . . .	77
12	Exact Flux Due to an Isotropic Pulsed Plane Source at $r = 0$ in a Nonabsorbing Infinite Medium For RZ Geometry . . . . .	85
13	FMP2DT Flux Due to an Isotropic Pulsed Plane Source at $r = 0$ in a Nonabsorbing Infinite Medium For RZ Geometry . . . . .	85
14	The Percent Relative Error for the FMP2DT Cylindrical Calculations	86
15	Three Group Energy Structure . . . . .	97

## Nomenclature

$\Psi(\mathbf{r}, E, \Omega, t)$	the angular flux at $\mathbf{r}$ in direction $\Omega$ with energy $E$ at time $t$ .
$S_{in}(\mathbf{r}, E, \Omega, t)$	the inhomogeneous neutron source at position $\mathbf{r}$ , emitting neutrons with energy $E$ in a direction $\Omega$ , at a time $t$ .
$\Sigma_t(\mathbf{r}, E)$	the total cross section, corresponding to neutron interactions involving neutrons with energy $E$ .
$\Sigma_s(\mathbf{r}, E' \rightarrow E, \Omega' \rightarrow \Omega)$	the inscattering probability (cross section) that neutrons with energy $E'$ moving in direction $\Omega'$ will scatter into energy $E$ and direction $\Omega$ .
$\chi_p(E)$	the probability that a prompt neutron (born from fission) will have an energy $E$ .
$\beta$	the fraction of neutrons from a delayed source (precursor decay).
$\chi_k(E)$	the probability that a delayed neutron born from precursor decay in the $k^{\text{th}}$ family group (also referred to as precursor species) will have energy $E$ .
$\lambda_k$	the decay constant for the $k^{\text{th}}$ precursor group.
$C_k(\mathbf{r}, t)$	the concentration of the $k^{\text{th}}$ precursor species at position $\mathbf{r}$ and at time $t$ .
$v$	the neutron velocity.
$\Omega$	the neutron direction.
$\nu$	the average neutrons emitted per fission from a fissile isotope.
$\Sigma_f(\mathbf{r}, E')$	the fission cross section at position $\mathbf{r}$ and energy $E'$ .

$P_l^m(\cos \theta)$	associated Legendre function of degree $l$ and order $m$ .
$\theta$	the polar angle measured from a direction coordinate axis in an orthogonal coordinate system.
$\phi$	the azimuthal angle stipulating the rotation around the chosen directed coordinate axis that $\theta$ is measured from.
$l, m$	the subscripts or superscripts for the spherical harmonic expansion.
$(N + 1)$	the time discretization superscript representing the present time step.
$(N)$	the time discretization superscript representing the last time step.
$g = 1, 2, \dots, G$	the energy groups. $g = 1$ represents the highest energy group, and $g = G$ is the lowest (thermal) energy group.
$\psi_{00}(\mathbf{r}, E, t)$	the coefficient in the $P_1$ approximation that physically represents the total flux in $\Psi(\mathbf{r}, E, \Omega, t)$ .
$\psi_{10}(\mathbf{r}, E, t)$	the coefficient in the $P_1$ approximation of $\Psi(\mathbf{r}, E, \Omega, t)$ physically representing the component of current in the $z$ direction.
$\psi_{11}(\mathbf{r}, E, t)$	the coefficient in the $P_1$ approximation of $\Psi(\mathbf{r}, E, \Omega, t)$ physically representing the component of current in the $x$ direction in XZ geometry or the current in the $r$ direction in RZ geometry.
$S_{00}$	the inhomogeneous isotropic source.
$S_{10}, S_{11}$	inhomogeneous anisotropic sources.
$B_p(x), B_q(z), B_q(r)$	linear interpolating hat functions.

$\Psi_{00}^{(N+1)}, \Psi_{00}^{(N)}$   $G \times 1$  vectors containing  $\psi_{00}^g$  expansion coefficients at a given mesh point.

$\Psi_{10}^{(N+1)}, \Psi_{10}^{(N)}$   $G \times 1$  vectors containing  $\psi_{10}^g$  expansion coefficients at a given mesh point.

$\Psi_{11}^{(N+1)}, \Psi_{11}^{(N)}$   $G \times 1$  vectors containing  $\psi_{11}^g$  expansion coefficients at a given mesh point.

$S_{00}^{(N+1)}$  a  $G \times 1$  vector containing  $S_{00}^g$  coefficients at a given mesh point.

$S_{10}^{(N+1)}, S_{11}^{(N+1)}$   $G \times 1$  vectors containing  $S_{10}^g$  and  $S_{11}^g$  coefficients at a given mesh point.

UNM The University of New Mexico

# 1 Introduction

Interest in nuclear power for both space exploration and terrestrial use has increased in the technical community in the recent years. Potential space missions that will demand dependable power levels beyond conventional sources are now being considered with new enthusiasm. President Bush has recently expressed his desires for the nation to become committed to putting a space station in orbit and developing a lunar base that will act as stage for the exploration of Mars. There are suggestions within the civilian community that the development of manufacturing plants in space is receiving strong consideration. Nuclear power is seen as a feasible source of the energy needed to accomplish these goals.

Likewise, developing strong concerns of possible greenhouse effects from using fossil fuels is renewing interest in developing small terrestrial nuclear reactors with passive safety designs. Even some established critics of nuclear power suggest that nuclear power would be acceptable if reactor designs with new passive safety features are developed. It is evident that nuclear reactors will be included in future energy considerations.

Therefore, development of new analytic tools is desirable to enhance reactor designs. This research resulted in developing a new finite element code which will be used in reactor design, development, and analysis, or for any time dependent radiation transport problem defined in XZ or RZ geometries.

## 1.1 Research Objectives

The object of this research was the development of a new neutron and gamma radiation transport code with the following characteristics. It must be able solve two

dimensional time dependent problems in either XZ slab or RZ cylindrical geometry. The angular flux must be defined so that some anisotropic flux behavior can be modeled. The spatial discretization must be adaptable to both XZ and RZ geometries, as well as future options that may be incorporated later. The code must have the ability to model systems that have strong energy dependency. And finally, if a system is modeled involving one or more fissile isotopes, the source must include a delayed neutron contribution.

The code will be used to investigate the following:

- a. Neutron wave effects.
- b. Spatially dependent subcritical and critical source driven transients.
- c. The effect on accuracy of tradition approximations in solving time dependent transport problems. This will include comparisons with:
  - i. The diffusion approximation.
  - ii. Treatment of the fission source.
  - iii. Treatment of upscatter.

The code will then be benchmarked and some few-group problems identified and solved that demonstrate the code's validity and applicability.

FMP2DT (Finite element, Multigroup,  $P_n$ , 2-Dimensional, Time dependent) was developed to met these objectives. It solves time dependent neutron and/or gamma radiation transport problems in XZ and RZ geometries. Finite elements were selected to implement spatial discretization, and the time discretization was done using Euler's backward differencing scheme.

The finite element scheme is employed by expanding the solution of a set of local partial differential equations with a set of basis, or interpolating functions. Using the Galerkin procedure, interpolating and weighting functions were chosen that adapt to both of the stated geometries, or any geometry option added later, no matter how irregular it may be. The finite element method has a firm theoretical foundation



which guarantees convergence of the approximate solution [Ref. 4].

Euler's backward differencing method was used for the time discretization. This is an implicit scheme that is numerically stable for any time step [Ref.3] [Ref. 26].

The angular dependency of the angular neutron flux was modeled using spherical harmonics. Spherical harmonics form a complete set of functions that describe the angular dependency of the neutron direction [Ref. 1]. Spherical harmonics yield solution results of arbitrarily high degrees of accuracy depending on the expenditure of labor to do the resulting calculations [Ref. 2]. At least a  $P_1$  approximation is a necessary requirement to observe neutron wave behavior and model some anisotropic behavior of the flux. All of this applies to the gamma flux also. Therefore it was modeled likewise.

## 1.2 Literature Search

A literature search conducted in July 1989 revealed no previous finite element neutron code developments with delayed neutron sources and inhomogeneous sources. There are numerous codes that model time dependency with other discretization characteristics.

Kinetics codes are available with numerous finite differencing schemes. Monte Carlo codes are available in which a detailed spatial model of the reactor can be accomplished. All of these codes have legitimate applications where they have advantages over other methods. They also have their constraints. Monte Carlo codes require a statistical approach, and experience is needed to ensure validity for different reactor configurations. The finite differencing scheme is the most used solver. For stiff problems, mesh spacing can be complicated, and implementing various boundary conditions can be tedious.

The finite element code developed by this research is more flexible. The ap-

proximating, or interpolating, functions used in the code allows the incorporation of complicated geometries. Boundary conditions are carried with each finite element, and therefore somewhat easier to implement than for other schemes. In fact, implementation of the boundary conditions appears to be the most attractive feature of finite element solution schemes.

Finite element codes have been used in neutron transport codes for sometime. Several codes exist for steady state analysis. FEMP1D (Finite Element Multi-group  $P_n$  1-Dimensional) is a radiation transport code for infinite slab geometry. Buckling height corrections are needed to adjust for leakage. This code is very cost effective. FEMP2D is a two dimensional version which analyzes a steady state configuration. It is a  $P_1$  code designed to handle XZ, RZ and R $\theta$  geometries. Likewise, FEMP3D is three dimensional. These codes are all written for vector machines and are coded in FORTRAN 77.

PERT2D is a finite element perturbation code that models small changes in reactivity [Ref. 19]. A one dimensional, time dependent, finite element code, TDF1D, is also available, but it does not have a delayed neutron precursor source contribution [Ref. 25]. SHLDTEMP is a coupled radiation transport and temperature distribution code written at The University of New Mexico [Ref. 24].

J. K. Fletcher has suggested finite element options in some of his transport codes for steady state [Ref. 11]. Finite elements have been used to discretize the angular dependency of the neutron direction in other neutron codes. So the foundation for using finite elements in neutron transport is strong. However, the literature search did not reveal any previous finite element, spatially discretized, multidimensional transient codes. Therefore, the development of this new code had a strong theoretical foundation, and it contributes to the work previously done.

### 1.3 Importance

The importance of this effort is that a finite element code now exist for time dependent radiation transport and nuclear reactor analysis. The code is both relatively easy to set up and economical to use. Benchmarking shows that it achieves an acceptable degree of accuracy for XZ and RZ geometries. Delayed neutrons can now be modeled in the source terms. Although delayed neutrons have an extremely small population in reactors compared to prompt fission neutrons, their presence ensures that the reactor is controllable. Thus, developing a finite element code that considers their source contribution is a credible enhancement and contribution to the inventory of codes now available. This code will make a contribution to fundamental engineering knowledge. It is also a valuable stepping stone for the development of higher order approximations in future research.

## 2 The Time Dependent Transport Equation

Neutron transport theory is a mathematical expression which describes neutron interactions in a given medium. For any arbitrary volume, the time dependent neutron transport equation may be written in the following form:

$$\begin{aligned}
 & \frac{1}{v} \frac{\partial}{\partial t} \Psi(\mathbf{r}, E, \Omega, t) + \Omega \cdot \nabla \Psi(\mathbf{r}, E, \Omega, t) + \Sigma_t(\mathbf{r}, E) \Psi(\mathbf{r}, E, \Omega, t) \\
 &= \int_{E'} \int_{\Omega'} \Sigma_s(\mathbf{r}, E' \rightarrow E, \Omega' \rightarrow \Omega) \Psi(\mathbf{r}, E', \Omega', t) d\Omega' dE' \\
 &+ \frac{\chi_p(E)}{4\pi} (1 - \beta) \int_{E'} \int_{\Omega'} \nu \Sigma_f(\mathbf{r}, E') \Psi(\mathbf{r}, E', \Omega', t) d\Omega' dE' \\
 &+ \frac{1}{4\pi} \sum_{k=1}^n \chi_k(E) \lambda_k C_k(\mathbf{r}, t) + S_{in}(\mathbf{r}, E, \Omega, t)
 \end{aligned} \tag{1}$$

Where Equation (1) states the relationships between source and loss terms such that:

$$\begin{aligned}
 & \left\{ \begin{array}{l} \text{The time rate of change of} \\ \text{the neutron angular flux} \end{array} \right\} + \left\{ \begin{array}{l} \text{neutron} \\ \text{streaming} \end{array} \right\} + \left\{ \begin{array}{l} \text{total} \\ \text{interactions} \end{array} \right\} \\
 &= \left\{ \begin{array}{l} \text{neutron} \\ \text{inscattering} \end{array} \right\} + \left\{ \begin{array}{l} \text{prompt fission} \\ \text{neutrons} \end{array} \right\} + \left\{ \begin{array}{l} \text{delayed} \\ \text{neutrons} \end{array} \right\} \\
 &+ \left\{ \begin{array}{l} \text{inhomogeneous} \\ \text{sources} \end{array} \right\}.
 \end{aligned}$$

The streaming and total interaction variables represent loss terms, where the terms on the right hand side represent sources. The angular neutron flux,  $\Psi(\mathbf{r}, E, \Omega, t)$ , is a function of spatial variables incorporated in  $\mathbf{r}$ , neutron energy  $E$ , angular variables incorporated in  $\Omega$ , all of which are evaluated at time  $t$ .  $\Omega$  is represented by an azimuthal angle  $\phi$  and a polar angle  $\theta$  in an orthogonal coordinate system. The polar angle is usually described in terms of its cosine. A complete set of functions that describe the angular dependency of the neutron flux are spherical harmonics [Ref. 1]. For XZ and RZ geometry, with azimuthal symmetry, the angular flux

may be completely described with the spherical harmonic expansion as,

$$\Psi(\mathbf{r}, E, \Omega, t) = \sum_{l=0}^{\infty} \sum_{m=0}^l \frac{2l+1}{4\pi} P_l^m(\cos \theta) \psi_{lm}(\mathbf{r}, E, t) \cos(m\phi) \quad (2)$$

Likewise, the inhomogeneous source may be expanded as,

$$S_{in}(\mathbf{r}, E, \Omega, t) = \sum_{l=0}^{\infty} \sum_{m=0}^l \frac{2l+1}{4\pi} P_l^m(\cos \theta) S_{lm}(\mathbf{r}, E, t) \cos(m\phi) \quad (3)$$

$P_l^m(\cos \theta)$  are associated Legendre functions of degree  $l$  and order  $m$  [Ref. 5]. They are orthogonal on the interval  $\theta = 0$ , to  $\theta = \pi$  radians. They obey the recurrence relationships [Ref. 11]:

$$(2l+1) \cos \theta P_l^m(\cos \theta) = (l-m+1) P_{l+1}^m(\cos \theta) + (l+m) P_{l-1}^m(\cos \theta) \quad (4)$$

$$(2l+1) \sin \theta P_l^m(\cos \theta) = P_{l+1}^{m+1}(\cos \theta) - P_{l-1}^{m+1}(\cos \theta) \quad (5)$$

$$(2l+1) \sin \theta P_l^m(\cos \theta) = (l+m)(l+m-1) P_{l-1}^{m-1}(\cos \theta) - (l-m+1)(l-m+2) P_{l+1}^{m-1}(\cos \theta) \quad (6)$$

The streaming term in Equation (1) is  $\Omega \cdot \nabla \Psi(\mathbf{r}, E, \Omega, t)$ . This term is a representation of the rate of change of the neutron's angular flux along a streaming path [Ref. 12]. The  $\Omega \cdot \nabla$  term is sensitive to the geometry in question. For XZ geometry, it is defined as,

$$\Omega \cdot \nabla = \cos \theta \frac{\partial}{\partial z} + \sin \theta \cos \phi \frac{\partial}{\partial x} \quad (7)$$

For RZ geometry, with symmetry in its azimuthal coordinate, it is defined as,

$$\Omega \cdot \nabla = \cos \theta \frac{\partial}{\partial z} + \sin \theta \cos \phi \frac{\partial}{\partial r} - \frac{\sin \theta \sin \phi}{r} \frac{\partial}{\partial \phi} \quad (8)$$

The inscattering probability (or cross section) in Equation (1) may be represented as

$$\Sigma_s(\mathbf{r}, E' \rightarrow E, \Omega' \rightarrow \Omega) = \sum_{l=0}^{\infty} \frac{2l+1}{4\pi} \Sigma_{s,l}(\mathbf{r}, E' \rightarrow E) P_l(\Omega' \cdot \Omega) \quad (9)$$

By the addition theorem [Ref. 6], we may write

$$P_l(\Omega' \cdot \Omega) = P_l(\cos \theta) P_l(\cos \theta') + 2 \sum_{m=1}^l \frac{(l-m)!}{(l+m)!} P_l^m(\cos \theta) P_l^m(\cos \theta') \cos[m(\phi - \phi')] \quad (10)$$

Therefore the inscatter cross section may be expressed as,

$$\Sigma_s(\mathbf{r}, E' \rightarrow E, \Omega' \rightarrow \Omega) = \sum_{l=0}^{\infty} \frac{2l+1}{4\pi} \Sigma_{s_l} \left\{ P_l(\cos \theta) P_l(\cos \theta') + 2 \sum_{m=1}^l \frac{(l-m)!}{(l+m)!} P_l^m(\cos \theta) P_l^m(\cos \theta') \cos[m(\phi - \phi')] \right\} \quad (11)$$

Exact solutions to Equation (1) are possible in only a few special cases. In practice, approximations are made to the transport equation to generate solutions that are accurate enough for specific physical interaction processes. We now consider the development of an approximate solution to the transport equation for XZ slab geometry.

### 3 Solution in XZ Geometry

To get an approximate solution to the transport equation in XZ geometry, the correct substitutions shown above are implemented into Equation (1). The transport equation is then transformed into the following form:

$$\begin{aligned}
 & \frac{1}{v} \frac{\partial}{\partial t} \sum_{l=0}^{\infty} \sum_{m=0}^l \frac{2l+1}{4\pi} P_l^m(\cos \theta) \psi_{lm} \cos(m\phi) \\
 & + \cos \theta \frac{\partial}{\partial z} \sum_{l=0}^{\infty} \sum_{m=0}^l \frac{2l+1}{4\pi} P_l^m(\cos \theta) \psi_{lm} \cos(m\phi) \\
 & + \sin \theta \cos \phi \frac{\partial}{\partial x} \sum_{l=0}^{\infty} \sum_{m=0}^l \frac{2l+1}{4\pi} P_l^m(\cos \theta) \psi_{lm} \cos(m\phi) \\
 & + \Sigma_t \sum_{l=0}^{\infty} \sum_{m=0}^l \frac{2l+1}{4\pi} P_l^m(\cos \theta) \psi_{lm} \cos(m\phi) \\
 & = \int_{E'} \int_{\Omega'} \sum_{l=0}^{\infty} \frac{2l+1}{4\pi} \Sigma_{s_l} P_l(\cos \theta) P_l(\cos \theta') \\
 & \quad \cdot \sum_{l=0}^{\infty} \sum_{m=0}^l \frac{2l+1}{4\pi} P_l^m(\cos \theta') \psi_{lm} \cos(m\phi') d\Omega' dE' \\
 & + \int_{E'} \int_{\Omega'} \sum_{l=0}^{\infty} \frac{2l+1}{4\pi} \Sigma_{s_l} (2) \sum_{m=1}^l \frac{(l-m)!}{(l+m)!} P_l^m(\cos \theta) P_l^m(\cos \theta') \cos[m(\phi - \phi')] \\
 & \quad \cdot \sum_{l=0}^{\infty} \sum_{m=0}^l \frac{2l+1}{4\pi} P_l^m(\cos \theta') \psi_{lm} \cos(m\phi') d\Omega' dE' \\
 & + \frac{\chi_p}{4\pi} (1 - \beta) \int_{E'} \int_{\Omega'} \nu \Sigma_f \sum_{l=0}^{\infty} \sum_{m=0}^l \frac{2l+1}{4\pi} P_l^m(\cos \theta') \psi_{lm} \cos(m\phi') d\Omega' dE' \\
 & + \sum_{l=0}^{\infty} \sum_{m=0}^l \frac{2l+1}{4\pi} P_l^m(\cos \theta) S_{lm} \cos(m\phi) \\
 & + \frac{1}{4\pi} \sum_{k=1}^n \chi_k \lambda_k C_k
 \end{aligned} \tag{12}$$

Equation (12) can be immediately simplified by defining fission as an isotropic event. This has been shown to be experimentally correct [Ref. 7], and it sets  $l = m = 0$  in the fission term. Some of the  $\Omega'$  terms can also be simplified by integrating

over all directions. This integration is defined as,

$$\int_{\Omega'} d\Omega' = \int_{\pi}^0 \int_0^{2\pi} d\phi' d(\cos \theta') = 4\pi \quad (13)$$

and, it can be immediately used in both the fission and inscattering terms. Associated Legendre functions are orthogonal. Integration of these functions is defined as,

$$\int_{\pi}^0 P_l^m(\cos \theta) P_K^N(\cos \theta) d(\cos \theta) = \frac{2}{2l+1} \frac{(l+m)!}{(l-m)!} \delta_{lK} \delta_{mN} \quad (14)$$

where  $\delta_{lK}$  and  $\delta_{mN}$  are Kronecker delta functions. Since  $P_0^0(\cos \theta) = 1.0$ , multiplying any term in Equation (12) by  $P_0^0(\cos \theta)$  will not change the equation's value. To implement orthogonality (at a later time), the precursor term and the fission source term can be multiplied by  $P_0^0(\cos \theta)$ . Using the above information yields,

$$\begin{aligned} & \frac{1}{v} \frac{\partial}{\partial t} \sum_{l=0}^{\infty} \sum_{m=0}^l (2l+1) P_l^m(\cos \theta) \psi_{lm} \cos(m\phi) \\ & + \sum_{l=0}^{\infty} \sum_{m=0}^l (2l+1) \cos \theta P_l^m(\cos \theta) \frac{\partial \psi_{lm}}{\partial z} \cos(m\phi) \\ & + \sum_{l=0}^{\infty} \sum_{m=0}^l (2l+1) \sin \theta P_l^m(\cos \theta) \frac{\partial \psi_{lm}}{\partial x} \cos(m\phi) \cos \phi \\ & + \Sigma_t \sum_{l=0}^{\infty} \sum_{m=0}^l (2l+1) P_l^m(\cos \theta) \psi_{lm} \cos(m\phi) \\ & = \int_{E'} \sum_{l=0}^{\infty} (2l+1) \Sigma_{s_l} P_l(\cos \theta) \sum_{l=0}^{\infty} \psi_{l0} dE' \\ & + \int_{E'} \sum_{l=1}^{\infty} (2l+1) \Sigma_{s_l} P_l^m(\cos \theta) \sum_{l=1}^{\infty} \sum_{m=1}^l \psi_{lm} \cos(m\phi) dE' \\ & + \chi_p (1-\beta) \int_{E'} \nu \Sigma_f \psi_{00} dE' P_0^0(\cos \theta) \\ & + \sum_{l=0}^{\infty} \sum_{m=0}^l (2l+1) P_l^m(\cos \theta) S_{lm} \cos(m\phi) \\ & + \sum_{k=1}^n \chi_k \lambda_k C_k P_0^0(\cos \theta) \end{aligned} \quad (15)$$

Note:  $P_l^m(\cos \theta) = P_l(\cos \theta)$  if  $m = 0$ . The following trigonometric identity may



now be implemented:

$$\cos(m\phi) \cos \phi = \frac{1}{2} \cos(m+1)\phi + \frac{1}{2} \cos(m-1)\phi \quad (16)$$

We can substitute Equation (16) and implement recurrence relations defined by Equations (4), (5), and (6) and manipulate so Equation (15) becomes,

$$\begin{aligned} & \frac{2}{v} \frac{\partial}{\partial t} \sum_{l=0}^{\infty} \sum_{m=0}^l (2l+1) P_l^m(\cos \theta) \psi_{lm} \cos(m\phi) \\ & + (2) \sum_{l=0}^{\infty} \sum_{m=0}^l (l-m+1) P_{l+1}^m(\cos \theta) \frac{\partial \psi_{lm}}{\partial z} \cos(m\phi) \\ & + (2) \sum_{l=0}^{\infty} \sum_{m=0}^l (l+m) P_{l-1}^m(\cos \theta) \frac{\partial \psi_{lm}}{\partial z} \cos(m\phi) \\ & + \sum_{l=0}^{\infty} \sum_{m=0}^l P_{l+1}^{m+1}(\cos \theta) \frac{\partial \psi_{lm}}{\partial x} \cos(m+1)\phi \\ & - \sum_{l=0}^{\infty} \sum_{m=0}^l P_{l-1}^{m+1}(\cos \theta) \frac{\partial \psi_{lm}}{\partial x} \cos(m+1)\phi \\ & + \sum_{l=0}^{\infty} \sum_{m=0}^l (l+m)(l+m-1) P_{l-1}^{m-1}(\cos \theta) \frac{\partial \psi_{lm}}{\partial x} \cos(m-1)\phi \\ & - \sum_{l=0}^{\infty} \sum_{m=0}^l (l-m+1)(l-m+2) P_{l+1}^{m-1}(\cos \theta) \frac{\partial \psi_{lm}}{\partial x} \cos(m-1)\phi \\ & + (2) \Sigma_t \sum_{l=0}^{\infty} \sum_{m=0}^l (2l+1) P_l^m(\cos \theta) \psi_{lm} \cos(m\phi) \\ & = (2) \int_{E'} \sum_{l=0}^{\infty} (2l+1) \Sigma_{s_l} P_l(\cos \theta) \sum_{l=0}^{\infty} \psi_{l0} dE' \\ & + (2) \int_{E'} \sum_{l=1}^{\infty} (2l+1) \Sigma_{s_l} P_l^m(\cos \theta) \sum_{l=1}^{\infty} \sum_{m=1}^l \psi_{lm} \cos(m\phi) dE' \\ & + (2) \chi_p (1-\beta) \int_{E'} \nu \Sigma_f \psi_{00} dE' P_0^0(\cos \theta) \\ & + (2) \sum_{l=0}^{\infty} \sum_{m=0}^l (2l+1) P_l^m(\cos \theta) S_{lm} \cos(m\phi) \\ & + (2) \sum_{k=1}^n \chi_k \lambda_k C_k P_0^0(\cos \theta) \end{aligned} \quad (17)$$

Next, the subscripts and superscripts may be set to put the transport equation back in terms of spherical harmonics. This can be done because starting an infinite series

expression at a different point will not change series convergence as long as all the series indices are likewise changed. Accomplishing this produced this form:

$$\begin{aligned}
& \frac{2}{v} \frac{\partial}{\partial t} \sum_{l=0}^{\infty} \sum_{m=0}^l (2l+1) P_l^m(\cos \theta) \psi_{lm} \cos(m\phi) \\
& + (2) \sum_{l=1}^{\infty} \sum_{m=0}^l (l-m) P_l^m(\cos \theta) \frac{\partial \psi_{l-1,m}}{\partial z} \cos(m\phi) \\
& + (2) \sum_{l=0}^{\infty} \sum_{m=0}^l (l+m+1) P_l^m(\cos \theta) \frac{\partial \psi_{l+1,m}}{\partial z} \cos(m\phi) \\
& + \sum_{l=1}^{\infty} \sum_{m=1}^l P_l^m(\cos \theta) \frac{\partial \psi_{l-1,m-1}}{\partial x} \cos(m\phi) \\
& - \sum_{l=-1}^{\infty} \sum_{m=1}^l P_l^m(\cos \theta) \frac{\partial \psi_{l+1,m-1}}{\partial x} \cos(m\phi) \\
& + \sum_{l=0}^{\infty} \sum_{m=0}^l (l+m+2)(l+m+1) P_l^m(\cos \theta) \frac{\partial \psi_{l+1,m+1}}{\partial x} \cos(m\phi) \\
& - \sum_{l=1}^{\infty} \sum_{m=-1}^l (l-m-1)(l-m) P_l^m(\cos \theta) \frac{\partial \psi_{l-1,m+1}}{\partial x} \cos(m\phi) \\
& + (2) \Sigma_t \sum_{l=0}^{\infty} \sum_{m=0}^l (2l+1) P_l^m(\cos \theta) \psi_{lm} \cos(m\phi) \\
& = (2) \int_{E'} \sum_{l=0}^{\infty} (2l+1) \Sigma_{s_l} P_l(\cos \theta) \sum_{l=0}^{\infty} \psi_{l0} dE' \\
& + (2) \int_{E'} \sum_{l=1}^{\infty} (2l+1) \Sigma_{s_l} P_l^m(\cos \theta) \sum_{l=1}^{\infty} \sum_{m=1}^l \psi_{lm} \cos(m\phi) dE' \\
& + (2) \chi_p (1-\beta) \int_{E'} \nu \Sigma_f \psi_{00} dE' P_0^0(\cos \theta) \\
& + (2) \sum_{l=0}^{\infty} \sum_{m=0}^l (2l+1) P_l^m(\cos \theta) S_{lm} \cos(m\phi) \\
& + (2) \sum_{k=1}^n \chi_k \lambda_k C_k P_0^0(\cos \theta) \tag{18}
\end{aligned}$$

Equation (18) is still in exact form. However, the summations to infinity prohibit practical implementation. The expansion coefficients  $\psi_{lm}$  are what we are ultimately solving for. They can be found by integrating over all directions and using orthogonality. If every term in Equation (18) is multiplied by  $P_K^N(\cos \theta) \cos(N\phi)$ , and the integration over all directions is done, there are two orthogonal relationships to ad-

dress. One has been defined by Equation (14). The other is related to the azimuthal angle,  $\phi$ . It is defined as:

$$\int_0^{2\pi} \cos(m\phi) \cos(N\phi) d\phi = \begin{cases} 0 & \text{if } m \neq N \\ \pi & \text{if } m = N \neq 0 \\ 2\pi & \text{if } m = N = 0 \end{cases} \quad (19)$$

Now we multiply Equation (18) by  $P_K^N(\cos \theta) \cos(N\phi)$ , and set it up to integrate over all directions. This yields:

$$\begin{aligned} & \int_{\pi}^0 \int_0^{2\pi} \frac{2}{v} \frac{\partial}{\partial t} \sum_{l=0}^{\infty} \sum_{m=0}^l (2l+1) P_l^m(\cos \theta) \psi_{lm} \cos(m\phi) P_K^N(\cos \theta) \cos(N\phi) d\phi d(\cos \theta) \\ & + (2) \int_{\pi}^0 \int_0^{2\pi} \sum_{l=1}^{\infty} \sum_{m=0}^l (l-m) P_l^m(\cos \theta) \frac{\partial \psi_{l-1,m}}{\partial z} \cos(m\phi) \\ & \quad \cdot P_K^N(\cos \theta) \cos(N\phi) d\phi d(\cos \theta) \\ & + (2) \int_{\pi}^0 \int_0^{2\pi} \sum_{l=0}^{\infty} \sum_{m=0}^l (l+m+1) P_l^m(\cos \theta) \frac{\partial \psi_{l+1,m}}{\partial z} \cos(m\phi) \\ & \quad \cdot P_K^N(\cos \theta) \cos(N\phi) d\phi d(\cos \theta) \\ & + \int_{\pi}^0 \int_0^{2\pi} \sum_{l=1}^{\infty} \sum_{m=1}^l P_l^m(\cos \theta) \frac{\partial \psi_{l-1,m-1}}{\partial x} \cos(m\phi) P_K^N(\cos \theta) \cos(N\phi) d\phi d(\cos \theta) \\ & - \int_{\pi}^0 \int_0^{2\pi} \sum_{l=-1}^{\infty} \sum_{m=1}^l P_l^m(\cos \theta) \frac{\partial \psi_{l+1,m-1}}{\partial x} \cos(m\phi) P_K^N(\cos \theta) \cos(N\phi) d\phi d(\cos \theta) \\ & + \int_{\pi}^0 \int_0^{2\pi} \sum_{l=0}^{\infty} \sum_{m=0}^l (l+m+2)(l+m+1) P_l^m(\cos \theta) \frac{\partial \psi_{l+1,m+1}}{\partial x} \cos(m\phi) \\ & \quad \cdot P_K^N(\cos \theta) \cos(N\phi) d\phi d(\cos \theta) \\ & - \int_{\pi}^0 \int_0^{2\pi} \sum_{l=1}^{\infty} \sum_{m=-1}^l (l-m-1)(l-m) P_l^m(\cos \theta) \frac{\partial \psi_{l-1,m+1}}{\partial x} \cos(m\phi) \\ & \quad \cdot P_K^N(\cos \theta) \cos(N\phi) d\phi d(\cos \theta) \\ & + (2) \int_{\pi}^0 \int_0^{2\pi} \sum_{l=0}^{\infty} \sum_{m=0}^l (2l+1) P_l^m(\cos \theta) \psi_{lm} \cos(m\phi) P_K^N(\cos \theta) \cos(N\phi) d\phi d(\cos \theta) \\ & = (2) \int_{\pi}^0 \int_0^{2\pi} \int_{E'} \sum_{l=0}^{\infty} (2l+1) \Sigma_{sl} P_l(\cos \theta) \sum_{l=0}^{\infty} \psi_{l0} dE' P_K^N(\cos \theta) \cos(N\phi) d\phi d(\cos \theta) \\ & + (2) \int_{\pi}^0 \int_0^{2\pi} \int_{E'} \sum_{l=1}^{\infty} (2l+1) \Sigma_{sl} P_l^m(\cos \theta) \sum_{l=1}^{\infty} \sum_{m=1}^l \psi_{lm} \cos(m\phi) dE' \end{aligned}$$

$$\begin{aligned}
& \cdot P_K^N(\cos \theta) \cos(N\phi) d\phi d(\cos \theta) \\
& + (2) \int_{\pi}^0 \int_0^{2\pi} \chi_p (1 - \beta) \int_{E'} \nu \Sigma_f \psi_{00} dE' P_0^0(\cos \theta) P_K^N(\cos \theta) \cos(N\phi) d\phi d(\cos \theta) \\
& + (2) \int_{\pi}^0 \int_0^{2\pi} \sum_{l=0}^{\infty} \sum_{m=0}^l (2l+1) P_l^m(\cos \theta) S_{lm} \cos(m\phi) P_K^N(\cos \theta) \cos(N\phi) d\phi d(\cos \theta) \\
& + (2) \int_{\pi}^0 \int_0^{2\pi} \sum_{k=1}^n \chi_k \lambda_k C_k P_0^0(\cos \theta) P_K^N(\cos \theta) \cos(N\phi) d\phi d(\cos \theta) \quad (20)
\end{aligned}$$

So far no approximations to the transport equation have been made. Simplifications, such as the isotropic nature of fission, were theoretically correct. However, we are now ready to incorporate some approximations to the transport equation to get it into a solvable form.

### 3.1 The $P_1$ Approximation

Equation (20) is exact. Now the first approximation to the transport equation is to be made. The summation over  $l$  is truncated to some finite value for the angular flux and inhomogeneous source expansions. Truncating the upper limit of  $l$  also sets the upper limit of  $m$ . If  $l = 0$ , then  $m = 0$  in all cases. If  $l = 1$ , then  $m$  can take on values of 0 and 1. For certain values of  $l$  and  $m$  some summation terms in Equation (20) will not exist. Making the  $P_1$  approximation states that either all expansion coefficients  $\psi_{2m} \approx 0$  or that the partials of  $\psi_{2m}$  in either the  $x$  or  $z$  directions are approximately zero. Therefore this approximation is not uniquely defined.

The  $P_1$  approximation states that the angular flux can be adequately defined by

$$\begin{aligned}
\Psi(r, E, \Omega, t) &= \frac{1}{4\pi} P_0^0(\cos \theta) \psi_{00}(r, E, t) + \frac{3}{4\pi} P_1^0(\cos \theta) \psi_{10}(r, E, t) \\
&+ \frac{3}{4\pi} P_1^1(\cos \theta) \psi_{11}(r, E, t) \cos \phi
\end{aligned}$$

Some values for the associated Legendre polynomials are [Ref. 27]:

$$\begin{aligned} P_0^0(\cos \theta) &= 1 & P_1^0(\cos \theta) &= \cos \theta \\ P_1^1(\cos \theta) &= \sin \theta \end{aligned} \quad (21)$$

For the angular flux expansion we then have,

$$\Psi(r, E, \Omega, t) = \frac{1}{4\pi} \psi_{00} + \frac{3}{4\pi} \cos \theta \psi_{10} + \frac{3}{4\pi} \sin \theta \psi_{11} \cos \phi \quad (22)$$

where the function arguments of the expansion coefficients have been dropped. The  $P_1$  approximation is the first correction to the diffusion equation.

Diffusion theory is valid in large homogeneous or nearly homogeneous reactors in which the curvature of the reactor is close to the mean free paths of the neutrons [Ref. 9]. Diffusion theory breaks down near reactor boundaries or strong absorbing materials [Ref. 10]. Therefore, since the  $P_1$  approximation resembles diffusion theory, it is expected that similar properties would hold for it. However, the diffusion coefficient should be better defined for the  $P_1$  transport equation approximation.

Now if we let  $K = N = 0$  in Equation (20) and integrate over all directions, we get,

$$\begin{aligned} \frac{1}{v} \frac{\partial}{\partial t} \psi_{00} + \frac{\partial \psi_{10}}{\partial z} + \frac{\partial \psi_{11}}{\partial x} + \Sigma_t \psi_{00} &= \int_{E'} \Sigma_{s0} \psi_{00} dE' + \chi_p (1 - \beta) \int_{E'} \nu \Sigma_f \psi_{00} dE' \\ &+ S_{00} + \sum_{k=1}^n \chi_k \lambda_k C_k \end{aligned} \quad (23)$$

Doing the same procedure but setting  $K = 1$  and  $N = 0$  results in,

$$\begin{aligned} \frac{3}{v} \frac{\partial}{\partial t} \psi_{10} + \frac{\partial \psi_{00}}{\partial z} + 2 \frac{\partial \psi_{20}}{\partial z} + 3 \frac{\partial \psi_{21}}{\partial x} + 3 \Sigma_t \psi_{10} \\ = 3 \int_{E'} \Sigma_{s1} \psi_{10} dE' + 3 S_{10} \end{aligned} \quad (24)$$

Applying the  $P_1$  approximation to Equation (24) yields:

$$\frac{3}{v} \frac{\partial}{\partial t} \psi_{10} + \frac{\partial \psi_{00}}{\partial z} + 3 \Sigma_t \psi_{10} = 3 \int_{E'} \Sigma_{s1} \psi_{10} dE' + 3 S_{10} \quad (25)$$

Again, setting  $K = N = 1$  in Equation (20), integrating, and implementing the  $P_1$  approximation results in,

$$\frac{3}{v} \frac{\partial}{\partial t} \psi_{11} + \frac{\partial \psi_{00}}{\partial x} + 3 \Sigma_t \psi_{11} = 3 \int_{E'} \Sigma_{s1} \psi_{11} dE' + 3 S_{11} \quad (26)$$

(In Equation (26), for  $m = 1$ , the  $\psi_{00}$  coefficient is multiplied by 2. This is caused by not using the recurrence relationship defined by Equation (5) since for the case when  $m = 0$ ,  $P_l^{-1}(\cos \theta)$  would result [Ref. 11].) Three equations have been developed with three unknowns,  $\psi_{00}$ ,  $\psi_{10}$  and  $\psi_{11}$ .

### 3.2 The Multigroup Approximation

This approximation entails dividing the infinite energy spectrum into discrete energy groups that are defined so that the spatial shape of the flux does not change in the discrete groups [Ref. 10]. If the energy groups are defined small enough, then this isn't much of an approximation at all. The multigroup approximations to Equations (23), (25), and (26) yield:

$$\begin{aligned} \frac{1}{v_g} \frac{\partial}{\partial t} \psi_{00}^g + \frac{\partial \psi_{10}^g}{\partial z} + \frac{\partial \psi_{11}^g}{\partial x} + \Sigma_t^g \psi_{00}^g &= \sum_{g'=1}^G \Sigma_{s0}^{g' \rightarrow g} \psi_{00}^{g'} \\ &+ \chi_p^g (1 - \beta) \sum_{g'=1}^G \nu^{g'} \Sigma_f^{g'} \psi_{00}^{g'} + S_{00}^g + \sum_{k=1}^n \chi_k^g \lambda_k C_k \end{aligned} \quad (27)$$

$$\frac{3}{v_g} \frac{\partial}{\partial t} \psi_{10}^g + \frac{\partial \psi_{00}^g}{\partial z} + 3 \Sigma_t^g \psi_{10}^g = 3 \sum_{g'=1}^G \Sigma_{s1}^{g' \rightarrow g} \psi_{10}^{g'} + 3 S_{10}^g \quad (28)$$

$$\frac{3}{v_g} \frac{\partial}{\partial t} \psi_{11}^g + \frac{\partial \psi_{00}^g}{\partial x} + 3 \Sigma_t^g \psi_{11}^g = 3 \sum_{g'=1}^G \Sigma_{s1}^{g' \rightarrow g} \psi_{11}^{g'} + 3 S_{11}^g \quad (29)$$

Each of the above equations is valid for a particular energy group  $g$ , with  $g = 1, 2, \dots, G$  as possible values.

### 3.3 Time Discretization: Euler's Backward Differencing

Equations (27), (28), and (29) will now be discretized in time using Euler's backward differencing scheme. This is an implicit scheme since it involves variables of the present time step on both sides of the equation. This scheme is numerically stable [Ref.3], which is its most desirable characteristic. The present time step is designated with a  $(N+1)$  superscript, and the previous time step is designated with a  $(N)$  superscript. Implementing,

$$\begin{aligned} \frac{1}{v_g} \frac{\psi_{00}^{(N+1)} - \psi_{00}^{(N)}}{\Delta t} + \frac{\partial \psi_{10}^{(N+1)}}{\partial z} + \frac{\partial \psi_{11}^{(N+1)}}{\partial x} + \Sigma_t^g \psi_{00}^{(N+1)} = \sum_{g'=1}^G \Sigma_{s_0}^{g' \rightarrow g} \psi_{00}^{(N+1)} \\ + \chi_p^g (1 - \beta) \sum_{g'=1}^G \nu_{g'} \Sigma_f^{g'} \psi_{00}^{(N+1)} + S_{00}^{(N+1)} + \sum_{k=1}^n \chi_k^g \lambda_k C_k^{(N+1)} \end{aligned} \quad (30)$$

$$\begin{aligned} \frac{3}{v_g} \frac{\psi_{10}^{(N+1)} - \psi_{10}^{(N)}}{\Delta t} + \frac{\partial \psi_{00}^{(N+1)}}{\partial z} + 3 \Sigma_t^g \psi_{10}^{(N+1)} \\ = 3 \sum_{g'=1}^G \Sigma_{s_1}^{g' \rightarrow g} \psi_{10}^{(N+1)} + 3 S_{10}^{(N+1)} \end{aligned} \quad (31)$$

$$\begin{aligned} \frac{3}{v_g} \frac{\psi_{11}^{(N+1)} - \psi_{11}^{(N)}}{\Delta t} + \frac{\partial \psi_{00}^{(N+1)}}{\partial x} + 3 \Sigma_t^g \psi_{11}^{(N+1)} \\ = 3 \sum_{g'=1}^G \Sigma_{s_1}^{g' \rightarrow g} \psi_{11}^{(N+1)} + 3 S_{11}^{(N+1)} \end{aligned} \quad (32)$$

Now all values with a superscript  $(N)$  are known because they are values from a previous time step. The  $\psi$  values that have the superscript  $(N+1)$  are our unknowns. The inhomogeneous sources are always known no matter their superscript because we assume that the extraneous neutron source contributions can be directly calculated.

The precursor values  $C_k^{(N+1)}$  in Equation (30) now are addressed. The precursor concentration for the present time step may be calculated in terms of the previous time step precursor concentration. The rate of change of the precursor concentration

with respect to time is [Ref. 7],

$$\frac{\partial C_k(r, t)}{\partial t} = \beta_k \sum_{g'=1}^G \nu^{g'} \Sigma_f^{g'} \psi_{00}^{g'} - \lambda_k C_k(r, t) \quad k = 1, 3, \dots, n \quad (33)$$

Discretization of Equation (33) in time using Euler's backward differencing yields,

$$\frac{C_k^{(N+1)} - C_k^{(N)}}{\Delta t} = \beta_k \sum_{g'=1}^G \nu^{g'} \Sigma_f^{g'} \psi_{00}^{g'(N+1)} - \lambda_k C_k^{(N+1)} \quad (34)$$

Solving Equation (34) for  $C_k^{(N+1)}$  yields,

$$C_k^{(N+1)} = \left( \frac{1}{1 + \lambda_k \Delta t} \right) C_k^{(N)} + \left( \frac{\Delta t}{1 + \lambda_k \Delta t} \right) \beta_k \sum_{g'=1}^G \nu^{g'} \Sigma_f^{g'} \psi_{00}^{g'(N+1)} \quad (35)$$

Now the present time step value of the precursor concentration can always be calculated in a straightforward manner using its previous time step value. Substituting Equation (35) into Equation (30) and rearranging yields,

$$\begin{aligned} & \frac{1}{v_g \Delta t} \psi_{00}^{g(N+1)} + \frac{\partial \psi_{10}^{g(N+1)}}{\partial z} + \frac{\partial \psi_{11}^{g(N+1)}}{\partial x} + \Sigma_t^g \psi_{00}^{g(N+1)} \\ &= \frac{1}{v_g \Delta t} \psi_{00}^{g(N)} + \sum_{g'=1}^G \Sigma_{s_0}^{g' \rightarrow g} \psi_{00}^{g'(N+1)} + S_{00}^{g(N+1)} \\ &+ \left[ \chi_p^g (1 - \beta) + \sum_{k=1}^n \chi_k^g \beta_k \left( \frac{1}{1 + \frac{1}{\lambda_k \Delta t}} \right) \right] \sum_{g'=1}^G \nu^{g'} \Sigma_f^{g'} \psi_{00}^{g'(N+1)} \\ &+ \sum_{k=1}^n \frac{\chi_k^g \lambda_k C_k^{(N)}}{1 + \lambda_k \Delta t} \end{aligned} \quad (36)$$

A Taylor series expansion can show that the error for this backward difference approximation is  $\mathcal{O}(\Delta t)$  [Ref. 37]. Thus a large  $\Delta t$  with a quickly changing process could yield a large error. However, computational cost stipulate the selection of the largest  $\Delta t$  possible that yields a convergent solution.

If there are  $G$  energy groups, then  $G$  equations may be written using Equation (36). Likewise, the same may be done using Equations (31) and (32) respectively. Thus, Equations (36), (31), and (32) may be written in vector form repre-



senting  $G$  energy groups. The vector form for Equation (36) is,

$$\begin{aligned} \frac{\partial}{\partial z} \Psi_{10}^{(N+1)} + \frac{\partial}{\partial x} \Psi_{11}^{(N+1)} + \Sigma^{00} \Psi_{00}^{(N+1)} \\ = S_{00}^{(N+1)} + V \Psi_{00}^{(N)} + \Sigma^f \Psi_{00}^{(N+1)} + C^{(N)} \end{aligned} \quad (37)$$

here  $\Psi_{10}^{(N+1)}$ ,  $\Psi_{11}^{(N+1)}$ ,  $\Psi_{00}^{(N+1)}$ ,  $S_{00}^{(N+1)}$ ,  $\Psi_{00}^{(N)}$ , and  $C^{(N)}$  are vectors containing  $G$  entries.  $\Sigma^{00}$ ,  $V$ , and  $\Sigma^f$  are  $G \times G$  matrices. All these terms, and other vectors and matrices developed later, are defined in Appendix A. Equation (31) in vector form is,

$$\frac{\partial}{\partial z} \Psi_{00}^{(N+1)} + 3 \Sigma^{10} \Psi_{10}^{(N+1)} = 3 V \Psi_{10}^{(N)} + 3 S_{10}^{(N+1)} \quad (38)$$

Equation (32) in vector form is,

$$\frac{\partial}{\partial x} \Psi_{00}^{(N+1)} + 3 \Sigma^{11} \Psi_{11}^{(N+1)} = 3 V \Psi_{11}^{(N)} + 3 S_{11}^{(N+1)} \quad (39)$$

Now solve Equation (38) for  $\Psi_{10}^{(N+1)}$ :

$$\begin{aligned} 3 \Sigma^{10} \Psi_{10}^{(N+1)} &= 3 V \Psi_{10}^{(N)} + 3 S_{10}^{(N+1)} - \frac{\partial}{\partial z} \Psi_{00}^{(N+1)} \\ \text{Define } D^{10} &= \{\Sigma^{10}\}^{-1}, \text{ then,} \\ \Psi_{10}^{(N+1)} &= \frac{1}{3} D^{10} \left[ 3 V \Psi_{10}^{(N)} + 3 S_{10}^{(N+1)} - \frac{\partial}{\partial z} \Psi_{00}^{(N+1)} \right] \end{aligned} \quad (40)$$

For Equation (39), solve for  $\Psi_{11}^{(N+1)}$ :

$$\begin{aligned} 3 \Sigma^{11} \Psi_{11}^{(N+1)} &= 3 V \Psi_{11}^{(N)} + 3 S_{11}^{(N+1)} - \frac{\partial}{\partial x} \Psi_{00}^{(N+1)} \\ \text{Define } D^{11} &= \{\Sigma^{11}\}^{-1}, \\ \Psi_{11}^{(N+1)} &= \frac{1}{3} D^{11} \left[ 3 V \Psi_{11}^{(N)} + 3 S_{11}^{(N+1)} - \frac{\partial}{\partial x} \Psi_{00}^{(N+1)} \right] \end{aligned} \quad (41)$$

Define  $\bar{D}^{10} = \frac{1}{3} D^{10}$  and  $\bar{D}^{11} = \frac{1}{3} D^{11}$ . Then substituting Equations (40) and (41) into (37) will yield,

$$\begin{aligned}
& -\frac{\partial}{\partial z} \bar{D}^{10} \frac{\partial}{\partial z} \Psi_{00}^{(N+1)} - \frac{\partial}{\partial x} \bar{D}^{11} \frac{\partial}{\partial x} \Psi_{00}^{(N+1)} + \Sigma^{00} \Psi_{00}^{(N+1)} \\
& = \Sigma^f \Psi_{00}^{(N+1)} + S_{00}^{(N+1)} + V \Psi_{00}^{(N)} + C^{(N)} \\
& -\frac{\partial}{\partial z} D^{10} V \Psi_{10}^{(N)} - \frac{\partial}{\partial z} D^{10} S_{10}^{(N+1)} \\
& -\frac{\partial}{\partial x} D^{11} V \Psi_{11}^{(N)} - \frac{\partial}{\partial x} D^{11} S_{11}^{(N+1)} \tag{42}
\end{aligned}$$

This is the equation in which the spatial discretization using the finite element method will be made. The only unknowns are in the  $\Psi_{00}^{(N+1)}$  vectors.

### 3.4 Finite Element Implementation

If Equation (42) is put into a matrix equation form of say  $A\mathbf{x} = \mathbf{b}$ , then numerical algorithms can be used to obtain a solution [Ref. 18]. Thus far, the transport equation has been discretized in its angular dependency using spherical harmonics, discretized in its energy dependency using the multigroup approximation, and discretized in time using Euler's backward differencing. Now we turn to the spatial discretization.

The finite element procedure consists of approximating a solution with a trial function. The set of functions that approximate the solution vector is referred to as a trial space. Once the proper trial function is selected, then we invoke the method of weighted residuals incorporated with the Galerkin method. This will tend to spread the error that resulted from the trial function approximation so that it is, in some sense, small over the whole problem domain. For transport equation problems such as this, error analysis comparisons between the finite element process and finite differencing schemes favor using finite elements [Ref. 19] [Ref. 24]. We now summarize the method.

Consider the following equation,

$$\nabla^2 \phi - f = 0 \quad (43)$$

where  $f$  is a known function of the independent variables. We approximate the solution  $\phi$  with some trial function,  $\tilde{\phi}$ . Most likely then Equation (43) will not be true. There should be some error called the residual,  $R$ , such that,

$$\nabla^2 \tilde{\phi} - f = R. \quad (44)$$

where

$$\tilde{\phi} = \sum_{i=1}^M \phi_i N_i \quad (45)$$

The  $\phi_i$ s in Equation (45) are the expansion coefficients, and the  $N_i$ s are interpolating functions [Ref. 13]. If the residual is weighted over the entire domain to determine the  $\phi_i$ s such that the error is small, then this is implementing the method of weighted residuals [Ref. 13] [Ref. 14]. We now choose  $M$  linearly independent weighting functions,  $W_i$ , so that

$$\int_D [\nabla^2 \tilde{\phi} - f] W_i dD = \int_D R W_i dD = 0, \quad (46)$$

where  $D$  in Equation (46) denotes the problem domain. So, in some sense, the residual  $R \approx 0$  over the entire problem domain. The Galerkin method simply states that the weighting functions,  $W_i$ , may be the same as the approximating or trial functions [Ref. 13].

Several methods exist for developing the finite element equations. Using the Galerkin method allows the development of these equations without any knowledge of the physical processes or variational calculus. Imposing it allows the development of a numerical algorithm to solve

$$\int_D [\nabla^2 \tilde{\phi} - f] W_i dD = 0. \quad (47)$$

The Galerkin method is now used to solve Equation (42) for XZ slab geometry.

### 3.5 Finite Element Discretization for XZ Geometry

Linear B splines will be used for the interpolating functions. These functions are continuous in their first derivatives. The angular flux vectors may be expanded in the form,

$$\Psi_{lm}^{(N+1)} \approx \tilde{\Psi}_{lm}^{(N+1)} = \sum_{p=1}^A \sum_{q=1}^B \Psi_{lm_{pq}}^{(N+1)} B_p(x) B_q(z) \quad (48)$$

And the inhomogeneous and precursor sources may likewise be expanded,

$$S_{lm}^{(N+1)} \approx \tilde{S}_{lm}^{(N+1)} = \sum_{p=1}^A \sum_{q=1}^B S_{lm_{pq}}^{(N+1)} B_p(x) B_q(z) \quad (49)$$

$$C^{(N)} \approx \tilde{C}^{(N)} = \sum_{p=1}^A \sum_{q=1}^B C_{pq}^{(N)} B_p(x) B_q(z) \quad (50)$$

$A$  and  $B$  in the above summations represent the upper limits of the mesh spacing in the  $x$  and  $z$  directions respectively. Likewise, the  $p$  and  $q$  subscripts represent the  $p^{th}$  mesh point in the  $x$  direction and the  $q^{th}$  mesh point in the  $z$  direction.  $B_p(x)$  and  $B_q(z)$  are linear basic splines or linear  $B$  splines, sometimes referred to as linear hat functions [Ref. 21]. They are defined as

$$B_p(x) = \begin{cases} 0 & \text{for } x < x_{p-1} \\ \frac{x - x_{p-1}}{x_p - x_{p-1}} & \text{if } x_{p-1} \leq x \leq x_p \\ \frac{x_{p+1} - x}{x_{p+1} - x_p} & \text{if } x_p \leq x \leq x_{p+1} \\ 0 & \text{for } x > x_{p+1} \end{cases} \quad (51)$$

And:

$$B_q(z) = \begin{cases} 0 & \text{for } z < z_{q-1} \\ \frac{z - z_{q-1}}{z_q - z_{q-1}} & \text{if } z_{q-1} \leq z \leq z_q \\ \frac{z_{q+1} - z}{z_{q+1} - z_q} & \text{if } z_q \leq z \leq z_{q+1} \\ 0 & \text{for } z > z_{q+1} \end{cases} \quad (52)$$

It is easier to see how these hat functions relate to each other when considering only one dimension. Figure 1 shows that each interior linear  $B$  spline only overlaps itself and its two nearest neighbors. This overlapping is an important characteristic which

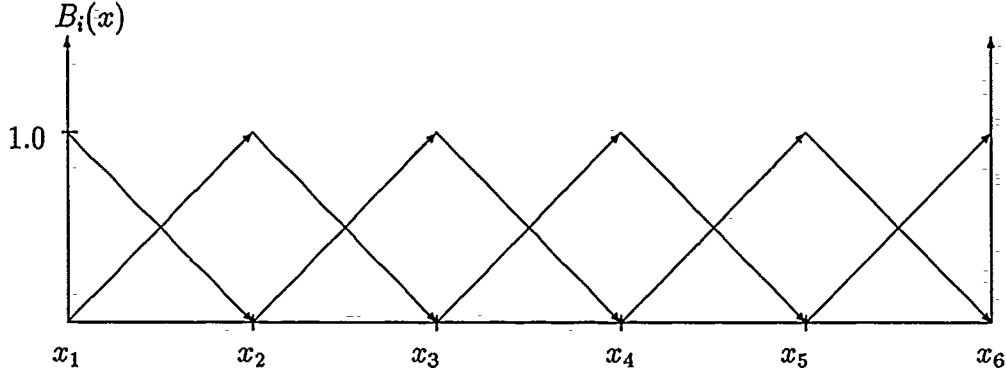


Figure 1: Linear  $B$  Splines

will be shown later. Two steps now need to be done. First, define the weighting functions shown in Equations (46) and (47) as  $B_i(x)$  for the  $x$  direction, and  $B_j(z)$  for the  $z$  direction. Second, substitute the approximating (trial) functions in the form shown in Equations (48), (49), and (50) into Equation (42), and invoke the Galerkin procedure. This yields,

$$\begin{aligned}
& - \int_0^L \int_0^K \frac{\partial}{\partial z} \overline{D}^{10} \frac{\partial}{\partial z} \tilde{\Psi}_{00}^{(N+1)} B_i(x) B_j(z) dz dx \\
& - \int_0^L \int_0^K \frac{\partial}{\partial x} \overline{D}^{11} \frac{\partial}{\partial x} \tilde{\Psi}_{00}^{(N+1)} B_i(x) B_j(z) dz dx \\
& + \int_0^L \int_0^K \Sigma^{00} \tilde{\Psi}_{00}^{(N+1)} B_i(x) B_j(z) dz dx \\
& = \int_0^L \int_0^K \Sigma^J \tilde{\Psi}_{00}^{(N+1)} B_i(x) B_j(z) dz dx \\
& + \int_0^L \int_0^K \tilde{S}_{00}^{(N+1)} B_i(x) B_j(z) dz dx
\end{aligned}$$

$$\begin{aligned}
& + \int_0^L \int_0^K V \tilde{\Psi}_{00}^{(N)} B_i(x) B_j(z) dz dx \\
& + \int_0^L \int_0^K \tilde{C}^{(N)} B_i(x) B_j(z) dz dx \\
& - \int_0^L \int_0^K \frac{\partial}{\partial z} D^{10} V \tilde{\Psi}_{10}^{(N)} B_i(x) B_j(z) dz dx \\
& - \int_0^L \int_0^K \frac{\partial}{\partial z} D^{10} \tilde{S}_{10}^{(N+1)} B_i(x) B_j(z) dz dx \\
& - \int_0^L \int_0^K \frac{\partial}{\partial x} D^{11} V \tilde{\Psi}_{11}^{(N)} B_i(x) B_j(z) dz dx \\
& - \int_0^L \int_0^K \frac{\partial}{\partial x} D^{11} \tilde{S}_{11}^{(N+1)} B_i(x) B_j(z) dz dx
\end{aligned} \tag{53}$$

The streaming terms (partial derivative terms) in Equation (53) will be integrated by parts. This will accomplish two important results. First, since the  $B$  splines are only continuous in their first derivative, terms having two partials operating on them would produce a value of zero. However, integrating by parts lowers the derivative order applied to the  $B$  splines by one. Thus, this legitimizes their use. Second, but probably the most important result, is that the integration procedure introduces, with relative ease, the natural boundary conditions into the finite elements [Ref. 13].

Integration by parts in one dimension is defined in the usual manner,

$$\int_a^b u dv = u v \Big|_a^b - \int_a^b v du.$$

However, in two dimensions, integration by parts is done using Green's theorem:

$$\iint_D u (\nabla \cdot \vec{v}) dD = \int_S u (\vec{v} \cdot \vec{n}) dS - \iint_D \vec{v} \cdot \nabla u dD. \tag{54}$$

In three dimensions, integration by parts is defined as Gauss's theorem [Ref. 13].

So an area integral is put in terms of a surface integral using Green's theorem. To

use Equation (54), let,

$$\begin{aligned}\nabla &= \frac{\partial}{\partial x} \mathbf{i} + \frac{\partial}{\partial z} \mathbf{k} \\ \vec{n} &= n_x \mathbf{i} + n_z \mathbf{k} \\ \vec{V} &= \frac{\partial \tilde{\Psi}_{00}^{(N+1)}}{\partial x} \mathbf{i} + \frac{\partial \tilde{\Psi}_{00}^{(N+1)}}{\partial z} \mathbf{k} \\ u &= B_i(x) B_j(z)\end{aligned}$$

$\vec{n}$  is a unit vector normal to the slab's surface, always pointing in an outward direction.  $n_x$  and  $n_z$  are the direction cosines of the unit vector  $\vec{n}$ . Figure 2 shows the geometry definitions.

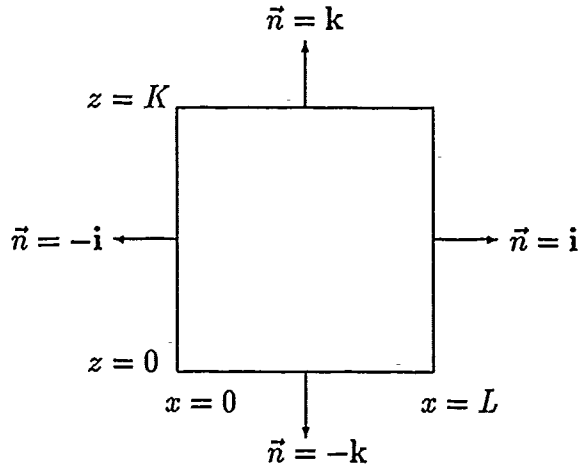


Figure 2: Two Dimensional Slab Geometry

If the entire slab's surface is defined as  $\Sigma$ , then performing the surface integration in Equation (54) over the entire surface is the same as integrating over each individual surface part. Thus,

$$\int_{\Sigma} d\Sigma = \int_{S_1} dS_1 + \int_{S_2} dS_2 + \int_{S_3} dS_3 + \int_{S_4} dS_4.$$

The dot product of  $\vec{V}$  and  $\vec{n}$  then isolates the particular surface face in question.

Integrating by parts appears to complicate the equation because it introduces more terms. However, later substitutions will be made to reduce the number of boundary terms. Now integrating by parts and rearranging puts the transport equation in the form:

$$\begin{aligned}
& \int_0^L \int_0^K \bar{D}^{10} \frac{\partial \tilde{\Psi}_{00}^{(N+1)}}{\partial z} B_i(x) \frac{\partial B_j(z)}{\partial z} dz dx + \int_0^L \int_0^K \bar{D}^{11} \frac{\partial \tilde{\Psi}_{00}^{(N+1)}}{\partial x} \frac{\partial B_i(x)}{\partial x} B_j(z) dz dx \\
& + \int_0^L \int_0^K \Sigma^{00} \tilde{\Psi}_{00}^{(N+1)} B_i(x) B_j(z) dz dx = \int_0^L \int_0^K \Sigma^J \tilde{\Psi}_{00}^{(N+1)} B_i(x) B_j(z) dz dx \\
& + \int_0^L \int_0^K \tilde{S}_{00}^{(N+1)} B_i(x) B_j(z) dz dx + \int_0^L \int_0^K V \tilde{\Psi}_{00}^{(N)} B_i(x) B_j(z) dz dx \\
& + \int_0^L \int_0^K \tilde{C}^{(N)} B_i(x) B_j(z) dz dx + \int_0^L \int_0^K D^{10} V \tilde{\Psi}_{10}^{(N)} B_i(x) \frac{\partial B_j(z)}{\partial z} dz dx \\
& + \int_0^L \int_0^K D^{10} \tilde{S}_{10}^{(N+1)} B_i(x) \frac{\partial B_j(z)}{\partial z} dz dx + \int_0^L \int_0^K D^{11} V \tilde{\Psi}_{11}^{(N)} \frac{\partial B_i(x)}{\partial x} B_j(z) dz dx \\
& + \int_0^L \int_0^K D^{11} \tilde{S}_{11}^{(N+1)} \frac{\partial B_i(x)}{\partial x} B_j(z) dz dx + \int_0^L \bar{D}^{10} B_i(x) \left[ B_j(z) \frac{\partial \tilde{\Psi}_{00}^{(N+1)}}{\partial z} \right]_0^K dx \\
& + \int_0^K \bar{D}^{11} B_j(z) \left[ B_i(x) \frac{\partial \tilde{\Psi}_{00}^{(N+1)}}{\partial x} \right]_0^L dz - \int_0^L D^{10} V B_i(x) \left[ B_j(z) \tilde{\Psi}_{10}^{(N)} \right]_0^K dx \\
& - \int_0^L D^{10} B_i(x) \left[ B_j(z) \tilde{S}_{10}^{(N+1)} \right]_0^K dx - \int_0^K D^{11} V B_j(z) \left[ B_i(x) \tilde{\Psi}_{11}^{(N)} \right]_0^L dz \\
& - \int_0^K D^{11} B_j(z) \left[ B_i(x) \tilde{S}_{11}^{(N+1)} \right]_0^L dz
\end{aligned} \tag{55}$$

Equation (55) has seventeen terms, including six boundary terms. The number of boundary terms may be reduced to two if substitutions derived from Equations (40) and (41) are made. Recalling that  $\bar{D}^{10} = \frac{1}{3} D^{10}$  and  $\bar{D}^{11} = \frac{1}{3} D^{11}$  and making the



substitutions yields,

$$\begin{aligned}
& \int_0^L \int_0^K \bar{D}^{10} \frac{\partial \tilde{\Psi}_{00}^{(N+1)}}{\partial z} B_i(x) \frac{\partial B_j(z)}{\partial z} dz dx + \int_0^L \int_0^K \bar{D}^{11} \frac{\partial \tilde{\Psi}_{00}^{(N+1)}}{\partial x} \frac{\partial B_i(x)}{\partial x} B_j(z) dz dx \\
& + \int_0^L \int_0^K \Sigma^{00} \tilde{\Psi}_{00}^{(N+1)} B_i(x) B_j(z) dz dx = \int_0^L \int_0^K \Sigma^j \tilde{\Psi}_{00}^{(N+1)} B_i(x) B_j(z) dz dx \\
& + \int_0^L \int_0^K \tilde{S}_{00}^{(N+1)} B_i(x) B_j(z) dz dx + \int_0^L \int_0^K V \tilde{\Psi}_{00}^{(N)} B_i(x) B_j(z) dz dx \\
& + \int_0^L \int_0^K \tilde{C}^{(N)} B_i(x) B_j(z) dz dx + \int_0^L \int_0^K D^{10} V \tilde{\Psi}_{10}^{(N)} B_i(x) \frac{\partial B_j(z)}{\partial z} dz dx \\
& + \int_0^L \int_0^K D^{10} \tilde{S}_{10}^{(N+1)} B_i(x) \frac{\partial B_j(z)}{\partial z} dz dx + \int_0^L \int_0^K D^{11} V \tilde{\Psi}_{11}^{(N)} \frac{\partial B_i(x)}{\partial x} B_j(z) dz dx \\
& + \int_0^L \int_0^K D^{11} \tilde{S}_{11}^{(N+1)} \frac{\partial B_i(x)}{\partial x} B_j(z) dz dx - \int_0^K B_j(z) \left[ B_i(x) \tilde{\Psi}_{11}^{(N+1)} \right]_0^L dz \\
& - \int_0^L B_i(x) \left[ B_j(z) \tilde{\Psi}_{10}^{(N+1)} \right]_0^K dx
\end{aligned} \tag{56}$$

Reducing the number of boundary terms introduces present time step currents,  $\tilde{\Psi}_{10}^{(N+1)}$  and  $\tilde{\Psi}_{11}^{(N+1)}$  which are unknown. However, we can use Marshak boundary conditions and get these currents in terms of  $\tilde{\Psi}_{00}^{(N+1)}$  [Ref. 9], [Ref. 11], [Ref. 15] and [Ref. 16]. For XZ geometry, the Marshak condition for a vacuum is: [Ref. 11]

$$\int_{\mathbf{n} \cdot \Omega \leq 0} \mathbf{n} \cdot \Omega P_l^m(\cos \theta) \cos(m\phi) \Psi(\mathbf{r}, E, \Omega, t) d\Omega = 0 \tag{57}$$

where the angular flux,  $\Psi(\mathbf{r}, E, \Omega, t)$  is defined in Equation (22) and  $\mathbf{n}$  is a unit normal vector at the surface pointing outwards. (Equation (57) is for even  $l$ .)

Marshak boundary conditions set the integral of the incoming current to zero. Although neutrons that leave a surface possess a finite probability of returning in reality, the ones that return usually have a negligible effect on criticality. It has been determined that for low order  $P_n$  approximations, Marshak boundary conditions

yield better results than say Mark boundary conditions. In fact, Henry states that numerical studies show that Marshak conditions lead to consistently more accurate results up to a  $P_{19}$  approximation [Ref. 1].

At  $x = 0$  and  $x = L$ ,  $B_1(x) = B_A(x) = 1.0$ . And at  $z = 0$  and  $z = K$ ,  $B_1(z) = B_B(z) = 1.0$ . The subscripts  $A$  and  $B$  on the linear  $B$  splines indicate the upper limits of the trial function expansions. If we consider a Marshak vacuum condition with Equation (57), then the transport equation becomes,

$$\begin{aligned}
& \int_0^L \int_0^K \bar{D}^{10} \frac{\partial \tilde{\Psi}_{00}^{(N+1)}}{\partial z} B_i(x) \frac{\partial B_j(z)}{\partial z} dz dx + \int_0^L \int_0^K \bar{D}^{11} \frac{\partial \tilde{\Psi}_{00}^{(N+1)}}{\partial x} \frac{\partial B_i(x)}{\partial x} B_j(z) dz dx \\
& + \int_0^L \int_0^K \Sigma^{00} \tilde{\Psi}_{00}^{(N+1)} B_i(x) B_j(z) dz dx = \int_0^L \int_0^K \Sigma^f \tilde{\Psi}_{00}^{(N+1)} B_i(x) B_j(z) dz dx \\
& + \int_0^L \int_0^K \tilde{S}_{00}^{(N+1)} B_i(x) B_j(z) dz dx + \int_0^L \int_0^K V \tilde{\Psi}_{00}^{(N)} B_i(x) B_j(z) dz dx \\
& + \int_0^L \int_0^K \tilde{C}^{(N)} B_i(x) B_j(z) dz dx + \int_0^L \int_0^K D^{10} V \tilde{\Psi}_{10}^{(N)} B_i(x) \frac{\partial B_j(z)}{\partial z} dz dx \\
& + \int_0^L \int_0^K D^{10} \tilde{S}_{10}^{(N+1)} B_i(x) \frac{\partial B_j(z)}{\partial z} dz dx + \int_0^L \int_0^K D^{11} V \tilde{\Psi}_{11}^{(N)} \frac{\partial B_i(x)}{\partial x} B_j(z) dz dx \\
& + \int_0^L \int_0^K D^{11} \tilde{S}_{11}^{(N+1)} \frac{\partial B_i(x)}{\partial x} B_j(z) dz dx - \frac{1}{2} \int_0^K \sum_{q=1}^B \Psi_{00_{1q}}^{(N+1)} B_q(z) B_j(z) dz \\
& - \frac{1}{2} \int_0^K \sum_{q=1}^B \Psi_{00_{Aq}}^{(N+1)} B_q(z) B_j(z) dz - \frac{1}{2} \int_0^L \sum_{p=1}^A \Psi_{00_{p1}}^{(N+1)} B_p(x) B_i(x) dx \\
& - \frac{1}{2} \int_0^L \sum_{p=1}^A \Psi_{00_{pB}}^{(N+1)} B_p(x) B_i(x) dx
\end{aligned} \tag{58}$$

Recall that the expansion of the flux in the  $x$  direction went from  $p = 1$  to  $p = A$ . In the  $z$  direction, the expansion went from  $q = 1$  to  $q = B$ . Therefore, in Equation (58), the boundary flux terms are defined as, (see Figure 2 on page 25)

$$\begin{aligned}
\Psi_{00_{1q}}^{(N+1)} & \text{ is on the surface where } & x = 0 & \quad z = 0 \text{ to } K \\
\Psi_{00_{Aq}}^{(N+1)} & \text{ is on the surface where } & x = L & \quad z = 0 \text{ to } K \\
\Psi_{00_{p1}}^{(N+1)} & \text{ is on the surface where } & z = 0 & \quad x = 0 \text{ to } L \\
\Psi_{00_{pB}}^{(N+1)} & \text{ is on the surface where } & z = K & \quad x = 0 \text{ to } L
\end{aligned}$$

Now the whole transport equation will be expanded:

$$\begin{aligned}
& \int_0^L \int_0^K \bar{D}^{10} \sum_{p=1}^A \sum_{q=1}^B \Psi_{00_{pq}}^{(N+1)} B_p(x) \frac{\partial B_q(z)}{\partial z} B_i(x) \frac{\partial B_j(z)}{\partial z} dz dx \\
& + \int_0^L \int_0^K \bar{D}^{11} \sum_{p=1}^A \sum_{q=1}^B \Psi_{00_{pq}}^{(N+1)} \frac{\partial B_p(x)}{\partial x} B_q(z) \frac{\partial B_i(x)}{\partial x} B_j(z) dz dx \\
& + \int_0^L \int_0^K \Sigma^{00} \sum_{p=1}^A \sum_{q=1}^B \Psi_{00_{pq}}^{(N+1)} B_p(x) B_q(z) B_i(x) B_j(z) dz dx \\
& = \int_0^L \int_0^K \Sigma^J \sum_{p=1}^A \sum_{q=1}^B \Psi_{00_{pq}}^{(N+1)} B_p(x) B_q(z) B_i(x) B_j(z) dz dx \\
& + \int_0^L \int_0^K \sum_{p=1}^A \sum_{q=1}^B S_{00_{pq}}^{(N+1)} B_p(x) B_q(z) B_i(x) B_j(z) dz dx \\
& + \int_0^L \int_0^K V \sum_{p=1}^A \sum_{q=1}^B \Psi_{00_{pq}}^{(N)} B_p(x) B_q(z) B_i(x) B_j(z) dz dx \\
& + \int_0^L \int_0^K \sum_{p=1}^A \sum_{q=1}^B C^{(N)} B_p(x) B_q(z) B_i(x) B_j(z) dz dx \\
& + \int_0^L \int_0^K D^{10} V \sum_{p=1}^A \sum_{q=1}^B \Psi_{10_{pq}}^{(N)} B_p(x) B_q(z) B_i(x) \frac{\partial B_j(z)}{\partial z} dz dx \\
& + \int_0^L \int_0^K D^{10} \sum_{p=1}^A \sum_{q=1}^B S_{10_{pq}}^{(N+1)} B_p(x) B_q(z) B_i(x) \frac{\partial B_j(z)}{\partial z} dz dx \\
& + \int_0^L \int_0^K D^{11} V \sum_{p=1}^A \sum_{q=1}^B \Psi_{11_{pq}}^{(N)} B_p(x) B_q(z) \frac{\partial B_i(x)}{\partial x} B_j(z) dz dx
\end{aligned}$$

$$\begin{aligned}
& + \int_0^L \int_0^K \bar{D}^{11} \sum_{p=1}^A \sum_{q=1}^B S_{11pq}^{(N+1)} B_p(x) B_q(z) \frac{\partial B_i(x)}{\partial x} B_j(z) dz dx \\
& - \frac{1}{2} \int_0^K \sum_{q=1}^B \Psi_{001q}^{(N+1)} B_q(z) B_j(z) dz \\
& - \frac{1}{2} \int_0^K \sum_{q=1}^B \Psi_{00Aq}^{(N+1)} B_q(z) B_j(z) dz \\
& - \frac{1}{2} \int_0^L \sum_{p=1}^A \Psi_{00p1}^{(N+1)} B_p(x) B_i(x) dx \\
& - \frac{1}{2} \int_0^L \sum_{p=1}^A \Psi_{00pB}^{(N+1)} B_p(x) B_i(x) dx
\end{aligned} \tag{59}$$

As previously stated and shown in Figure 1, each linear  $B$  spline overlaps itself and its two nearest neighbors. This implies that  $p = i - 1, i, i + 1$  and  $q = j - 1, j, j + 1$ . Also, the integration may now be over each element, since the boundary fluxes are set, and each element carries the boundary terms with them [Ref. 13].  $e_x$  will denote integration of the elements in the  $x$  direction and  $e_z$  will likewise denote integration of the elements in the  $z$  direction. Therefore,

$$\begin{aligned}
& \int_{e_x} \int_{e_z} \bar{D}^{10} \sum_{p=i-1}^{i+1} \sum_{q=j-1}^{j+1} \Psi_{00pq}^{(N+1)} B_p(x) \frac{\partial B_q(z)}{\partial z} B_i(x) \frac{\partial B_j(z)}{\partial z} dz dx \\
& + \int_{e_x} \int_{e_z} \bar{D}^{11} \sum_{p=i-1}^{i+1} \sum_{q=j-1}^{j+1} \Psi_{00pq}^{(N+1)} \frac{\partial B_p(x)}{\partial x} B_q(z) \frac{\partial B_i(x)}{\partial x} B_j(z) dz dx \\
& + \int_{e_x} \int_{e_z} \Sigma^{00} \sum_{p=i-1}^{i+1} \sum_{q=j-1}^{j+1} \Psi_{00pq}^{(N+1)} B_p(x) B_q(z) B_i(x) B_j(z) dz dx \\
& = \int_{e_x} \int_{e_z} \Sigma^J \sum_{p=i-1}^{i+1} \sum_{q=j-1}^{j+1} \Psi_{00pq}^{(N+1)} B_p(x) B_q(z) B_i(x) B_j(z) dz dx \\
& + \int_{e_x} \int_{e_z} \sum_{p=i-1}^{i+1} \sum_{q=j-1}^{j+1} S_{00pq}^{(N+1)} B_p(x) B_q(z) B_i(x) B_j(z) dz dx
\end{aligned}$$

$$\begin{aligned}
& + \int_{c_x} \int_{c_z} V \sum_{p=i-1}^{i+1} \sum_{q=j-1}^{j+1} \Psi_{00pq}^{(N)} B_p(x) B_q(z) B_i(x) B_j(z) dz dx \\
& + \int_{c_x} \int_{c_z} \sum_{p=i-1}^{i+1} \sum_{q=j-1}^{j+1} C^{(N)} B_p(x) B_q(z) B_i(x) B_j(z) dz dx \\
& + \int_{c_x} \int_{c_z} D^{10} V \sum_{p=i-1}^{i+1} \sum_{q=j-1}^{j+1} \Psi_{10pq}^{(N)} B_p(x) B_q(z) B_i(x) \frac{\partial B_j(z)}{\partial z} dz dx \\
& + \int_{c_x} \int_{c_z} D^{10} \sum_{p=i-1}^{i+1} \sum_{q=j-1}^{j+1} S_{10pq}^{(N+1)} B_p(x) B_q(z) B_i(x) \frac{\partial B_j(z)}{\partial z} dz dx \\
& + \int_{c_x} \int_{c_z} D^{11} V \sum_{p=i-1}^{i+1} \sum_{q=j-1}^{j+1} \Psi_{11pq}^{(N)} B_p(x) B_q(z) \frac{\partial B_i(x)}{\partial x} B_j(z) dz dx \\
& + \int_{c_x} \int_{c_z} D^{11} \sum_{p=i-1}^{i+1} \sum_{q=j-1}^{j+1} S_{11pq}^{(N+1)} B_p(x) B_q(z) \frac{\partial B_i(x)}{\partial x} B_j(z) dz dx \\
& - \frac{1}{2} \int_{c_x} \sum_{q=j-1}^{j+1} \Psi_{001q}^{(N+1)} B_q(z) B_j(z) dz - \frac{1}{2} \int_{c_x} \sum_{q=j-1}^{j+1} \Psi_{00Aq}^{(N+1)} B_q(z) B_j(z) dz \\
& - \frac{1}{2} \int_{c_x} \sum_{p=i-1}^{i+1} \Psi_{00p1}^{(N+1)} B_p(x) B_i(x) dx - \frac{1}{2} \int_{c_x} \sum_{p=i-1}^{i+1} \Psi_{00pB}^{(N+1)} B_p(x) B_i(x) dx
\end{aligned} \tag{60}$$

The integration summaries for the elements are given in Appendix B. Each material matrix is assumed to be piece-wise continuous in each  $xz$  interval. Bringing the boundary terms over to the right side of the equation and integrating Equation (60) with Kronecker delta notation yields,

$$\begin{aligned}
& \left\{ \left( \frac{h_{j-1}}{12} \right) \Psi_{001j-1}^{(N+1)} + \left( \frac{h_{j-1} + h_j}{6} \right) \Psi_{001j}^{(N+1)} + \left( \frac{h_j}{12} \right) \Psi_{001j+1}^{(N+1)} \right\} \delta_{1q} \\
& + \left\{ \left( \frac{h_{j-1}}{12} \right) \Psi_{00Aj-1}^{(N+1)} + \left( \frac{h_{j-1} + h_j}{6} \right) \Psi_{00Aj}^{(N+1)} + \left( \frac{h_j}{12} \right) \Psi_{00Aj+1}^{(N+1)} \right\} \delta_{Aq} \\
& + \left\{ \left( \frac{h_{i-1}}{12} \right) \Psi_{00i-11}^{(N+1)} + \left( \frac{h_{i-1} + h_i}{6} \right) \Psi_{00i1}^{(N+1)} + \left( \frac{h_i}{12} \right) \Psi_{00i+11}^{(N+1)} \right\} \delta_{p1} \\
& + \left\{ \left( \frac{h_{i-1}}{12} \right) \Psi_{00i-1B}^{(N+1)} + \left( \frac{h_{i-1} + h_i}{6} \right) \Psi_{00iB}^{(N+1)} + \left( \frac{h_i}{12} \right) \Psi_{00i+1B}^{(N+1)} \right\} \delta_{pB}
\end{aligned}$$

**THIS  
PAGE  
IS  
MISSING  
IN  
ORIGINAL  
DOCUMENT**

$$\begin{aligned}
& + \left( \frac{1}{h_{i-1}} \right) \left( \frac{h_j}{6} \right) \bar{D}_{i-1j}^{11} + \left( \frac{1}{h_i} \right) \left( \frac{h_j}{6} \right) \bar{D}_{ij}^{11} \\
& + \left( \frac{h_{i-1}}{3} \right) \left( \frac{h_j}{6} \right) [\Sigma_{i-1j}^{00} - \Sigma_{i-1j}^f] + \left( \frac{h_i}{3} \right) \left( \frac{h_j}{6} \right) [\Sigma_{ij}^{00} - \Sigma_{ij}^f] \left\} \Psi_{00i,j+1}^{(N+1)} \\
& + \left\{ \left( \frac{h_i}{6} \right) \left( \frac{-1}{h_{j-1}} \right) \bar{D}_{ij-1}^{10} + \left( \frac{-1}{h_i} \right) \left( \frac{h_{j-1}}{6} \right) \bar{D}_{ij-1}^{11} \right. \\
& + \left. \left( \frac{h_i}{6} \right) \left( \frac{h_{j-1}}{6} \right) [\Sigma_{ij-1}^{00} - \Sigma_{ij-1}^f] \right\} \Psi_{00i+1,j-1}^{(N+1)} \\
& + \left\{ \left( \frac{h_i}{6} \right) \left( \frac{1}{h_{j-1}} \right) \bar{D}_{ij-1}^{10} + \left( \frac{h_i}{6} \right) \left( \frac{1}{h_j} \right) \bar{D}_{ij}^{10} \right. \\
& + \left. \left( \frac{-1}{h_i} \right) \left( \frac{h_{j-1}}{3} \right) \bar{D}_{ij-1}^{11} + \left( \frac{-1}{h_i} \right) \left( \frac{h_j}{3} \right) \bar{D}_{ij}^{11} \right. \\
& + \left. \left( \frac{h_i}{6} \right) \left( \frac{h_{j-1}}{3} \right) [\Sigma_{ij-1}^{00} - \Sigma_{ij-1}^f] + \left( \frac{h_i}{6} \right) \left( \frac{h_j}{6} \right) [\Sigma_{ij}^{00} - \Sigma_{ij}^f] \right\} \Psi_{00i+1,j}^{(N+1)} \\
& + \left\{ \left( \frac{h_i}{6} \right) \left( \frac{-1}{h_j} \right) \bar{D}_{ij}^{10} + \left( \frac{-1}{h_i} \right) \left( \frac{h_j}{6} \right) \bar{D}_{ij}^{11} \right. \\
& + \left. \left( \frac{h_i}{6} \right) \left( \frac{h_j}{6} \right) [\Sigma_{ij}^{00} - \Sigma_{ij}^f] \right\} \Psi_{00i+1,j+1}^{(N+1)} \\
& = \left( \frac{h_{i-1}}{6} \right) \left( \frac{h_{j-1}}{6} \right) [S_{00i-1,j-1}^{(N+1)} + V \Psi_{00i-1,j-1}^{(N)} + C_{i-1,j-1}^{(N)}] \\
& + \left\{ \left( \frac{h_{i-1}}{6} \right) \left( \frac{h_{j-1}}{3} \right) + \left( \frac{h_{i-1}}{6} \right) \left( \frac{h_j}{3} \right) \right\} [S_{00i-1,j}^{(N+1)} + V \Psi_{00i-1,j}^{(N)} + C_{i-1,j}^{(N)}] \\
& + \left( \frac{h_{i-1}}{6} \right) \left( \frac{h_j}{3} \right) [S_{00i-1,j+1}^{(N+1)} + V \Psi_{00i-1,j+1}^{(N)} + C_{i-1,j+1}^{(N)}] \\
& + \left\{ \left( \frac{h_{i-1}}{3} \right) \left( \frac{h_{j-1}}{6} \right) + \left( \frac{h_i}{3} \right) \left( \frac{h_{j-1}}{6} \right) \right\} [S_{00i,j-1}^{(N+1)} + V \Psi_{00i,j-1}^{(N)} + C_{i,j-1}^{(N)}] \\
& + \left\{ \left( \frac{h_{i-1}}{3} \right) \left( \frac{h_{j-1}}{3} \right) + \left( \frac{h_{i-1}}{3} \right) \left( \frac{h_j}{3} \right) + \left( \frac{h_i}{3} \right) \left( \frac{h_{j-1}}{3} \right) \right. \\
& + \left. \left( \frac{h_i}{3} \right) \left( \frac{h_j}{3} \right) \right\} [S_{00i,j}^{(N+1)} + V \Psi_{00i,j}^{(N)} + C_{i,j}^{(N)}] \\
& + \left\{ \left( \frac{h_{i-1}}{3} \right) \left( \frac{h_j}{6} \right) + \left( \frac{h_i}{3} \right) \left( \frac{h_j}{6} \right) \right\} [S_{00i,j+1}^{(N+1)} + V \Psi_{00i,j+1}^{(N)} + C_{i,j+1}^{(N)}] \\
& + \left( \frac{h_i}{6} \right) \left( \frac{h_{j-1}}{6} \right) [S_{00i+1,j-1}^{(N+1)} + V \Psi_{00i+1,j-1}^{(N)} + C_{i+1,j-1}^{(N)}] \\
& + \left\{ \left( \frac{h_i}{6} \right) \left( \frac{h_{j-1}}{3} \right) + \left( \frac{h_i}{6} \right) \left( \frac{h_j}{3} \right) \right\} [S_{00i+1,j}^{(N+1)} + V \Psi_{00i+1,j}^{(N)} + C_{i+1,j}^{(N)}] \\
& + \left( \frac{h_i}{6} \right) \left( \frac{h_j}{3} \right) [S_{00i+1,j+1}^{(N+1)} + V \Psi_{00i+1,j+1}^{(N)} + C_{i+1,j+1}^{(N)}]
\end{aligned}$$

$$\begin{aligned}
& + \left( \frac{h_{i-1}}{6} \right) \left( \frac{1}{2} \right) D_{i-1j-1}^{10} [V \Psi_{10i-1j-1}^{(N)} + S_{10i-1j-1}^{(N+1)}] \\
& + \left\{ \left( \frac{h_{i-1}}{6} \right) \left( \frac{1}{2} \right) D_{i-1j-1}^{10} + \left( \frac{h_{i-1}}{6} \right) \left( \frac{-1}{2} \right) D_{i-1j}^{10} \right\} \\
& \quad \cdot [V \Psi_{10i-1j}^{(N)} + S_{10i-1j}^{(N+1)}] \\
& + \left( \frac{h_{i-1}}{6} \right) \left( \frac{-1}{2} \right) D_{i-1j}^{10} [V \Psi_{10i-1j+1}^{(N)} + S_{10i-1j+1}^{(N+1)}] \\
& + \left\{ \left( \frac{h_{i-1}}{3} \right) \left( \frac{1}{2} \right) D_{i-1j-1}^{10} + \left( \frac{h_i}{3} \right) \left( \frac{1}{2} \right) D_{ij-1}^{10} \right\} \\
& \quad \cdot [V \Psi_{10ij-1}^{(N)} + S_{10ij-1}^{(N+1)}] \\
& + \left\{ \left( \frac{h_{i-1}}{3} \right) \left( \frac{1}{2} \right) D_{i-1j-1}^{10} + \left( \frac{h_i}{3} \right) \left( \frac{1}{2} \right) D_{ij-1}^{10} \right. \\
& \quad \left. + \left( \frac{h_{i-1}}{3} \right) \left( \frac{-1}{2} \right) D_{i-1j}^{10} + \left( \frac{h_i}{3} \right) \left( \frac{-1}{2} \right) D_{ij}^{10} \right\} [V \Psi_{10ij}^{(N)} + S_{10ij}^{(N+1)}] \\
& + \left\{ \left( \frac{h_{i-1}}{3} \right) \left( \frac{-1}{2} \right) D_{i-1j}^{10} + \left( \frac{h_i}{3} \right) \left( \frac{-1}{2} \right) D_{ij}^{10} \right\} \\
& \quad \cdot [V \Psi_{10ij+1}^{(N)} + S_{10ij+1}^{(N+1)}] \\
& + \left( \frac{h_i}{6} \right) \left( \frac{1}{2} \right) D_{ij-1}^{10} [V \Psi_{10i+1j-1}^{(N)} + S_{10i+1j-1}^{(N+1)}] \\
& + \left\{ \left( \frac{h_i}{6} \right) \left( \frac{1}{2} \right) D_{ij-1}^{10} + \left( \frac{h_i}{6} \right) \left( \frac{-1}{2} \right) D_{ij}^{10} \right\} \\
& \quad \cdot [V \Psi_{10i+1j}^{(N)} + S_{10i+1j}^{(N+1)}] \\
& + \left( \frac{h_i}{6} \right) \left( \frac{-1}{2} \right) D_{ij}^{10} [V \Psi_{10i+1j+1}^{(N)} + S_{10i+1j+1}^{(N+1)}] \\
& + \left( \frac{1}{2} \right) \left( \frac{h_{j-1}}{6} \right) D_{i-1j-1}^{11} [V \Psi_{11i-1j-1}^{(N)} + S_{11i-1j-1}^{(N+1)}] \\
& + \left\{ \left( \frac{1}{2} \right) \left( \frac{h_{j-1}}{3} \right) D_{i-1j-1}^{11} + \left( \frac{1}{2} \right) \left( \frac{h_j}{3} \right) D_{i-1j}^{11} \right\} \\
& \quad \cdot [V \Psi_{11i-1j}^{(N)} + S_{11i-1j}^{(N+1)}] \\
& + \left( \frac{1}{2} \right) \left( \frac{h_j}{6} \right) D_{i-1j}^{11} [V \Psi_{11i-1j+1}^{(N)} + S_{11i-1j+1}^{(N+1)}] \\
& + \left\{ \left( \frac{1}{2} \right) \left( \frac{h_{j-1}}{6} \right) D_{i-1j-1}^{11} + \left( \frac{-1}{2} \right) \left( \frac{h_{j-1}}{6} \right) D_{ij-1}^{11} \right\} \\
& \quad \cdot [V \Psi_{11ij-1}^{(N)} + S_{11ij-1}^{(N+1)}] \\
& + \left\{ \left( \frac{1}{2} \right) \left( \frac{h_{j-1}}{3} \right) D_{i-1j-1}^{11} + \left( \frac{-1}{2} \right) \left( \frac{h_{j-1}}{3} \right) D_{ij-1}^{10} \right.
\end{aligned}$$



$$\begin{aligned}
& + \left( \frac{1}{2} \right) \left( \frac{h_j}{3} \right) D_{i-1,j}^{11} + \left( \frac{-1}{2} \right) \left( \frac{h_j}{3} \right) D_{i,j}^{11} \left\{ V \Psi_{11,j}^{(N)} + S_{11,j}^{(N+1)} \right\} \\
& + \left\{ \left( \frac{1}{2} \right) \left( \frac{h_j}{6} \right) D_{i-1,j}^{11} + \left( \frac{-1}{2} \right) \left( \frac{h_j}{6} \right) D_{i,j}^{11} \right\} \\
& \quad \cdot \left[ V \Psi_{11,i,j+1}^{(N)} + S_{11,i,j+1}^{(N+1)} \right] \\
& + \left( \frac{-1}{2} \right) \left( \frac{h_{j-1}}{6} \right) D_{i,j-1}^{11} \left[ V \Psi_{11,i+1,j-1}^{(N)} + S_{11,i+1,j-1}^{(N+1)} \right] \\
& + \left\{ \left( \frac{-1}{2} \right) \left( \frac{h_{j-1}}{3} \right) D_{i,j-1}^{11} + \left( \frac{-1}{2} \right) \left( \frac{h_j}{3} \right) D_{i,j}^{11} \right\} \\
& \quad \cdot \left[ V \Psi_{11,i+1,j}^{(N)} + S_{11,i+1,j}^{(N+1)} \right] \\
& + \left( \frac{-1}{2} \right) \left( \frac{h_j}{6} \right) D_{i,j}^{11} \left[ V \Psi_{11,i+1,j+1}^{(N)} + S_{11,i+1,j+1}^{(N+1)} \right]
\end{aligned} \tag{61}$$

### 3.6 Coefficient Matrix Example

When Equation (61) is implemented a square symmetric positive definite block matrix equation is produced. The matrix equation is in the form of  $A \Psi_{00}^{(N+1)} = S$ .  $A$  is the coefficient matrix,  $\Psi_{00}^{(N+1)}$  are the expansion coefficients that physically represent the total flux at mesh points  $ij$ , and  $S$  is the source vector. If we are considering a system that has  $G$  energy groups, then each entry in  $A$ ,  $\tilde{A}_{ij}$ , is a  $G \times G$  matrix. Likewise, each of the entries in  $\Psi_{00}^{(N+1)}$  and  $S$  are  $G \times 1$  vectors. Thus we have a block matrix equation. Block multiplication can be carried out in the same way as traditional matrix multiplication since all entries will have the proper dimensions [Ref. 20].

Suppose we have a slab with 16 mesh points, 4 in the  $x$  direction and 4 in the  $z$  direction as shown in Figure 3. By applying Equation (61) for the sixteen mesh points, we will get a 16 by 16 matrix,  $A$ , and 16 by 1 vectors,  $\Psi_{00}^{(N+1)}$  and  $S$ . This system is shown in Figure 4. The block matrix has a bandwidth of 11 with nine nonzero diagonals. For this example, there are 100 nonzero  $\tilde{A}_{ij}$  entries. Each entry is a material defined matrix for an  $xz$  interval along with factors resulting from

the finite element integrations. For a particular spatial interval, the material cross sections are assumed to be piece-wise constant.

This development of the coefficient matrix was done in a "brute force" way. Traditional finite element schemes assemble the coefficient matrix in a much simpler way by using a local to global mesh point numbering scheme. This entails the addition of local coefficient matrices to yield the global coefficient matrix. The source vector is likewise developed. Thus one advantage of finite element schemes was not taken advantage of here. But, it is clearer to see how each entry in the coefficient matrix was derived by developing the coefficient matrix in this manner.

Now we summarize this process for RZ geometry. Basically, everything is done the same as for XZ geometry, but the RZ case is slightly more complicated because of its streaming terms.

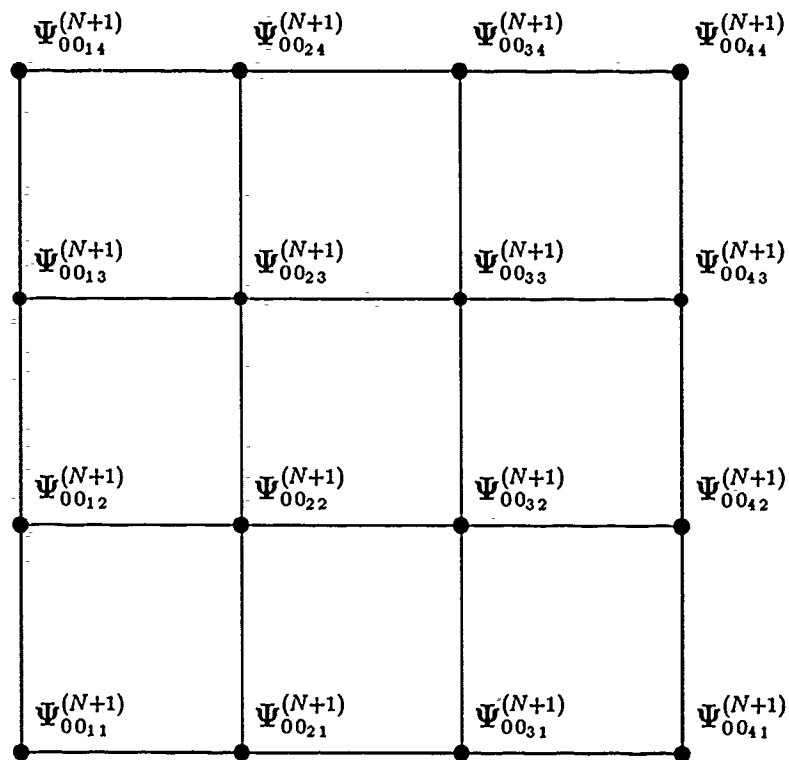


Figure 3: Two Dimensional Slab Mesh Point Layout Example

$$\begin{bmatrix}
A_{11} & A_{12} & 0 & 0 & A_{15} & A_{16} & 0 & 0 & 0 & 0 & 0 & 0 & 0 & 0 & 0 & 0 \\
A_{21} & A_{22} & A_{23} & 0 & A_{25} & A_{26} & A_{27} & 0 & 0 & 0 & 0 & 0 & 0 & 0 & 0 & 0 \\
0 & A_{32} & A_{33} & A_{34} & 0 & A_{36} & A_{37} & A_{38} & 0 & 0 & 0 & 0 & 0 & 0 & 0 & 0 \\
0 & 0 & A_{43} & A_{44} & 0 & 0 & A_{47} & A_{48} & 0 & 0 & 0 & 0 & 0 & 0 & 0 & 0 \\
A_{51} & A_{52} & 0 & 0 & A_{55} & A_{56} & 0 & 0 & A_{59} & A_{510} & 0 & 0 & 0 & 0 & 0 & 0 \\
A_{61} & A_{62} & A_{63} & 0 & A_{65} & A_{66} & A_{67} & 0 & A_{69} & A_{610} & A_{611} & 0 & 0 & 0 & 0 & 0 \\
0 & A_{72} & A_{73} & A_{74} & 0 & A_{76} & A_{77} & A_{78} & 0 & A_{710} & A_{711} & A_{712} & 0 & 0 & 0 & 0 \\
0 & 0 & A_{83} & A_{84} & 0 & 0 & A_{87} & A_{88} & 0 & 0 & A_{811} & A_{812} & 0 & 0 & 0 & 0 \\
0 & 0 & 0 & 0 & A_{95} & A_{96} & 0 & 0 & A_{99} & A_{910} & 0 & 0 & A_{913} & A_{914} & 0 & 0 \\
0 & 0 & 0 & 0 & A_{105} & A_{106} & A_{107} & 0 & A_{109} & A_{1010} & A_{1011} & 0 & A_{1013} & A_{1014} & A_{1015} & 0 \\
0 & 0 & 0 & 0 & 0 & A_{116} & A_{117} & A_{118} & 0 & A_{1110} & A_{1111} & A_{1112} & 0 & A_{1114} & A_{1115} & A_{1116} \\
0 & 0 & 0 & 0 & 0 & 0 & A_{127} & A_{128} & 0 & 0 & A_{1211} & A_{1212} & 0 & 0 & A_{1215} & A_{1216} \\
0 & 0 & 0 & 0 & 0 & 0 & 0 & 0 & A_{139} & A_{1310} & 0 & 0 & A_{1313} & A_{1314} & 0 & 0 \\
0 & 0 & 0 & 0 & 0 & 0 & 0 & 0 & A_{149} & A_{1410} & A_{1411} & 0 & A_{1413} & A_{1414} & A_{1415} & 0 \\
0 & 0 & 0 & 0 & 0 & 0 & 0 & 0 & 0 & A_{1510} & A_{1511} & A_{1512} & 0 & A_{1514} & A_{1515} & A_{1516} \\
0 & 0 & 0 & 0 & 0 & 0 & 0 & 0 & 0 & 0 & A_{1611} & A_{1612} & 0 & 0 & A_{1615} & A_{1616}
\end{bmatrix}
=
\begin{bmatrix}
\Psi_{0011}^{(N+1)} \\
\Psi_{0021}^{(N+1)} \\
\Psi_{0031}^{(N+1)} \\
\Psi_{0041}^{(N+1)} \\
\Psi_{0012}^{(N+1)} \\
\Psi_{0022}^{(N+1)} \\
\Psi_{0032}^{(N+1)} \\
\Psi_{0042}^{(N+1)} \\
\Psi_{0013}^{(N+1)} \\
\Psi_{0023}^{(N+1)} \\
\Psi_{0033}^{(N+1)} \\
\Psi_{0043}^{(N+1)} \\
\Psi_{0014}^{(N+1)} \\
\Psi_{0024}^{(N+1)} \\
\Psi_{0034}^{(N+1)} \\
\Psi_{0044}^{(N+1)}
\end{bmatrix}
=
\begin{bmatrix}
S_1 \\
S_2 \\
S_3 \\
S_4 \\
S_5 \\
S_6 \\
S_7 \\
S_8 \\
S_9 \\
S_{10} \\
S_{11} \\
S_{12} \\
S_{13} \\
S_{14} \\
S_{15} \\
S_{16}
\end{bmatrix}$$

Figure 4: Spatial Matrix Example

## 4 Solution in RZ Geometry

We now do much the same procedure to obtain an approximate solution to the transport equation in RZ geometry. The cylindrical coordinate system depends on azimuthal angle,  $\chi$ , a distance,  $r$ , measured from the  $z$  axis, and the coordinate  $z$  measured on the  $z$  axis itself from the  $xy$  plane. Figure 5 shows the geometry definitions. If we have azimuthal symmetry, then the neutron density is not changing with respect to the azimuthal angular coordinate  $\chi$ . Therefore the rate of change of the neutrons along a streaming path is accurately described by Equation (8). The flux and source may be expanded as before in Equations (2) and (3). Thus implementing

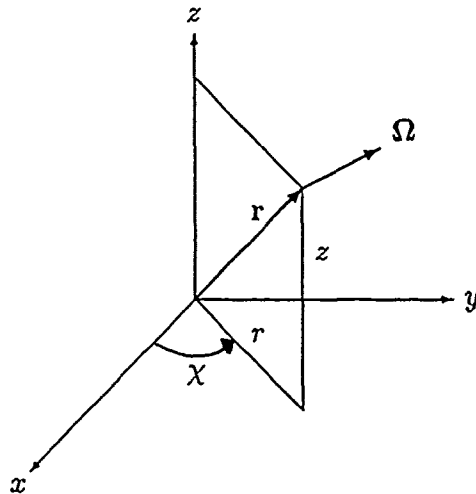


Figure 5: Cylindrical Geometry

Equations (2), (3), and (8) into Equation (1) puts the transport equation in a form much like Equation (12):

$$\begin{aligned}
& \frac{1}{v} \frac{\partial}{\partial t} \sum_{l=0}^{\infty} \sum_{m=0}^l \frac{2l+1}{4\pi} P_l^m(\cos \theta) \psi_{lm} \cos(m\phi) \\
& + \cos \theta \frac{\partial}{\partial z} \sum_{l=0}^{\infty} \sum_{m=0}^l \frac{2l+1}{4\pi} P_l^m(\cos \theta) \psi_{lm} \cos(m\phi) \\
& + \sin \theta \cos \phi \frac{\partial}{\partial r} \sum_{l=0}^{\infty} \sum_{m=0}^l \frac{2l+1}{4\pi} P_l^m(\cos \theta) \psi_{lm} \cos(m\phi) \\
& - \frac{\sin \theta \sin \phi}{r} \frac{\partial}{\partial \phi} \sum_{l=0}^{\infty} \sum_{m=0}^l \frac{2l+1}{4\pi} P_l^m(\cos \theta) \psi_{lm} \cos(m\phi) \\
& + \Sigma_t \sum_{l=0}^{\infty} \sum_{m=0}^l \frac{2l+1}{4\pi} P_l^m(\cos \theta) \psi_{lm} \cos(m\phi) \\
& = \int_{E'} \int_{\Omega'} \Sigma_s \sum_{l=0}^{\infty} \sum_{m=0}^l \frac{2l+1}{4\pi} P_l^m(\cos \theta') \psi_{lm} \cos(m\phi') d\Omega' dE' \\
& + \frac{\chi_p}{4\pi} (1 - \beta) \int_{E'} \int_{\Omega'} \nu \Sigma_f \sum_{l=0}^{\infty} \sum_{m=0}^l \frac{2l+1}{4\pi} P_l^m(\cos \theta') \psi_{lm} \cos(m\phi') d\Omega' dE' \\
& + \sum_{l=0}^{\infty} \sum_{m=0}^l \frac{2l+1}{4\pi} P_l^m(\cos \theta) S_{lm} \cos(m\phi) \\
& + \frac{1}{4\pi} \sum_{k=1}^n \chi_k \lambda_k C_k
\end{aligned} \tag{62}$$

The angular dependency of the angular neutron flux is described the same as for XZ geometry. Spherical harmonics have been used again for the angular discretization of the direction vector  $\Omega$  because they completely describe the angular dependency of  $\Omega$ . Note, because of the relationship,  $P_l^{-m}(\cos \theta) = (-1)^m \frac{(l-m)!}{(l+m)!} P_l^m(\cos \theta)$ , it is unnecessary to include negative  $m$  [Ref. 22] [Ref. 23]. To proceed, we need two more equations in addition to Equation (16). They are,

$$\frac{\partial}{\partial \phi} \cos(m\phi) = -m \sin(m\phi) \tag{63}$$

$$\sin(m\phi) \sin \phi = \frac{1}{2} \cos(m-1)\phi - \frac{1}{2} \cos(m+1)\phi \tag{64}$$

As before we assume fission to be an isotropic event, invoke the addition theorem, and rearrange. The transport equation now takes the form:

$$\begin{aligned}
& \frac{2}{v} \frac{\partial}{\partial t} \sum_{l=0}^{\infty} \sum_{m=0}^l (2l+1) P_l^m(\cos \theta) \psi_{lm} \cos(m\phi) \\
& + 2 \sum_{l=0}^{\infty} \sum_{m=0}^l (2l+1) \cos \theta P_l^m(\cos \theta) \frac{\partial \psi_{lm}}{\partial z} \cos(m\phi) \\
& + \sum_{l=0}^{\infty} \sum_{m=0}^l (2l+1) \sin \theta P_l^m(\cos \theta) \frac{\partial \psi_{lm}}{\partial r} \cos(m+1)\phi \\
& + \sum_{l=0}^{\infty} \sum_{m=0}^l (2l+1) \sin \theta P_l^m(\cos \theta) \frac{\partial \psi_{lm}}{\partial r} \cos(m-1)\phi \\
& + \frac{1}{r} \sum_{l=0}^{\infty} \sum_{m=0}^l (2l+1) \sin \theta P_l^m(\cos \theta) \psi_{lm}(m) \cos(m-1)\phi \\
& - \frac{1}{r} \sum_{l=0}^{\infty} \sum_{m=0}^l (2l+1) \sin \theta P_l^m(\cos \theta) \psi_{lm}(m) \cos(m+1)\phi \\
& + 2 \Sigma_t \sum_{l=0}^{\infty} \sum_{m=0}^l (2l+1) P_l^m(\cos \theta) \psi_{lm} \cos(m\phi) \\
& = (2) \int_{E'} \sum_{l=0}^{\infty} (2l+1) \Sigma_{s_l} P_l(\cos \theta) \sum_{l=0}^{\infty} \psi_{l0} dE' \\
& + (2) \int_{E'} \sum_{l=1}^{\infty} (2l+1) \Sigma_{s_l} P_l^m(\cos \theta) \sum_{l=1}^{\infty} \sum_{m=1}^l \psi_{lm} \cos(m\phi) dE' \\
& + 2 \chi_p (1-\beta) \int_{E'} \nu \Sigma_f \psi_{00} dE' P_0^0(\cos \theta) \\
& + 2 \sum_{l=0}^{\infty} \sum_{m=0}^l (2l+1) P_l^m(\cos \theta) S_{lm} \cos(m\phi) \\
& + 2 \sum_{k=1}^n \chi_k \lambda_k C_k P_0^0(\cos \theta)
\end{aligned} \tag{65}$$

As with XZ geometry, Equation (65) will be manipulated by implementing the recurrence relationships, adjusting the indices to put it back in terms of spherical harmonics, and then multiplying by  $P_K^N(\cos \theta) \cos(N\phi)$  and integrating in all directions. With stipulated values for  $K$  and  $N$  and using Euler's backward differencing scheme for time discretizations, the following vector equations are produced:

$$\begin{aligned} & \frac{\partial}{\partial z} \Psi_{10}^{(N+1)} + \frac{\partial}{\partial r} \Psi_{11}^{(N+1)} + \frac{1}{r} \Psi_{11}^{(N+1)} + \Sigma^{00} \Psi_{00}^{(N+1)} \\ &= S_{00}^{(N+1)} + V \Psi_{00}^{(N)} + \Sigma^f \Psi_{00}^{(N+1)} + C^{(N)} \end{aligned} \quad (66)$$

$$\frac{\partial}{\partial z} \Psi_{00}^{(N+1)} + 3 \Sigma^{10} \Psi_{10}^{(N+1)} = 3 V \Psi_{10}^{(N)} + 3 S_{10}^{(N+1)} \quad (67)$$

$$\frac{\partial}{\partial r} \Psi_{00}^{(N+1)} + 3 \Sigma^{11} \Psi_{11}^{(N+1)} = 3 V \Psi_{11}^{(N)} + 3 S_{11}^{(N+1)} \quad (68)$$

Now we substitute the value of  $\Psi_{10}^{(N+1)}$  from Equation (67) and the value of  $\Psi_{11}^{(N+1)}$  from Equation (68) into Equation (66) to yield,

$$\begin{aligned} & -\frac{\partial}{\partial z} \bar{D}^{10} \frac{\partial}{\partial z} \Psi_{00}^{(N+1)} - \frac{\partial}{\partial r} \bar{D}^{11} \frac{\partial}{\partial r} \Psi_{00}^{(N+1)} - \frac{1}{r} \bar{D}^{11} \frac{\partial}{\partial r} \Psi_{00}^{(N+1)} \\ & + \Sigma^{00} \Psi_{00}^{(N+1)} = \Sigma^f \Psi_{00}^{(N+1)} + S_{00}^{(N+1)} + V \Psi_{00}^{(N)} + C^{(N)} \\ & - \frac{\partial}{\partial z} D^{10} V \Psi_{10}^{(N)} - \frac{\partial}{\partial z} D^{10} S_{10}^{(N+1)} \\ & - \frac{\partial}{\partial r} D^{11} V \Psi_{11}^{(N)} - \frac{\partial}{\partial r} D^{11} S_{11}^{(N+1)} \\ & - \frac{1}{r} D^{11} V \Psi_{11}^{(N)} - \frac{1}{r} D^{11} S_{11}^{(N+1)} \end{aligned} \quad (69)$$

Equation (69) is the RZ equivalent to Equation (42) for XZ geometry, but Equation (69) has more terms, and some terms have a  $\frac{1}{r}$  factor in them. As the finite element spatial discretization is applied to Equation (69), some of the extra terms cancel with terms produced when integrating by parts. We now proceed with the finite element discretization.

#### 4.1 RZ Finite Element Discretization

The neutron sources in Equation (69) may be expanded with the same basis hat functions in the  $r$  and  $z$  directions as was done in the XZ geometry in Equations (48), (49), and (50). The hat functions in the  $z$  direction are defined as in Equation (52).



The functions in the  $r$  direction are defined as:

$$B_p(r) = \begin{cases} 0 & \text{for } r < r_{p-1} \\ \frac{r - r_{p-1}}{r_p - r_{p-1}} & \text{if } r_{p-1} \leq r \leq r_p \\ \frac{r_{p+1} - r}{r_{p+1} - r_p} & \text{if } r_p \leq r \leq r_{p+1} \\ 0 & \text{for } r > r_{p+1} \end{cases} \quad (70)$$

Now substituting the trial functions into Equation (69) yields:

$$\begin{aligned} & -\frac{\partial}{\partial z} \bar{D}^{10} \frac{\partial}{\partial z} \tilde{\Psi}_{00}^{(N+1)} - \frac{\partial}{\partial r} \bar{D}^{11} \frac{\partial}{\partial r} \tilde{\Psi}_{00}^{(N+1)} - \frac{1}{r} \bar{D}^{11} \frac{\partial}{\partial r} \tilde{\Psi}_{00}^{(N+1)} \\ & + \Sigma^{00} \tilde{\Psi}_{00}^{(N+1)} = \Sigma^f \tilde{\Psi}_{00}^{(N+1)} + \tilde{S}_{00}^{(N+1)} + \tilde{C}^{(N)} + V \tilde{\Psi}_{00}^{(N)} \\ & - \frac{\partial}{\partial z} D^{10} V \tilde{\Psi}_{10}^{(N)} - \frac{\partial}{\partial z} D^{10} \tilde{S}_{10}^{(N+1)} \\ & - \frac{\partial}{\partial r} D^{11} V \tilde{\Psi}_{11}^{(N)} - \frac{\partial}{\partial r} D^{11} \tilde{S}_{11}^{(N+1)} \\ & - \frac{1}{r} D^{11} V \tilde{\Psi}_{11}^{(N)} - \frac{1}{r} D^{11} \tilde{S}_{11}^{(N+1)} \end{aligned} \quad (71)$$

The Galerkin procedure can now be implemented. However, integration over the domain is now defined for a cylinder with a radius from 0 to  $R$  and a height from 0 to  $K$ . Therefore, the domain integration is,  $\int_0^K \int_0^R 2\pi r dr dz$ . Implementing this, the transport equation is now:

$$\begin{aligned} & - \int_0^K \int_0^R \frac{\partial}{\partial z} \bar{D}^{10} \frac{\partial}{\partial z} \tilde{\Psi}_{00}^{(N+1)} B_i(r) B_j(z) 2\pi r dr dz \\ & - \int_0^K \int_0^R \frac{\partial}{\partial r} \bar{D}^{11} \frac{\partial}{\partial r} \tilde{\Psi}_{00}^{(N+1)} B_i(r) B_j(z) 2\pi r dr dz \\ & - \int_0^K \int_0^R \frac{1}{r} \bar{D}^{11} \frac{\partial}{\partial r} \tilde{\Psi}_{00}^{(N+1)} B_i(r) B_j(z) 2\pi r dr dz \\ & + \int_0^K \int_0^R \Sigma^{00} \tilde{\Psi}_{00}^{(N+1)} B_i(r) B_j(z) 2\pi r dr dz \\ & = \int_0^K \int_0^R \Sigma^f \tilde{\Psi}_{00}^{(N+1)} B_i(r) B_j(z) 2\pi r dr dz \end{aligned}$$

$$\begin{aligned}
& + \int_0^K \int_0^R \tilde{S}_{00}^{(N+1)} B_i(r) B_j(z) 2\pi r dr dz \\
& + \int_0^K \int_0^R \tilde{C}^{(N)} B_i(r) B_j(z) 2\pi r dr dz \\
& + \int_0^K \int_0^R V \tilde{\Psi}_{00}^{(N)} B_i(r) B_j(z) 2\pi r dr dz \\
& - \int_0^K \int_0^R \frac{\partial}{\partial z} D^{10} V \tilde{\Psi}_{10}^{(N)} B_i(r) B_j(z) 2\pi r dr dz \\
& - \int_0^K \int_0^R \frac{\partial}{\partial z} D^{10} \tilde{S}_{10}^{(N+1)} B_i(r) B_j(z) 2\pi r dr dz \\
& - \int_0^K \int_0^R \frac{\partial}{\partial r} D^{11} V \tilde{\Psi}_{11}^{(N)} B_i(r) B_j(z) 2\pi r dr dz \\
& - \int_0^K \int_0^R \frac{\partial}{\partial r} D^{11} \tilde{S}_{11}^{(N+1)} B_i(r) B_j(z) 2\pi r dr dz \\
& - \int_0^K \int_0^R \frac{1}{r} D^{11} V \tilde{\Psi}_{11}^{(N)} B_i(r) B_j(z) 2\pi r dr dz \\
& - \int_0^K \int_0^R \frac{1}{r} D^{11} \tilde{S}_{11}^{(N+1)} B_i(r) B_j(z) 2\pi r dr dz
\end{aligned} \tag{72}$$

Green's theorem is again used to integrate the streaming terms by parts. This reduces the continuity requirement of the trial functions and implements the natural boundary conditions. And since each element carries the boundary conditions with them, the integrations may be designated over each element. Let  $e_r$  indicate integration over the elements in the  $r$  direction and let  $e_z$  indicate integration over the elements of the  $z$  direction. Implementing the Galerkin procedure, the transport equation is now:

$$\begin{aligned}
& \int_{e_z} \int_{e_r} \bar{D}^{10} \frac{\partial \tilde{\Psi}_{00}^{(N+1)}}{\partial z} \frac{\partial B_j(z)}{\partial z} B_i(r) r dr dz \\
& + \int_{e_z} \int_{e_r} \bar{D}^{11} \frac{\partial \tilde{\Psi}_{00}^{(N+1)}}{\partial r} \frac{\partial B_i(r)}{\partial r} B_j(z) r dr dz
\end{aligned}$$

$$\begin{aligned}
& + \int_{c_z} \int_{c_r} \bar{D}^{11} \frac{\partial \tilde{\Psi}_{00}^{(N+1)}}{\partial r} B_i(r) B_j(z) dr dz \\
& + \int_{c_z} \int_{c_r} \bar{D}^{11} \tilde{\Psi}_{00}^{(N+1)} \frac{\partial B_i(r)}{\partial r} B_j(z) dr dz \\
& + \int_{c_z} \int_{c_r} \Sigma^{00} \tilde{\Psi}_{00}^{(N+1)} B_i(r) B_j(z) r dr dz \\
& = \int_{c_z} \int_{c_r} \Sigma^f \tilde{\Psi}_{00}^{(N+1)} B_i(r) B_j(z) r dr dz \\
& + \int_{c_z} \int_{c_r} \tilde{S}_{00}^{(N+1)} B_i(r) B_j(z) r dr dz \\
& + \int_{c_z} \int_{c_r} \tilde{C}^{(N)} B_i(r) B_j(z) r dr dz \\
& + \int_{c_z} \int_{c_r} V \tilde{\Psi}_{00}^{(N)} B_i(r) B_j(z) r dr dz \\
& + \int_{c_z} \int_{c_r} D^{10} V \tilde{\Psi}_{10}^{(N)} B_i(r) \frac{\partial B_j(z)}{\partial z} r dr dz \\
& + \int_{c_z} \int_{c_r} D^{10} \tilde{S}_{10}^{(N+1)} B_i(r) \frac{\partial B_j(z)}{\partial z} r dr dz \\
& + \int_{c_z} \int_{c_r} D^{11} V \tilde{\Psi}_{11}^{(N)} \frac{\partial B_i(r)}{\partial r} B_j(z) r dr dz \\
& + \int_{c_z} \int_{c_r} D^{11} \tilde{S}_{11}^{(N+1)} \frac{\partial B_i(r)}{\partial r} B_j(z) r dr dz \\
& + \int_{c_z} D^{11} \left[ B_i(r) \tilde{\Psi}_{00}^{(N+1)} \right]_{r=R} B_j(z) dz \\
& - \int_{c_z} D^{11} \left[ B_i(r) \tilde{\Psi}_{00}^{(N+1)} \right]_{r=0} B_j(z) dz \\
& - \int_{c_r} \left[ B_j(z) \tilde{\Psi}_{10}^{(N+1)} \right]_{z=K} B_i(r) r dr \\
& + \int_{c_r} \left[ B_j(z) \tilde{\Psi}_{10}^{(N+1)} \right]_{z=0} B_i(r) r dr \\
& - \int_{c_z} \left[ r B_i(r) \tilde{\Psi}_{11}^{(N+1)} \right]_{r=R} B_j(z) dz
\end{aligned} \tag{73}$$

Appendix B gives the integrating summaries. Again, Marshak vacuum boundary conditions are implemented to substitute for the  $\Psi_{10,i}^{(N+1)}$  and  $\Psi_{11,j}^{(N+1)}$  coefficients in

terms of  $\Psi_{00ij}^{(N+1)}$  coefficients. Using the Kronecker delta where  $p = i-1, i$ , and  $i+1$  and  $q = j-1, j$ , and  $j+1$  produces:

$$\begin{aligned}
& \left\{ \left( \frac{1}{2} \right) \Psi_{00i-1B}^{(N+1)} (R_1) + \left( \frac{1}{2} \right) \Psi_{00iB}^{(N+1)} (R_2) \right. \\
& + \left. \left( \frac{1}{2} \right) \Psi_{00iB}^{(N+1)} (R_3) + \left( \frac{1}{2} \right) \Psi_{00i+1B}^{(N+1)} (R_4) \right\} \delta_{pB} \\
& + \left\{ \left( \frac{1}{2} \right) \Psi_{00i-1,1}^{(N+1)} (R_1) + \left( \frac{1}{2} \right) \Psi_{00i,1}^{(N+1)} (R_2) \right. \\
& + \left. \left( \frac{1}{2} \right) \Psi_{00i,1}^{(N+1)} (R_3) + \left( \frac{1}{2} \right) \Psi_{00i+1,1}^{(N+1)} (R_4) \right\} \delta_{p1} \\
& + \left\{ \left( \frac{1}{2} \right) \Psi_{00Aj-1}^{(N+1)} (R) \left( \frac{h_{j-1}}{6} \right) + \left( \frac{1}{2} \right) \Psi_{00Aj}^{(N+1)} (R) \left( \frac{h_{j-1}}{3} \right) \right. \\
& + \left. \left( \frac{1}{2} \right) \Psi_{00Aj}^{(N+1)} (R) \left( \frac{h_j}{3} \right) + \left( \frac{1}{2} \right) \Psi_{00Aj+1}^{(N+1)} (R) \left( \frac{h_j}{6} \right) \right\} \delta_{Aq} \\
& - \left\{ \left( \frac{h_{j-1}}{6} \right) \bar{D}_{A-1j-1}^{11} \Psi_{00Aj-1}^{(N+1)} \right. \\
& + \left. \left[ \left( \frac{h_{j-1}}{3} \right) \bar{D}_{A-1j-1}^{11} + \left( \frac{h_j}{3} \right) \bar{D}_{A-1j}^{11} \right] \Psi_{00Aj}^{(N+1)} \right. \\
& + \left. \left( \frac{h_j}{6} \right) \bar{D}_{A-1j}^{11} \Psi_{00Aj+1}^{(N+1)} \right\} \delta_{Aq} \\
& + \left\{ \left( \frac{h_{j-1}}{6} \right) \bar{D}_{1j-1}^{11} \Psi_{00i,j-1}^{(N+1)} \right. \\
& + \left. \left[ \left( \frac{h_{j-1}}{3} \right) \bar{D}_{1j-1}^{11} + \left( \frac{h_j}{3} \right) \bar{D}_{1j}^{11} \right] \Psi_{00i,j}^{(N+1)} \right. \\
& + \left. \left( \frac{h_j}{6} \right) \bar{D}_{1j}^{11} \Psi_{00i,j+1}^{(N+1)} \right\} \delta_{1q} \\
& + \left[ \bar{D}_{i-1,j-1}^{10} \left( \frac{-1}{h_{j-1}} \right) (R_1) + \bar{D}_{i-1,j-1}^{11} \left( \frac{h_{j-1}}{6} \right) (R_5) \right. \\
& + \left. \left( \Sigma_{i-1,j-1}^{00} - \Sigma_{i-1,j-1}^f \right) \left( \frac{h_{j-1}}{6} \right) (R_1) \right] \Psi_{00i-1,j-1}^{(N+1)} \\
& + \left[ \left( \frac{1}{h_{j-1}} \right) (R_1) \bar{D}_{i-1,j-1}^{10} + \left( \frac{1}{h_j} \right) (R_1) \bar{D}_{i-1,j}^{10} \right. \\
& + \left. \left( \frac{h_{j-1}}{3} \right) (R_5) \bar{D}_{i-1,j-1}^{11} + \left( \frac{h_j}{3} \right) (R_5) \bar{D}_{i-1,j}^{11} \right. \\
& + \left. \left( \frac{h_{j-1}}{3} \right) (R_1) \left( \Sigma_{i-1,j-1}^{00} - \Sigma_{i-1,j-1}^f \right) \right. \\
& + \left. \left( \frac{h_j}{3} \right) (R_1) \left( \Sigma_{i-1,j}^{00} - \Sigma_{i-1,j}^f \right) \right] \Psi_{00i-1,j}^{(N+1)}
\end{aligned}$$

$$\begin{aligned}
& + \left[ \left( \frac{-1}{h_j} \right) (R_1) \bar{D}_{i-1j}^{10} + \left( \frac{h_j}{6} \right) (R_5) \bar{D}_{i-1j}^{11} \right. \\
& + \left. \left( \frac{h_j}{6} \right) (R_1) (\Sigma_{i-1j}^{00} - \Sigma_{i-1j}^f) \right] \Psi_{00i-1j+1}^{(N+1)} \\
& + \left[ \left( \frac{-1}{h_{j-1}} \right) (R_2) \bar{D}_{i-1j-1}^{10} + \left( \frac{-1}{h_{j-1}} \right) (R_3) \bar{D}_{ij-1}^{10} \right. \\
& + \left( \frac{h_{j-1}}{6} \right) (R_6) \bar{D}_{i-1j-1}^{11} + \left( \frac{h_{j-1}}{6} \right) (R_7) \bar{D}_{ij-1}^{11} \\
& + \left( \frac{h_{j-1}}{6} \right) \bar{D}_{i-1j-1}^{11} + \left( \frac{-h_{j-1}}{6} \right) \bar{D}_{ij-1}^{11} \\
& + \left( \frac{h_{j-1}}{6} \right) (R_2) (\Sigma_{i-1j-1}^{00} - \Sigma_{i-1j-1}^f) \\
& + \left. \left( \frac{h_{j-1}}{6} \right) (R_3) (\Sigma_{ij-1}^{00} - \Sigma_{ij-1}^f) \right] \Psi_{00ij-1}^{(N+1)} \\
& + \left[ \left( \frac{1}{h_{j-1}} \right) (R_2) \bar{D}_{i-1j-1}^{10} + \left( \frac{1}{h_j} \right) (R_2) \bar{D}_{i-1j}^{10} \right. \\
& + \left( \frac{1}{h_{j-1}} \right) (R_3) \bar{D}_{ij-1}^{10} + \left( \frac{1}{h_j} \right) (R_3) \bar{D}_{ij}^{10} \\
& + \left( \frac{h_{j-1}}{3} \right) (R_6) \bar{D}_{i-1j-1}^{11} + \left( \frac{h_{j-1}}{3} \right) (R_7) \bar{D}_{ij-1}^{11} \\
& + \left( \frac{h_j}{3} \right) (R_6) \bar{D}_{i-1j}^{11} + \left( \frac{h_j}{3} \right) (R_7) \bar{D}_{ij}^{11} \\
& + \left( \frac{h_{j-1}}{3} \right) \bar{D}_{i-1j-1}^{11} + \left( \frac{-h_{j-1}}{3} \right) \bar{D}_{ij-1}^{11} + \left( \frac{h_j}{3} \right) \bar{D}_{i-1j}^{11} + \left( \frac{-h_j}{3} \right) \bar{D}_{ij}^{11} \\
& + \left( \frac{h_{j-1}}{3} \right) (R_2) (\Sigma_{i-1j-1}^{00} - \Sigma_{i-1j-1}^f) + \left( \frac{h_j}{3} \right) (R_2) (\Sigma_{i-1j}^{00} - \Sigma_{i-1j}^f) \\
& + \left( \frac{h_{j-1}}{3} \right) (R_3) (\Sigma_{ij-1}^{00} - \Sigma_{ij-1}^f) + \left( \frac{h_j}{3} \right) (R_3) (\Sigma_{ij}^{00} - \Sigma_{ij}^f) \right] \Psi_{00i,j}^{(N+1)} \\
& + \left[ \left( \frac{-1}{h_j} \right) (R_2) \bar{D}_{i-1j}^{10} + \left( \frac{-1}{h_j} \right) (R_3) \bar{D}_{ij}^{10} \right. \\
& + \left( \frac{h_j}{6} \right) (R_6) \bar{D}_{i-1j}^{11} + \left( \frac{h_j}{6} \right) (R_7) \bar{D}_{ij}^{11} \\
& + \left( \frac{h_j}{6} \right) \bar{D}_{i-1j}^{11} + \left( \frac{-h_j}{6} \right) \bar{D}_{ij}^{11} \\
& + \left. \left( \frac{h_j}{6} \right) (R_2) (\Sigma_{i-1j}^{00} - \Sigma_{i-1j}^f) + \left( \frac{h_j}{6} \right) (R_3) (\Sigma_{ij}^{00} - \Sigma_{ij}^f) \right] \Psi_{00i,j+1}^{(N+1)} \\
& + \left[ \left( \frac{-1}{h_{j-1}} \right) (R_4) \bar{D}_{ij-1}^{10} + \left( \frac{h_{j-1}}{6} \right) (R_8) \bar{D}_{ij-1}^{11} \right.
\end{aligned}$$

$$\begin{aligned}
& + \left( \frac{h_{j-1}}{6} \right) (R_4) (\Sigma_{ij-1}^{00} - \Sigma_{ij-1}^f) \left] \Psi_{00i+1j-1}^{(N+1)} \right. \\
& + \left[ \left( \frac{1}{h_{j-1}} \right) (R_4) \overline{D}_{ij-1}^{10} + \left( \frac{1}{h_j} \right) (R_4) \overline{D}_{ij}^{10} \right. \\
& + \left( \frac{h_{j-1}}{3} \right) (R_8) \overline{D}_{ij-1}^{11} + \left( \frac{h_j}{3} \right) (R_8) \overline{D}_{ij}^{11} \\
& + \left( \frac{h_{j-1}}{3} \right) (R_4) (\Sigma_{ij-1}^{00} - \Sigma_{ij-1}^f) \\
& + \left( \frac{h_j}{3} \right) (R_4) (\Sigma_{ij}^{00} - \Sigma_{ij}^f) \left] \Psi_{00i+1j}^{(N+1)} \right. \\
& + \left[ \left( \frac{-1}{h_j} \right) (R_4) \overline{D}_{ij}^{10} + \left( \frac{h_j}{6} \right) (R_8) \overline{D}_{ij}^{11} \right. \\
& + \left( \frac{h_j}{6} \right) (R_4) (\Sigma_{ij}^{00} - \Sigma_{ij}^f) \left] \Psi_{00i+1j+1}^{(N+1)} \right. \\
& = \left( \frac{h_{j-1}}{6} \right) (R_1) [S_{00i-1j-1}^{(N+1)} + V \Psi_{00i-1j-1}^{(N)} + C_{i-1j-1}^{(N)}] \\
& + \left[ \left( \frac{h_{j-1}}{6} \right) (R_2) + \left( \frac{h_{j-1}}{6} \right) (R_3) \right] [S_{00ij-1}^{(N+1)} + V \Psi_{00ij-1}^{(N)} + C_{ij-1}^{(N)}] \\
& + \left( \frac{h_{j-1}}{6} \right) (R_4) [S_{00i+1j-1}^{(N+1)} + V \Psi_{00i+1j-1}^{(N)} + C_{i+1j-1}^{(N)}] \\
& + \left[ \left( \frac{h_{j-1}}{3} \right) (R_1) + \left( \frac{h_j}{3} \right) (R_1) \right] [S_{00i-1j}^{(N+1)} + V \Psi_{00i-1j}^{(N)} + C_{i-1j}^{(N)}] \\
& + \left[ \left( \frac{h_{j-1}}{3} \right) (R_2) + \left( \frac{h_j}{3} \right) (R_2) + \left( \frac{h_{j-1}}{3} \right) (R_3) + \left( \frac{h_j}{3} \right) (R_3) \right] \\
& \quad \cdot [S_{00ij}^{(N+1)} + V \Psi_{00ij}^{(N)} + C_{ij}^{(N)}] \\
& + \left[ \left( \frac{h_{j-1}}{3} \right) (R_4) + \left( \frac{h_j}{3} \right) (R_4) \right] [S_{00i+1j}^{(N+1)} + V \Psi_{00i+1j}^{(N)} + C_{i+1j}^{(N)}] \\
& + \left( \frac{h_j}{6} \right) (R_1) [S_{00i-1j+1}^{(N+1)} + V \Psi_{00i-1j+1}^{(N)} + C_{i-1j+1}^{(N)}] \\
& + \left[ \left( \frac{h_j}{6} \right) (R_2) + \left( \frac{h_j}{6} \right) (R_3) \right] [S_{00ij+1}^{(N+1)} + V \Psi_{00ij+1}^{(N)} + C_{ij+1}^{(N)}] \\
& + \left( \frac{h_j}{6} \right) (R_4) [S_{00i+1j+1}^{(N+1)} + V \Psi_{00i+1j+1}^{(N)} + C_{i+1j+1}^{(N)}] \\
& + \left( \frac{1}{2} \right) (R_1) D_{i-1j-1}^{10} [V \Psi_{10i-1j-1}^{(N)} + S_{10i-1j-1}^{(N+1)}] \\
& + \left[ \left( \frac{1}{2} \right) (R_2) D_{i-1j-1}^{10} + \left( \frac{1}{2} \right) (R_3) D_{ij-1}^{10} \right] [V \Psi_{10ij-1}^{(N)} + S_{10ij-1}^{(N+1)}]
\end{aligned}$$

$$\begin{aligned}
& + \left(\frac{1}{2}\right) (R_4) D_{i-1}^{10} [V \Psi_{10i+1j-1}^{(N)} + S_{10i+1j-1}^{(N+1)}] \\
& + \left[\left(\frac{1}{2}\right) (R_1) D_{i-1j-1}^{10} + \left(\frac{-1}{2}\right) (R_1) D_{i-1j}^{10}\right] [V \Psi_{10i-1j}^{(N)} + S_{10i-1j}^{(N+1)}] \\
& + \left[\left(\frac{1}{2}\right) (R_2) D_{i-1j-1}^{10} + \left(\frac{-1}{2}\right) (R_2) D_{i-1j}^{10}\right] \\
& + \left(\frac{1}{2}\right) (R_3) D_{ij-1}^{10} + \left(\frac{-1}{2}\right) (R_3) D_{ij}^{10} [V \Psi_{10ij}^{(N)} + S_{10ij}^{(N+1)}] \\
& + \left[\left(\frac{1}{2}\right) (R_4) D_{ij-1}^{10} + \left(\frac{-1}{2}\right) (R_4) D_{ij}^{10}\right] [V \Psi_{10i+1j}^{(N)} + S_{10i+1j}^{(N+1)}] \\
& + \left(\frac{-1}{2}\right) (R_1) D_{i-1j}^{10} [V \Psi_{10i-1j+1}^{(N)} + S_{10i-1j+1}^{(N+1)}] \\
& + \left[\left(\frac{-1}{2}\right) (R_2) D_{i-1j}^{10} + \left(\frac{-1}{2}\right) (R_3) D_{ij}^{10}\right] [V \Psi_{10ij+1}^{(N)} + S_{10ij+1}^{(N+1)}] \\
& + \left(\frac{-1}{2}\right) (R_4) D_{ij}^{10} [V \Psi_{10i+1j+1}^{(N)} + S_{10i+1j+1}^{(N+1)}] \\
& + \left(\frac{h_{j-1}}{6}\right) (R_9) D_{i-1j-1}^{11} [V \Psi_{11i-1j-1}^{(N)} + S_{11i-1j-1}^{(N+1)}] \\
& + \left[\left(\frac{h_{j-1}}{6}\right) (R_{10}) D_{i-1j-1}^{11} + \left(\frac{h_{j-1}}{6}\right) (R_{11}) D_{ij-1}^{11}\right] [V \Psi_{11i-1j}^{(N)} + S_{11i-1j}^{(N+1)}] \\
& + \left(\frac{h_{j-1}}{6}\right) (R_{12}) D_{ij-1}^{11} [V \Psi_{11i+1j-1}^{(N)} + S_{11i+1j-1}^{(N+1)}] \\
& + \left[\left(\frac{h_{j-1}}{3}\right) (R_9) D_{i-1j}^{11} + \left(\frac{h_j}{3}\right) (R_9) D_{i-1j}^{11}\right] [V \Psi_{11i-1j}^{(N)} + S_{11i-1j}^{(N+1)}] \\
& + \left[\left(\frac{h_{j-1}}{3}\right) (R_{10}) D_{i-1j-1}^{11} + \left(\frac{h_j}{3}\right) (R_{10}) D_{i-1j}^{11}\right] \\
& + \left(\frac{h_{j-1}}{3}\right) (R_{11}) D_{ij-1}^{11} + \left(\frac{h_j}{3}\right) (R_{11}) D_{ij}^{11} \\
& \quad \cdot [V \Psi_{11ij}^{(N)} + S_{11ij}^{(N+1)}] \\
& + \left[\left(\frac{h_{j-1}}{3}\right) (R_{12}) D_{ij-1}^{11} + \left(\frac{h_j}{3}\right) (R_{12}) D_{ij}^{11}\right] [V \Psi_{11i+1j}^{(N)} + S_{11i+1j}^{(N+1)}] \\
& + \left(\frac{h_j}{6}\right) (R_9) D_{i-1j}^{11} [V \Psi_{11i-1j+1}^{(N)} + S_{11i-1j+1}^{(N+1)}] \\
& + \left[\left(\frac{h_j}{6}\right) (R_{10}) D_{i-1j}^{11} + \left(\frac{h_j}{6}\right) (R_{11}) D_{ij}^{11}\right] [V \Psi_{11ij+1}^{(N)} + S_{11ij+1}^{(N+1)}] \\
& + \left(\frac{h_j}{6}\right) (R_{12}) D_{ij}^{11} [V \Psi_{11i+1j+1}^{(N)} + S_{11i+1j+1}^{(N+1)}]
\end{aligned} \tag{74}$$

This equation will also produce a block matrix equation with nine diagonals. Now we will address the solution techniques to solve Equations (61) and (74).

## 5 Solution Technique

Using Equation (61) or (74) produces a block matrix equation as show in the example in Figure 4. The coefficient matrix,  $A$ , will always have nine full diagonals. For the 16 by 16 example shown, there were 100 nonzero entries in  $A$ . That means that 156 entries contain nothing but zeros. Recall that each entry in  $A$  is itself a  $G$  by  $G$  matrix representing  $G$  energy groups. Storage of all those zero matrices would be very inefficient. Therefore, FMP2DT uses some storage schemes to avoid using excessive computer memory. And because this system can be extremely sparse and large, depending on the number of mesh points and energy groups selected, FMP2DT used some special algorithms to calculate a solution. The following is information, including some background, concerning FMP2DT's solution algorithm.

If  $A \in \mathbf{R}^{n \times n}$  is a symmetric positive definite matrix, then a lower triangular matrix  $G \in \mathbf{R}^{n \times n}$  exist with positive diagonal entries such that  $A = G G^T$ . Splitting  $A$  like this is known as the Cholesky decomposition of the matrix  $A$ . To solve the system  $Ax = b$  using a Cholesky algorithm entails computing  $A = G G^T$  and then solving  $Gy = b$  and then  $G^T x = y$  [Ref. 18]. This solution technique is stable and efficient for solving large banded systems. This solution technique is called factoring the coefficient matrix  $A$ , and is referred to as a direct method of solution.

However, for very large and sparse systems, which could be our case, direct methods are often not efficient enough. For a linear system, iterative methods are more suitable. One iterative method is call the conjugate gradient method [Ref. 18]. It involves minimizing a functional  $\phi(x)$  such that,

$$\phi(x) = \frac{1}{2}x^T A x - x^T b.$$

If  $A$  is symmetric and positive definite, then minimizing the above expression is the same as solving for  $Ax = b$  [Ref. 18]. But convergence of a steepest descent



algorithm may be extremely slow. Therefore, preconditioning  $A$  is desirable to speed convergence. One preconditioning strategy is developing an incomplete Cholesky factorization of  $A$ . This involves calculation of some lower triangular matrix that is somewhat close to the actual Cholesky lower triangle matrix  $G$  [Ref. 18].

This solution technique FMP2DT uses to do this is the *incomplete Cholesky conjugate gradient* algorithm [Ref. 33]. Two iteration schemes are used. The inner iterations are over the spatial mesh points. The outer iterations are over the specified energy groups.

Now we examine one of the important features of FMP2DT. FMP2DT has the ability to calculate a delayed  $\chi$  spectrum if that spectrum is not known. If it is known, then it may be entered in the input deck. However, in most cases, these values are not easily found. Therefore, the next section shows how FMP2DT calculates these values for the user.

## 6 Calculation of $\chi_k^g$

In the multigroup derivations, Equation (27) has  $\chi$  parameters for both prompt and delayed neutrons. Most cross section sets contain information defining  $\chi_p^g$ , but they do not define  $\chi_k^g$ . If values for  $\chi_k^g$  are known, then they may be entered in FMP2DT's 15\*\* array in the input deck. If this array is filled with zeros, and FMP2DT is running a fission problem, then an internal flag is triggered that causes FMP2DT to assume that the user does not know these values. FMP2DT then proceeds to calculate them and continues the solution process.

The spectra for prompt neutrons are easily found in literature. There are many formulae that have been derived to fit the data mathematically by Watt, Cranberg, and others [Ref. 34] [Ref. 35]. Each analytical fit is due to examination of data over certain energy ranges [Ref. 36]. FMP2DT assumes a Maxwellian distribution function that is defined as [Ref. 30],

$$f(E) = \frac{2}{\sqrt{\pi}} \frac{1}{kT} \left[ \frac{E}{kT} \right]^{0.5} e^{-\frac{E}{kT}} \quad (75)$$

where  $k$  is Boltzmann's constant and  $T$  is the spectrum temperature (K). The average energy is given by

$$\bar{E} = \frac{3}{2} kT.$$

However, the delayed neutron spectrum is not as well established. Several different data exist with various uncertainty. FMP2DT assumes that delayed neutrons follow the same sort of Maxwellian distribution as prompt neutrons [Ref. 30]. Assuming that  $kT=1.29$  for prompt neutrons, or that  $kT=0.29$  for delayed neutrons [Ref. 31], Equation (75) may be used to calculate either a prompt or delayed spectrum. (The values for  $T$  above are for  $^{235}\text{U}$ , and  $kT$  is in MeV.)

For a  $\chi$  spectrum, we note that

$$\int_0^{\infty} \chi(E) dE = 1.0.$$

For a multigroup approximation,  $\chi^g$  is calculated as

$$\chi^g = \int_{E_g}^{E_{g+1}} \chi(E) dE.$$

FMP2DT calculates  $\chi_k^g$  likewise using an adaptive quadrature scheme based on Gauss-Kronrod algorithms. And as stated, changing the value for  $kT$  can cause an evaluation for a prompt  $\chi$  calculation. Also, if a *better* distribution function is desired, then a short function subprogram may be added to the code and the quadrature scheme can evaluate it.

Using a 47 neutron group structure shown in Tables 1 and 2, the following results were generated. First, a value of  $kT=1.29$  was used to generate a prompt  $\chi$  distribution shown in Figure 6. Note that although the neutron groups go to 17.33 MeV, the graph stops at 10 MeV. This is because the  $\chi_p^g$ s are approximately zero beyond that point. Using FMP2DT's quadrature scheme with a value of  $kT=0.29$ , Figure 7 was generated for the delayed  $\chi$ s. It was truncated at only 2.231 MeV because of the same reason as the prompt data.

It is important to notice that the delayed  $\chi$ s peak at lower energy groups than the prompt  $\chi$ s do. Also the prompt  $\chi$ s range over a much larger number of groups. This is expected since prompt fission neutrons tend to be born with higher energies than the delayed fission neutrons.

Now we want to establish FMP2DT's computational integrity. First, a comparison between flux shapes was made with a flux calculation by a two dimensional, two-group, space-time diffusion code called TWIGL. Then FMP2DT was benchmarked with some exact flux calculations in both slab and cylindrical geometries.

Group	Upper Bound (MeV)	Lower Bound (MeV)
1	1.7330E+01	1.4190E+01
2	1.4190E+01	1.2210E+01
3	1.2210E+01	1.0000E+01
4	1.0000E+01	8.6070E+00
5	8.6070E+00	7.4080E+00
6	7.4080E+00	6.0650E+00
7	6.0650E+00	4.9650E+00
8	4.9650E+00	3.6780E+00
9	3.6780E+00	3.0110E+00
10	3.0110E+00	2.7250E+00
11	2.7250E+00	2.4660E+00
12	2.4660E+00	2.3650E+00
13	2.3650E+00	2.3450E+00
14	2.3450E+00	2.2310E+00
15	2.2310E+00	1.9200E+00
16	1.9200E+00	1.6530E+00
17	1.6530E+00	1.3530E+00
18	1.3530E+00	1.0020E+00
19	1.0020E+00	8.2080E-01
20	8.2080E-01	7.4270E-01
21	7.4270E-01	6.0810E-01
22	6.0810E-01	4.9780E-01
23	4.9780E-01	3.6880E-01
24	3.6880E-01	2.9720E-01

Table 1: Part 1: 47 Neutron Group Structure

Group	Upper Bound (MeV)	Lower Bound (MeV)
25	2.9720E-01	1.8310E-01
26	1.8310E-01	1.1100E-01
27	1.1100E-01	6.7370E-02
28	6.7370E-02	4.0860E-02
29	4.0860E-02	3.1820E-02
30	3.1820E-02	2.6050E-02
31	2.6050E-02	2.4170E-02
32	2.4170E-02	2.1870E-02
33	2.1870E-02	1.5030E-02
34	1.5030E-02	7.1010E-03
35	7.1010E-03	3.3540E-03
36	3.3540E-03	1.5840E-03
37	1.5840E-03	4.5400E-04
38	4.5400E-04	2.1440E-04
39	2.1440E-04	1.0130E-04
40	1.0130E-04	3.7260E-05
41	3.7260E-05	1.0670E-05
42	1.0670E-05	5.0430E-06
43	5.0430E-06	1.8550E-06
44	1.8550E-06	8.7640E-07
45	8.7640E-07	4.1390E-07
46	4.1390E-07	9.9990E-08
47	9.9990E-08	1.0000E-11

Table 2: Part 2: 47 Neutron Group Structure

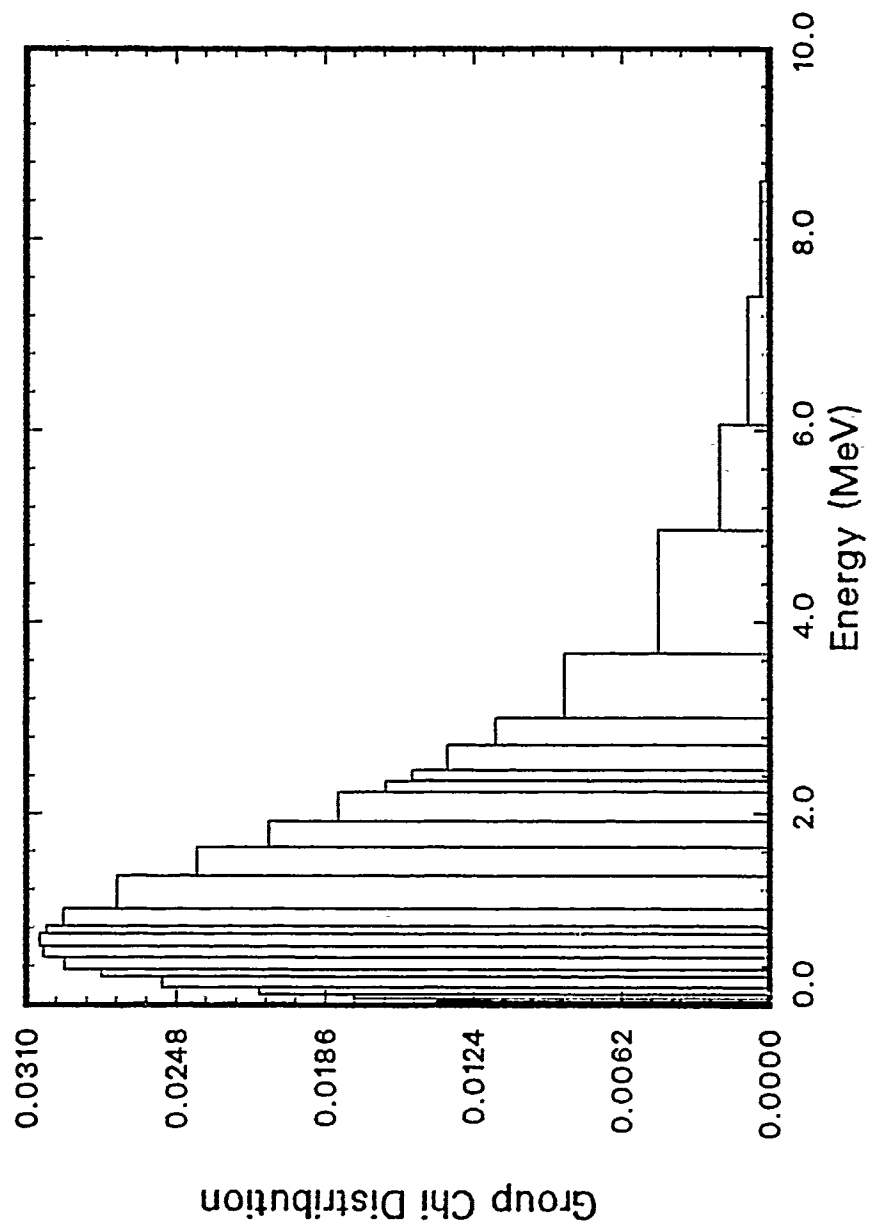


Figure 6: Prompt Group  $\chi$  for  $^{235}\text{U}$

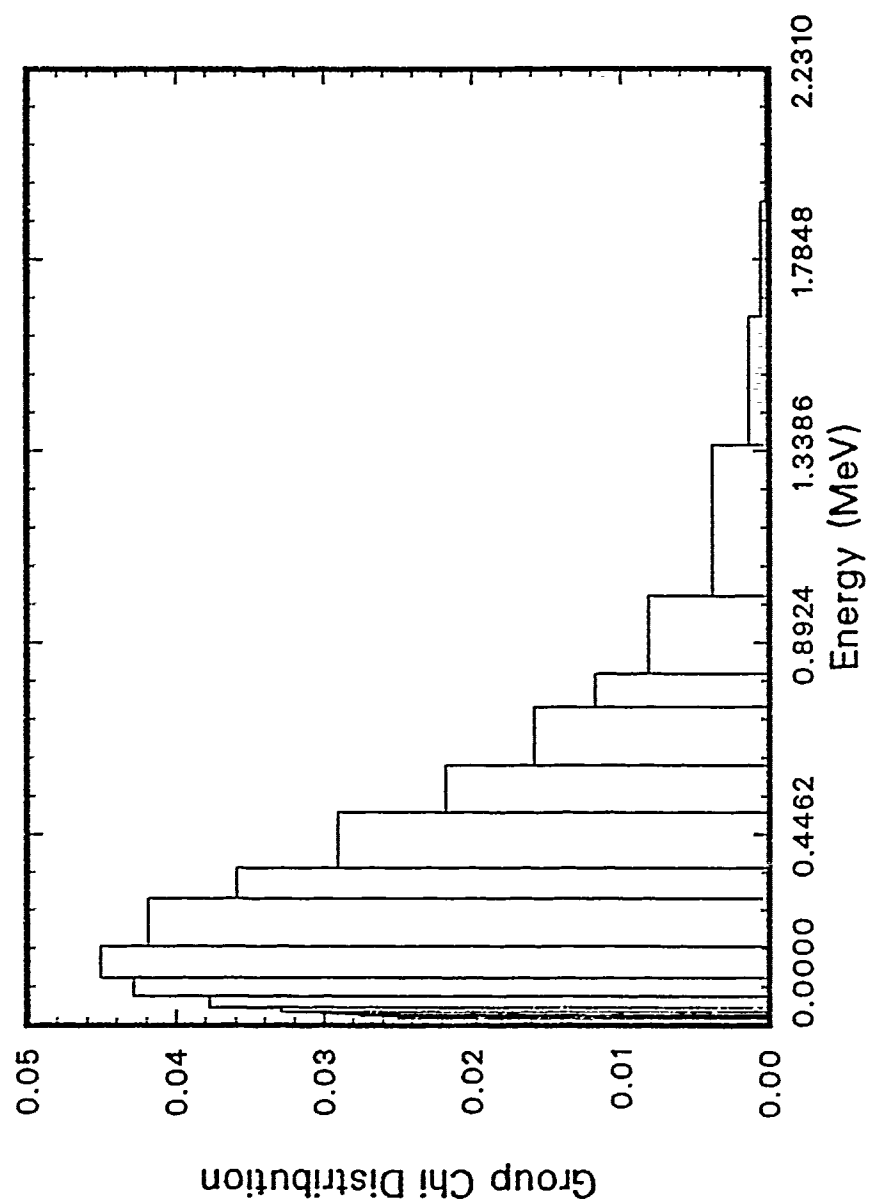


Figure 7: Delay Group  $\chi$  for  $^{235}\text{U}$

## 7 Code Benchmark

While there are many publications of time dependent neutron transport work available, it is extremely difficult to find a two-dimensional problem with a delayed neutron source so that FMP2DT can be benchmarked. While problems of this nature are often cited, the published results usually do not contain enough information about parameters and cross sectional data to reproduce them. In 1968, a technical report was published showing results for a time-dependent, two dimensional slab problem solved with a code called TWIGL [Ref. 28]. TWIGL is a two dimensional, two-group, space-time diffusion equation solver that incorporates temperature feedback.

TWIGL was used to compare FMP2DT's fast flux shape. To benchmark FMP2DT's computation accuracy, data in a report by B. D. Ganapol [Ref. 29] was used. First we show the results for the TWIGL comparison, and then two benchmarks using Ganapol's data for infinite RZ and XZ geometries.

### 7.1 TWIGL Comparison

TWIGL was used to compare FMP2DT's fast flux shape. This offered at least some sort of comparison between source vectors for the two codes, and both source vectors have a delayed neutron contribution in them. TWIGL is a diffusion code. It basically solved the following equations:

$$\begin{aligned} & \nabla \cdot D_1(\mathbf{r}, t) \nabla \phi_1(\mathbf{r}, t) - \Sigma_1(\mathbf{r}, t) \phi_1(\mathbf{r}, t) \\ & + (1 - \beta) [\nu \Sigma_{f_1}(\mathbf{r}, t) \phi_1(\mathbf{r}, t) + \nu \Sigma_{f_2}(\mathbf{r}, t) \phi_2(\mathbf{r}, t)] \\ & + \sum_{i=1}^I \lambda_i C_i(\mathbf{r}, t) = \frac{1}{v_1} \frac{\partial}{\partial t} \phi_1(\mathbf{r}, t) \end{aligned} \quad (76)$$



$$\nabla \cdot D_2(\mathbf{r}, t) \nabla \phi_2(\mathbf{r}, t) - \Sigma_2(\mathbf{r}, t) \phi_2(\mathbf{r}, t) + \Sigma_{r_1}(\mathbf{r}, t) \phi_1(\mathbf{r}, t) = \frac{1}{v_2} \frac{\partial}{\partial t} \phi_2(\mathbf{r}, t) \quad (77)$$

and

$$\frac{\partial}{\partial t} C_i(\mathbf{r}, t) = \beta^i [\nu \Sigma_{f_1}(\mathbf{r}, t) \phi_1(\mathbf{r}, t) + \nu \Sigma_{f_2}(\mathbf{r}, t) \phi_2(\mathbf{r}, t)] - \lambda_i C_i(\mathbf{r}, t), \quad i = 1, \dots, I \quad (78)$$

where  $\mathbf{r}$  represents  $x, z$  for slab geometry. The slab geometry for this problem is shown in Figure 8. The equations above are solved by TWIGL subject to *zero flux boundary conditions* on all external surfaces. At time  $t = 0$ , the reactor is critical, i.e.  $k_{\text{eff}} = 1.0$ . The initial flux is calculated using this steady state condition. TWIGL

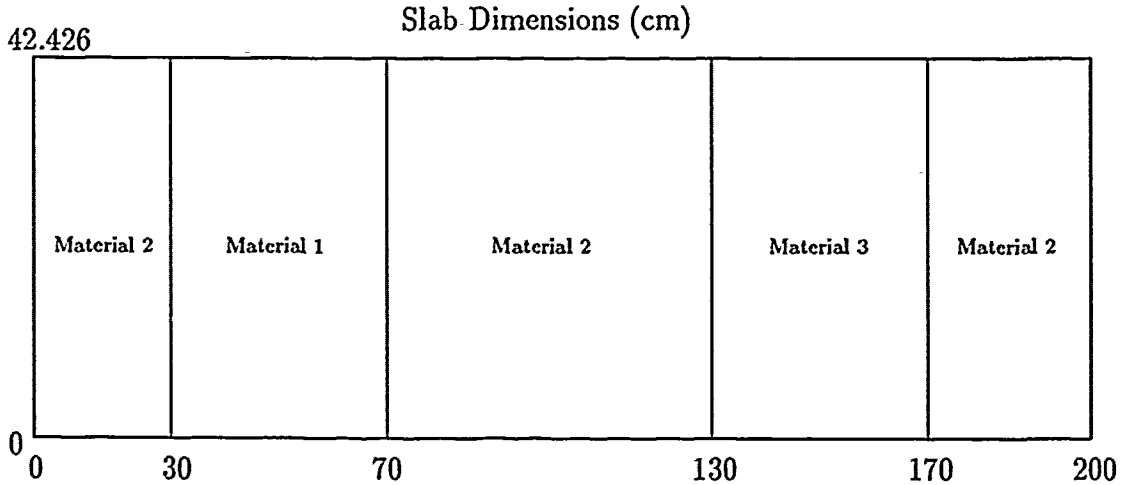


Figure 8: TWIGL Slab Geometry

discretizes the time dependent flux using a backward differencing scheme (for this problem) and a central differencing scheme for the precursor terms.

For most problems, FMP2DT reads cross sectional data from an input tape. However, data can be input directly. The input parameters used were derived from the data in the TWIGL report. Since TWIGL is a diffusion code, the values corresponding to the  $\Sigma_{s_1}^{g'-g}$  entries in FMP2DT's input deck are set to zero. This is known as the diffusion approximation for the  $P_1$  calculations. This is also done for

the calculation of the initial flux at time  $t = 0$ , which was calculated by FEMP2D. FMP2DT can calculate its own initial flux by using a very large  $\Delta t$ . This will cause all the  $\frac{1}{v_g \Delta t}$  terms to be approximately zero. From Appendix A, it is seen that all the time dependent terms will drop out. But using an initial flux calculated by FEMP2D is more cost effective since a large  $\Delta t$  in FMP2DT still entails some unnecessary calculations . like  $V \Psi_{00}^{(N)} = 0$ .

Table 3 compares the TWIGL and FMP2DT initial fluxes. Because of symmetry,

X(cm)	TWIGL	FEMP2D
10	6.26847E+13	5.9368E+13
20	1.92851E+14	1.8581E+14
30	5.34671E+14	5.5854E+14
40	9.37259E+14	9.4485E+14
50	1.08474E+15	1.0848E+15
60	9.39969E+14	9.4610E+14
70	5.39333E+14	5.6072E+14
80	2.00865E+14	1.9003E+14
90	8.28086E+13	7.1108E+13
100	5.38778E+13	4.3079E+13
110	8.28086E+13	7.1108E+13
120	2.00865E+14	1.9003E+14
130	5.39333E+14	5.6072E+14
140	9.39969E+14	9.4610E+14
150	1.08474E+15	1.0848E+15
160	9.37259E+14	9.4485E+14
170	5.34671E+14	5.5854E+14
180	1.92851E+14	1.8581E+14
190	6.26847E+13	5.9368E+13

Table 3: TWIGL and FMP2DT Initial Fast Fluxes

the flux data are for  $z \approx 14.142$  cm. There are no flux values given in Table 3 for  $x = 0$  or  $x = 200$  cm since TWIGL sets these values to zero. FMP2DT, however, does not set these fluxes to zero because it models a vacuum boundary condition. So the two codes should agree more for the interior mesh point flux calculations.

Figure 9 shows the plot of the TWIGL flux at time  $t = 0$ .

The material mean free paths (MFP) are calculated in Appendix C and displayed in Table 4. It is obvious that mesh spacing with  $\Delta z = 14.142$  cm and  $\Delta x = 10$  cm, which was used in the TWIGL report, is much larger than these MFPs. This suggests that the thermal flux calculations could be suspect. Indeed, both the FEMP2D and FMP2DT calculations showed that the thermal flux shape varied greatly as finer mesh spacing was chosen. The fast energy group, with its longer MFPs, was the least affected by mesh spacing. Figure 10 shows the initial FMP2DT flux calculated by FEMP2D. It was done using the reported TWIGL mesh. To be sure that this mesh spacing was sufficient to define the fast flux, another FEMP2D run was made using twice the reported TWIGL mesh points. (The TWIGL  $\Delta x$  and  $\Delta z$  values were cut in half.) Figure 11 shows this result. There is no substantial change between the two FEMP2D fluxes.

Group	Materials 1 & 3	Material 2
1	4.1701 cm	3.5702 cm
2	1.5601 cm	2.1000 cm

Table 4: Material Mean Free Paths

TWIGL set the initial condition of the slab to be critical. Using TWIGL mesh spacing, FEMP2D calculated a  $k_{\text{eff}} = 1.01418$ , and using twice as many mesh points, FEMP2D calculated a  $k_{\text{eff}} = 1.026858$ . So the initial calculations for the slab are very close for both codes. Therefore, the TWIGL mesh seems to be good enough to define the fast flux.

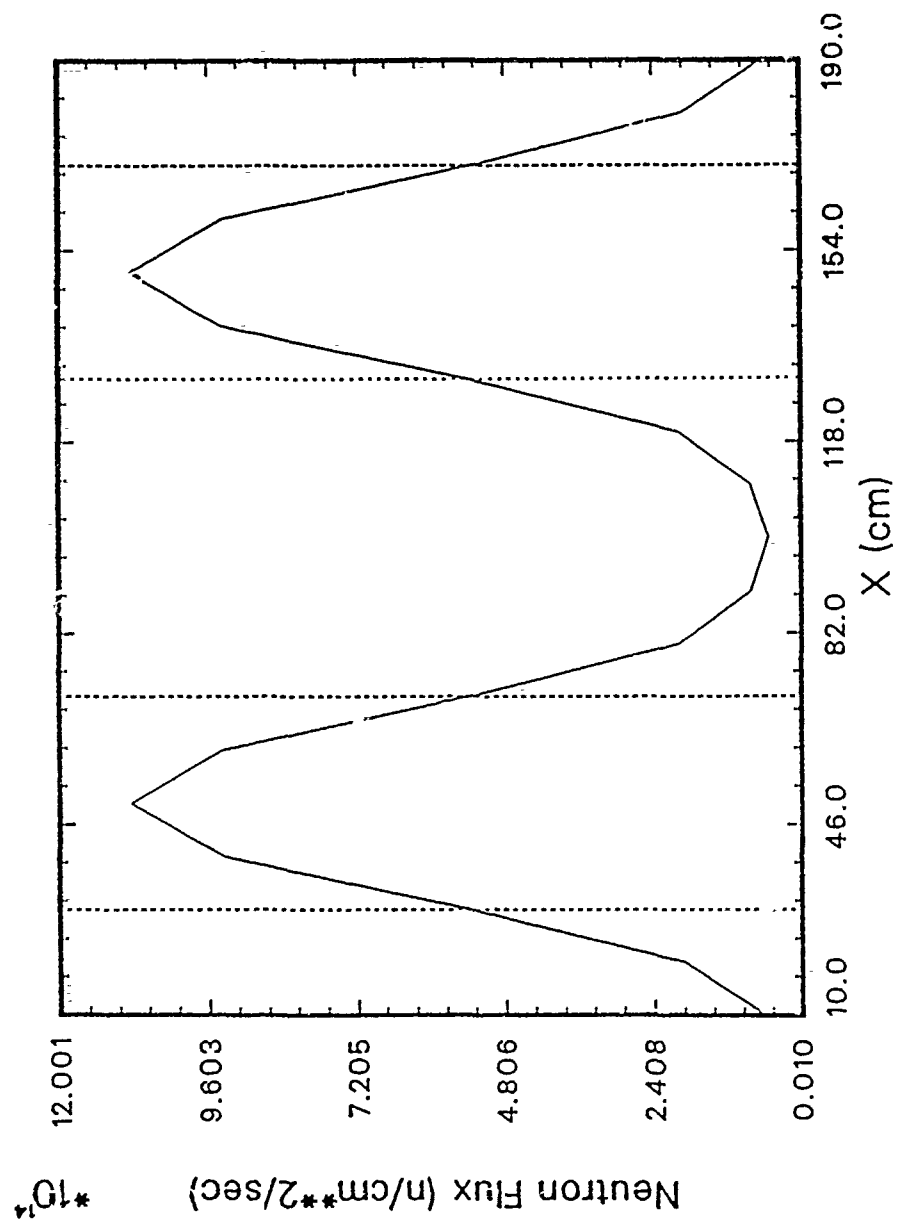


Figure 9: Initial TWIGL Flux

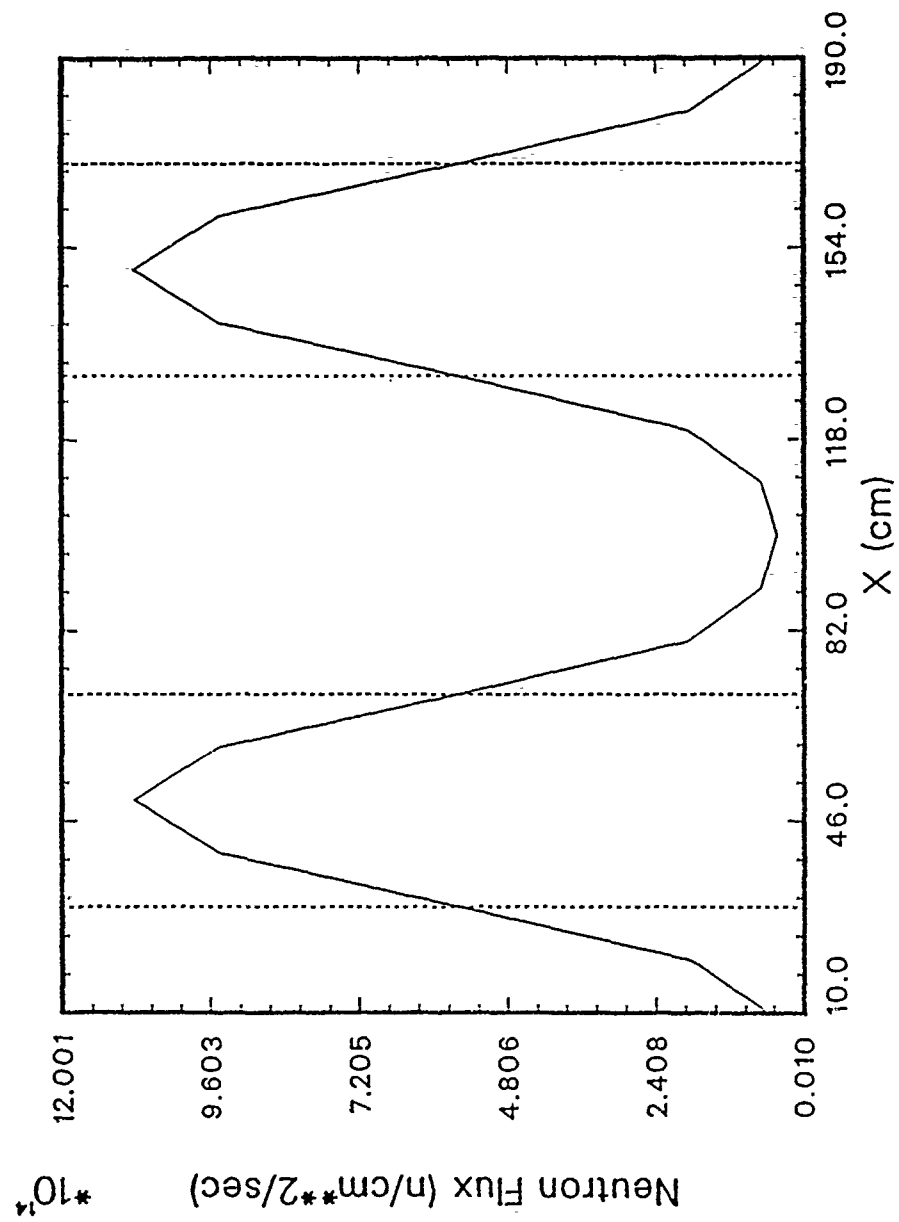


Figure 10: Initial FEMP2D Flux Using TWIGL Mesh Spacing

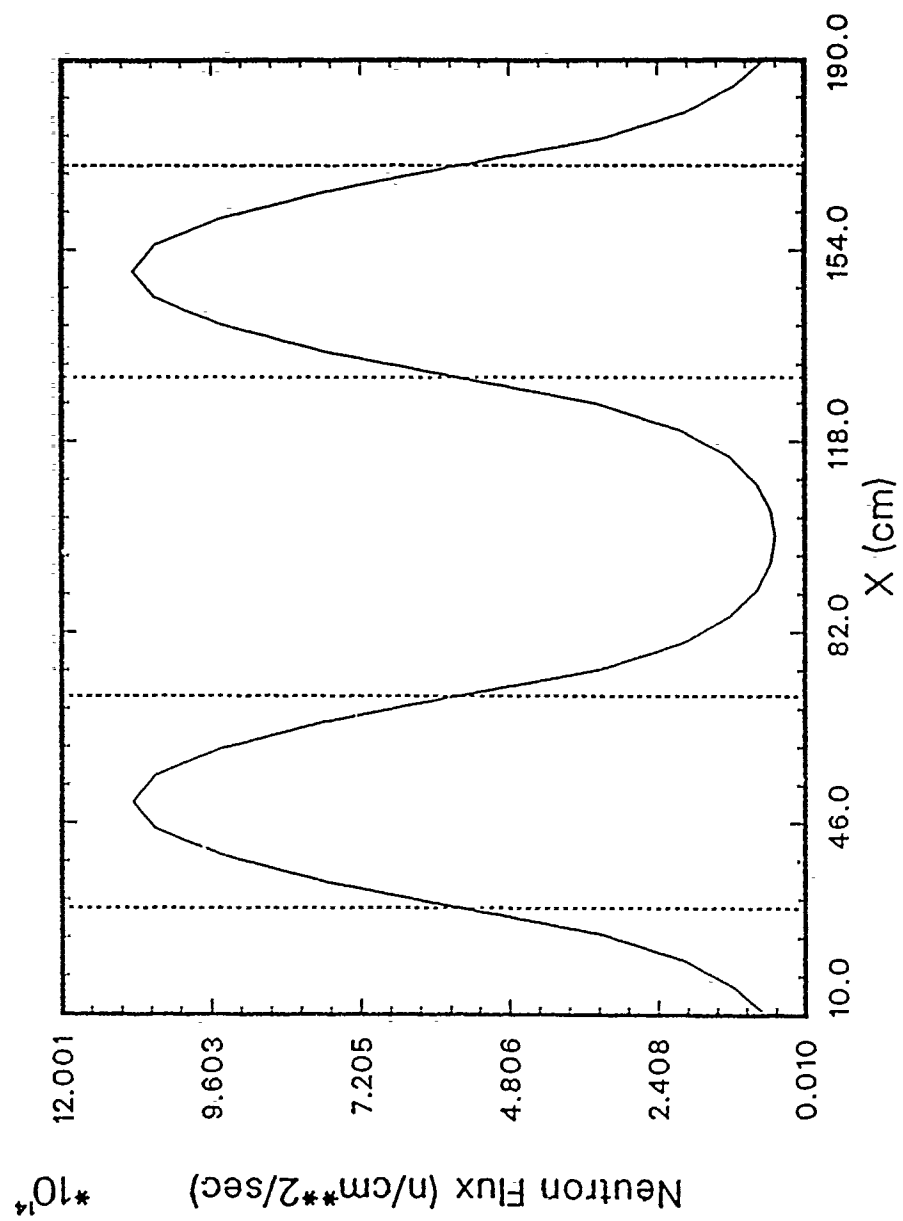


Figure 11: Initial FEMP2D Flux Using 2X TWIGL Mesh Spacing

### 7.1.1 Transient Calculations

The material cross sections changed with time due to two causes. The first has to do with a linearly changing cross section. Material 1 in Figure 8 differs from material 3 because material 1 has a time dependent thermal absorption shown in Figure 12. The second is due to temperature change. The TWIGL code assumes a

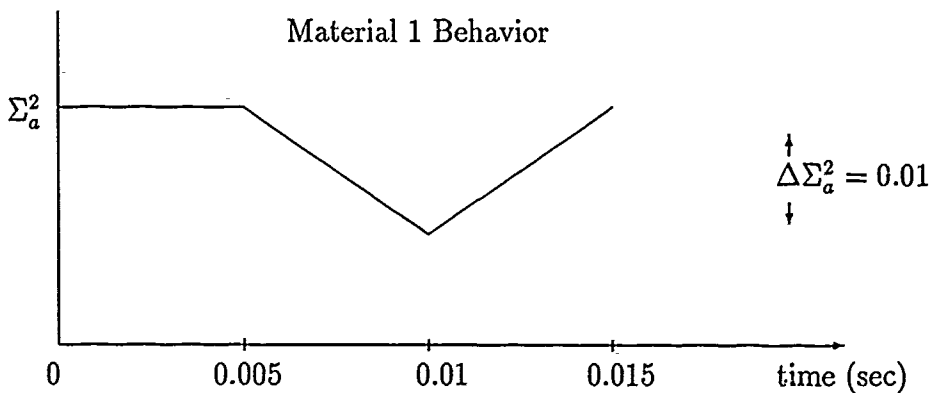


Figure 12: Time Dependent Thermal Absorption

coolant flow along the  $z$  axis. Since it sets the flux to zero on the slab surface, the coolant has no direct neutronic effect such as absorption, reflection, etc. However, it couples with a fission power calculation to establish a core and coolant temperature. The material cross sections are then adjusted for the change in temperature after each time step convergence. The time interval which the TWIGL had the smallest temperature change was chosen for this comparison. For time  $t = 0$  to  $t = 0.01$  sec there was no change in the core temperature. However, there was a small change in the coolant temperature. This is shown in Table 5. FMP2DT could have modeled this change if the TWIGL report had given the temperatures at the end of each time step. However, it did not. But the error should be very small since the coolant

Time (sec)	Zone 1	Zone 2	Zone 3	Zone 4	Zone 5
0.00	500.5680 °F	513.3180 °F	500.6400 °F	513.3180 °F	500.5680 °F
0.01	500.5681 °F	513.3188 °F	500.6399 °F	513.3181 °F	500.5680 °F

Table 5: Coolant Temperatures by Zone

temperature change for each zone is not significant.

The time dependent thermal absorption for material 1 can be described mathematically as,

$$\Sigma_a^2(t) = \begin{cases} 0.43 & \text{For } t \leq 0.005 \text{ sec} \\ 0.44 - 2t & \text{For } 0.005 < t \leq 0.01 \text{ sec} \end{cases} \quad (79)$$

Except for a small change due to temperature, the  $D_2$  TWIGL parameter remains constant in the interval. Therefore,  $\Sigma_t^2$  for the FMP2DT calculations remains constant. Since  $\Sigma_t^2 = \Sigma_a^2 + \Sigma_{s_0}^{2 \rightarrow 2}$ ,  $\Sigma_{s_0}^{2 \rightarrow 2}$  must be time dependent. This can be expressed mathematically as,

$$\Sigma_{s_0}^{2 \rightarrow 2}(t) = \begin{cases} 0.211 & \text{For } t \leq 0.005 \text{ sec} \\ 0.201 + 2t & \text{For } 0.005 < t \leq 0.01 \text{ sec} \end{cases} \quad (80)$$

Using Equations (79) and (80) above the cross section value for each parameter can be calculated for each time step. Then the value calculated for the present time step must be subtracted from the value for that parameter used during the last time step to obtain some  $\Delta\Sigma$ . That  $\Delta\Sigma$  goes into the input deck in the 20\*\*, 21\*\*, and 22\*\* arrays (shown in Appendix C). If a cross section has no time dependency, then its entries will be zero. (Note, the initial input into these arrays must contain the steady state values.)

The TWIGL flux at time  $t = 0.01$  sec is given in Table 6. The peaks occur at  $x = 50$  cm and  $x = 150$  cm, or in material zones 2 and 4 which are composed of material 1 and material 3 respectively. Figure 13 shows the TWIGL flux and the two distinct peaks.

The two peaks differ because of the change in the thermal absorption in ma-



X(cm)	$\phi$
10	1.835550+14
20	5.668937+14
30	1.578674+15
40	2.774679+15
50	3.211949+15
60	2.779915+15
70	1.587650+15
80	5.824532+14
90	2.229511+14
100	1.039940+14
110	1.038213+14
120	2.137265+14
130	5.582470+14
140	9.682363+14
150	1.115436+15
160	9.629778+14
170	5.491288+14
180	1.980289+14
190	6.435757+13

Table 6: TWIGL Flux at Time  $t = 0.01$  sec

terial 1. Thermal neutrons have a larger probability of inducing fission than fast neutrons. Neutrons emitted as a result of a fission event are high energy, or fast neutrons. Therefore, material absorption of thermal neutrons result in a decline of fission events. Conversely, less absorption increases the thermal neutron population, and increases fission events. More fission events then increase the fast neutron population.

It follows then that since the thermal absorption cross section decreases in material 1, more fission events occur there. This increases the fast neutron population, and causes a larger peak in material 1.

FMP2DT should also display the same shape. Figure 14 shows this to be the case. Figure 15 shows the results using twice the reported TWIGL mesh spacing.

In both cases, FMP2DT's flux shape was very similar to TWIGL's.

FMP2DT made twelve runs to insure that its flux shape was correctly defined. Table 7 shows the different configurations modeled. Runs 1 through 4 were done using the reported TWIGL mesh spacing. Note, that for runs 1 and 2 there are differences in the number of time intervals and  $\Delta t$ s. The parameters for run 1 are the same as those that TWIGL used for its calculations. TWIGL used one time interval with ten time steps to model from  $t = 0$  to  $t = 0.01$  sec, with each  $\Delta t = 0.001$  sec. From Figure 12 it is shown that between times  $t = 0$  and  $t = 0.005$  sec, there is no change in the thermal absorption cross section. TWIGL still used five time steps there even though no physical process was changing.

Run	Intervals	$\Delta t_1$ (sec)	$\Delta t_2$ (sec)	$\Delta x$ (cm)	$\Delta z$ (cm)	Total Steps
1	1	0.001	N/A	10.0	14.142	10
2	2	0.005	0.001	10.0	14.142	6
3	2	0.005	0.0005	10.0	14.142	11
4	2	0.005	0.00025	10.0	14.142	21
5	1	0.001	N/A	20.0	14.142	10
6	2	0.005	0.001	20.0	14.142	6
7	2	0.005	0.0005	20.0	14.142	11
8	2	0.005	0.00025	20.0	14.142	21
9	1	0.001	N/A	5.0	7.071	10
10	2	0.005	0.001	5.0	7.071	6
11	2	0.005	0.0005	5.0	7.071	11
12	2	0.005	0.00025	5.0	7.071	21

Table 7: FMP2DT Run Summary for TWIGL Comparison

For run 2, FMP2DT divided this problem into two intervals. The first went from  $t = 0$  to  $t = 0.005$  sec, and the second went from  $t = 0.005$  to  $0.01$  sec. However, for the first interval only one time step, with a  $\Delta t = 0.005$  sec, was used. The second interval used five time steps with  $\Delta t = 0.001$  sec. Thus, run 2 used a total of six time steps. The answers for runs 1 and 2 were exactly the same.

This demonstrates the ability for FMP2DT to yield a substantial savings in computational cost due to the fact that it has an implicit, numerical stable, time discretization. FMP2DT demonstrated this same characteristic for the other combinations of  $\Delta x$ ,  $\Delta z$  and  $\Delta t$  configurations shown in Table 7.

The differences in the peak magnitudes for the TWIGL and FMP2DT calculations, shown in Figure 14, yield no special concern since the large mesh spacing used makes the accuracy of either calculation questionable. However, since the flux shapes are similar, it can be said that the source vectors for the two codes were similar. This is significant because both codes modeled a precursor source.

We benchmark FMP2DT now using exact flux values. This will not only validate the ability of FMP2DT to obtain the correct flux shape, but will enhance its credibility for computational accuracy.

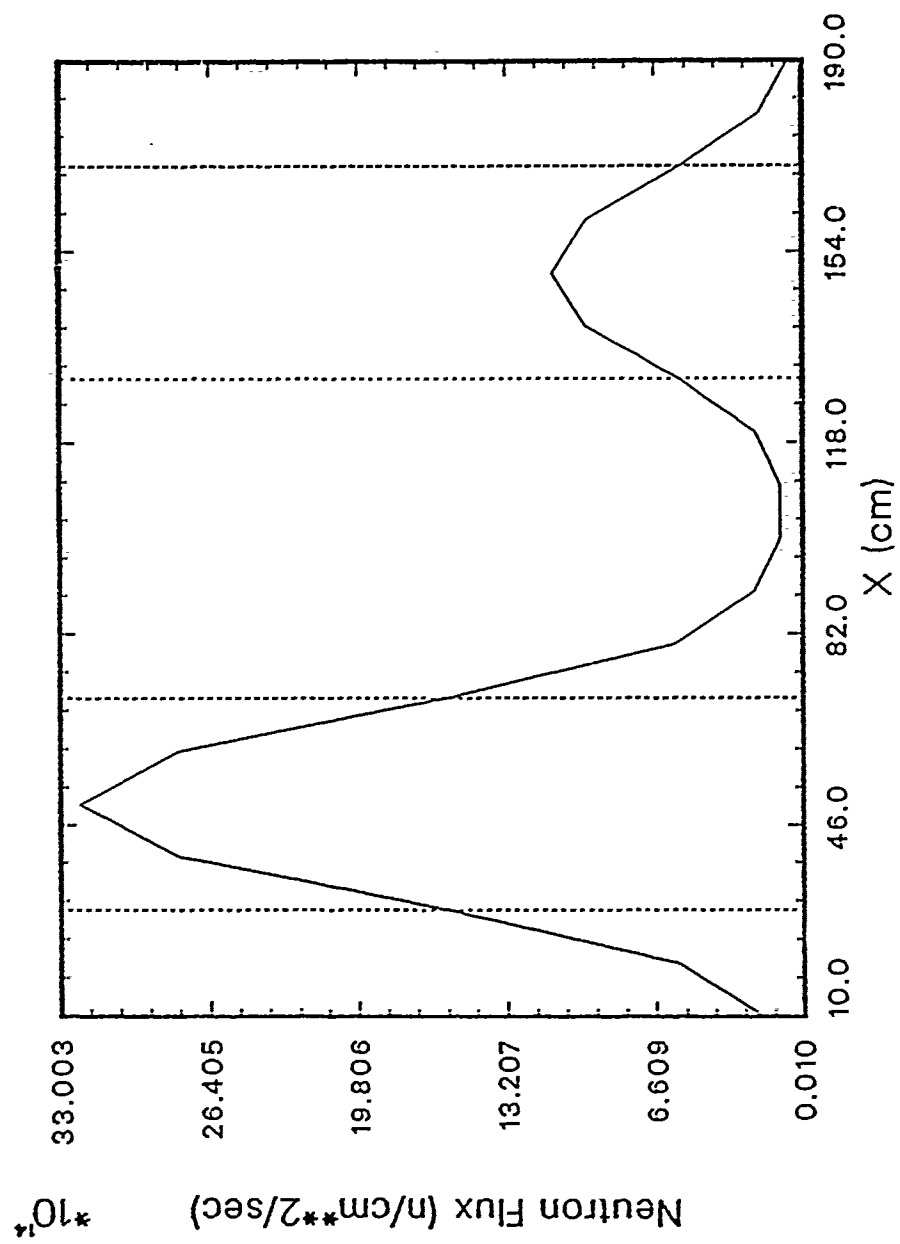


Figure 13: TWIGL Flux at Time  $t = 0.01$  sec

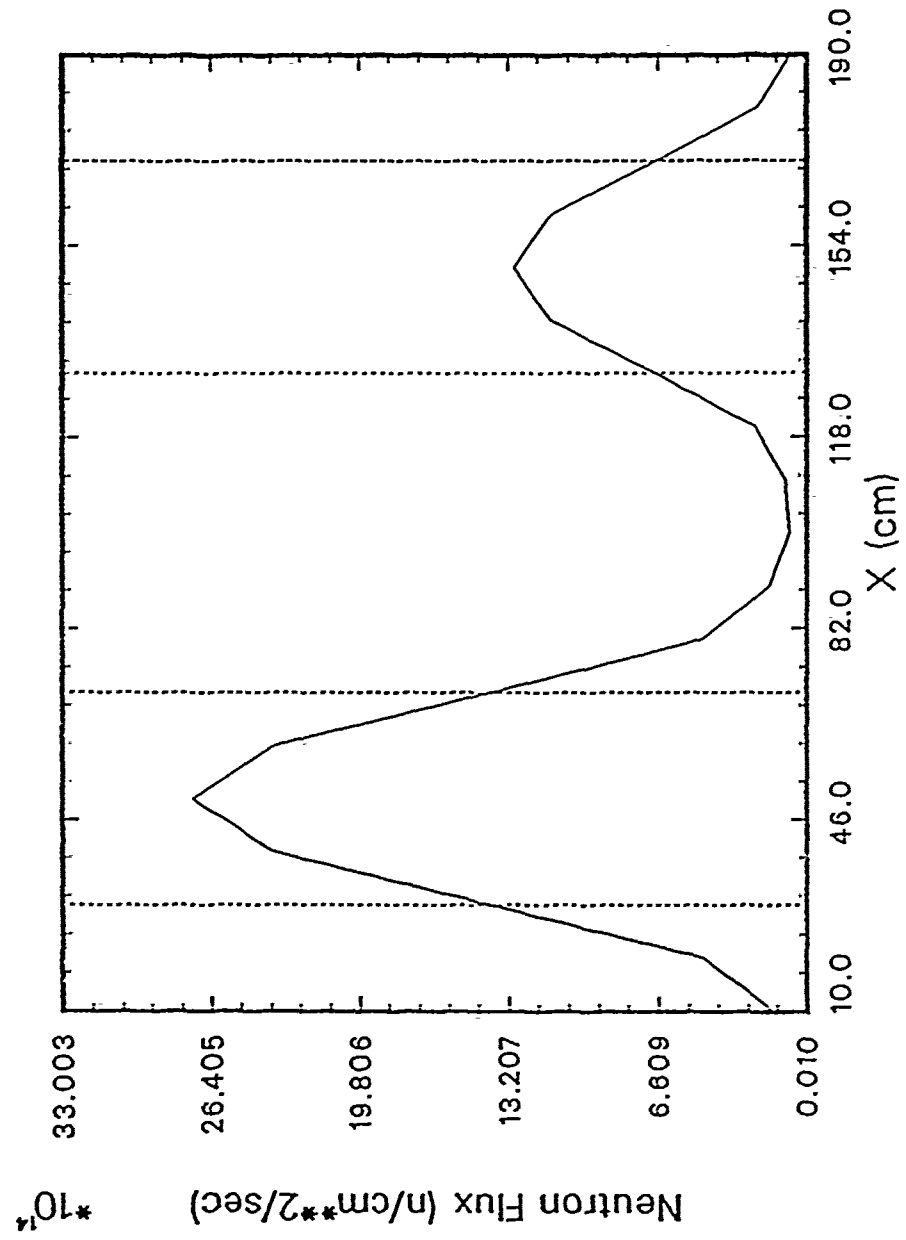


Figure 14: FMP2DT Flux With TWIGL Mesh;  $t = 0.01$  sec

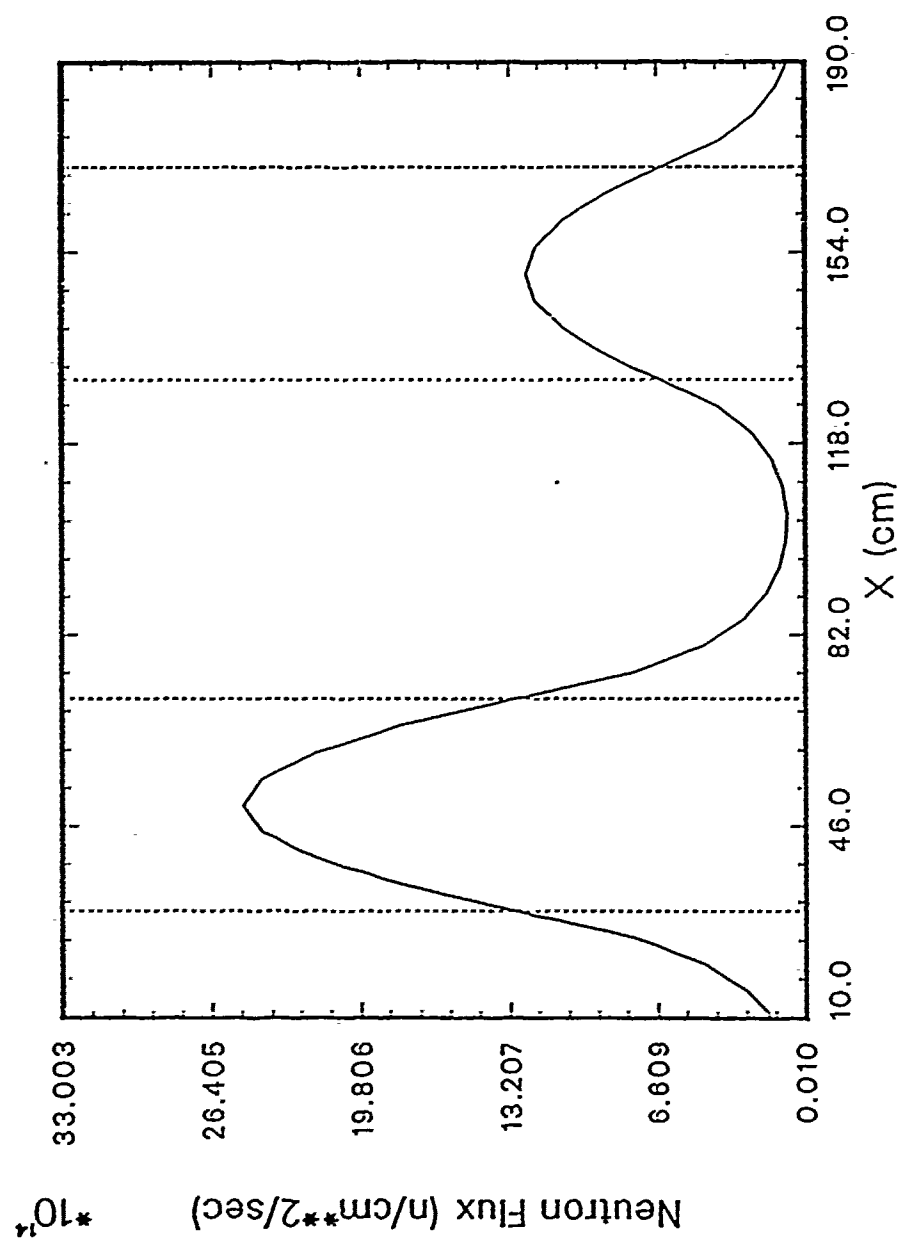


Figure 15: FMP2DT Flux With 2X TWIGL Mesh;  $t = 0.01$  sec

## 7.2 Slab Geometry Benchmark

Since the TWIGL mesh spacing was much larger than a MFP, the most that can be said about that comparison is that FMP2DT produced a similarly shaped flux. The TWIGL work then needs to be supplemented with some exact calculations to establish FMP2DT's ability to produce credible results.

B. D. Ganapol [Ref. 29] published a paper giving exact results for infinite one dimensional slab and cylindrical geometries. FMP2DT modeled these configurations by making the mediums so large that neutrons born because of a pulsed source at time  $t = 0$  sec did not have time to leak out of the medium. Ganapol tabulated these calculations to aid in debugging programming errors. This section compares FMP2DT calculations with Ganapol's exact calculations for XZ slab geometry.

Table 8 shows the exact flux in an infinite slab with an isotropic pulsed plane source at  $x = 0$  in a nonabsorbing medium. For each time step, the flux is calculated at the mean free paths shown. The solutions were generated using Neumann series for the angular and scalar fluxes. The neutron velocity,  $v$ , was set to be 1 cm/sec, and the total cross section,  $\Sigma_t$ , was set at  $1.0 \text{ cm}^{-1}$ . (This was the case for both XZ and RZ geometry.) The media for both of the infinite geometries were non-multiplying. Table 9 shows the FMP2DT results, and Table 10 shows the percent relative error.

The data in Table 9 were calculated with a two dimensional slab configuration with a reflective boundary at  $x = 0$  cm, vacuum boundaries at  $x = 45$  cm and  $z = 0$  and  $z = 46$  cm. These values represent the physical dimensions of the slab modeled. The fluxes were calculated at  $x = 1, 2, 3, 4, 5$ , and 6 cm respectively with a corresponding value of  $z = 23.0$  cm. These values of  $x$  were 1 MFP apart, with the first being 1 MFP from the boundary. For all runs in both slab and cylindrical

geometries, the source had a thickness of  $6.25\text{E-}02$  cm. To insure convergence, ten runs were done with different mesh spacing and different time steps. As the mesh spacing became finer, it became necessary to model the infinite medium by using reflective boundary conditions on the top and bottom of the slab, which left only the right side allowing any leakage. It was found that only five mesh points in the  $z$  direction were necessary. Most runs were modeled with a reflector at  $z = 0$  and  $z = 4$  cm and the flux data calculated at  $z = 2$  cm. In the cases where  $\Delta z = 2$  cm, the reflectors were put at  $z = 0$  and  $z = 8$  cm with the flux calculations made at  $z = 4$  cm. The reflective top and bottom boundary configurations yielded the same answers as did the configuration with vacuum boundary conditions on the top and bottom. Since the reflective configurations had fewer axial mesh points, there was a substantial savings in computational cost, and they had much faster run times. These same schemes were done with the cylindrical calculations. Table 11 summarizes the different configurations.

The results of the FMP2DT flux are extremely good. The error at 1 mean free path (MFP) is most noticeable at early time. It is expected that the flux at 1 MFP would yield the most error since this is closest to the boundary and a  $P_1$  approximation is more likely to be suspect there. Also, while mathematically the line source can be turned on and off at a time  $t = 0$ , at  $x = 0$  cm, using a delta function, the code cannot. The source had to have some finite dimension, and it had to be left on at some finite time. These dimensions were extremely small, but produced some error.

Figure 16 shows that the error dies out as time increases. However, even for earlier times, the flux shape is in good agreement. Figure 17 shows the comparison between the FMP2DT and the exact flux two MFPs from the source. Again, the early time values have the worst error. Figures 18, 19, 20, and 21 show the FMP2DT



and exact flux calculations at 3, 4, 5, and 6 MFPs respectively. The error for these calculations is extremely small, especially after the first few time points. This is consistent with the expected flux behavior using a  $P_1$  approximation.

TIME	1 MFP	2 MFPs	3 MFPs	4 MFPs	5 MFPs	6 MFPs
0	0.0000E+00	0.0000E+00	0.0000E+00	0.0000E+00	0.0000E+00	0.0000E+00
1	1.8394E-01	0.0000E+00	0.0000E+00	0.0000E+00	0.0000E+00	0.0000E+00
3	2.3942E-01	9.3836E-02	8.2978E-03	0.0000E+00	0.0000E+00	0.0000E+00
5	1.9957E-01	1.2105E-01	4.9595E-02	1.1823E-02	6.7379E-04	0.0000E+00
7	1.7347E-01	1.2293E-01	6.8028E-02	2.8447E-02	8.4158E-03	1.5036E-03
9	1.5528E-01	1.1935E-01	7.6384E-02	4.0186E-02	1.7004E-02	5.5765E-03
11	1.4175E-01	1.1454E-01	7.9986E-02	4.7953E-02	2.4433E-02	1.0419E-02
13	1.3120E-01	1.0969E-01	8.1200E-02	5.3024E-02	3.0372E-02	1.5137E-02
15	1.2269E-01	1.0514E-01	8.1158E-02	5.6305E-02	3.4985E-02	1.9376E-02
17	1.1564E-01	1.0096E-01	8.0438E-02	5.8390E-02	3.8531E-02	2.3041E-02
19	1.0968E-01	9.7166E-02	7.9349E-02	5.9663E-02	4.1241E-02	2.6150E-02
21	1.0455E-01	9.3719E-02	7.8066E-02	6.0377E-02	4.3305E-02	2.8761E-02
23	1.0007E-01	9.0583E-02	7.6693E-02	6.0698E-02	4.4868E-02	3.0942E-02
25	9.6128E-02	8.7720E-02	7.5287E-02	6.0744E-02	4.6042E-02	3.2757E-02
27	9.2615E-02	8.5099E-02	7.3885E-02	6.0592E-02	4.6912E-02	3.4265E-02
29	8.9460E-02	8.2688E-02	7.2508E-02	6.0301E-02	4.7547E-02	3.5515E-02
31	8.6606E-02	8.0464E-02	7.1168E-02	5.9910E-02	4.7984E-02	3.6549E-02
33	8.4009E-02	7.8404E-02	6.9872E-02	5.9448E-02	4.8274E-02	3.7400E-02
35	8.1632E-02	7.6491E-02	6.8624E-02	5.8937E-02	4.8445E-02	3.8099E-02
37	7.9446E-02	7.4708E-02	6.7424E-02	5.8393E-02	4.8519E-02	3.8669E-02
39	7.7427E-02	7.3041E-02	6.6272E-02	5.7826E-02	4.8515E-02	3.9129E-02
41	7.5553E-02	7.1479E-02	6.5167E-02	5.7247E-02	4.8450E-02	3.9497E-02
43	7.3810E-02	7.0012E-02	6.4108E-02	5.6661E-02	4.8334E-02	3.9786E-02
45	7.2182E-02	6.8630E-02	6.3091E-02	5.6074E-02	4.8177E-02	4.0007E-02

Table 8: Exact Flux Due to an Isotropic Pulsed Plane Source at  $x = 0$  in a Nonabsorbing Infinite Medium For Slab Geometry

TIME	1 MFP	2 MFPs	3 MFPs	4 MFPs	5 MFPs	6 MFPs
0	0.0000E+00	0.0000E+00	0.0000E+00	0.0000E+00	0.0000E+00	0.0000E+00
1	1.0461E-01	0.0000E+00	0.0000E+00	0.0000E+00	0.0000E+00	0.0000E+00
3	2.7485E-01	7.4742E-02	9.8860E-03	0.0000E+00	0.0000E+00	0.0000E+00
5	2.0536E-01	1.3069E-01	4.3453E-02	9.2030E-03	1.4897E-03	0.0000E+00
7	1.6964E-01	1.3084E-01	7.0663E-02	2.5537E-02	6.6768E-03	1.3782E-03
9	1.5137E-01	1.2190E-01	8.0677E-02	4.0570E-02	1.5307E-02	4.4989E-03
11	1.3853E-01	1.1488E-01	8.2818E-02	4.9817E-02	2.4089E-02	9.3242E-03
13	1.2850E-01	1.0927E-01	8.2747E-02	5.4848E-02	3.0971E-02	1.4612E-02
15	1.2038E-01	1.0442E-01	8.1953E-02	5.7699E-02	3.5895E-02	1.9389E-02
17	1.1362E-01	1.0012E-01	8.0792E-02	5.9390E-02	3.9427E-02	2.3361E-02
19	1.0789E-01	9.6275E-02	7.9427E-02	6.0360E-02	4.2021E-02	2.6594E-02
21	1.0294E-01	9.2818E-02	7.7963E-02	6.0845E-02	4.3951E-02	2.9232E-02
23	9.8615E-02	8.9692E-02	7.6467E-02	6.0993E-02	4.5387E-02	3.1392E-02
25	9.4792E-02	8.6850E-02	7.4978E-02	6.0904E-02	4.6448E-02	3.3166E-02
27	9.1382E-02	8.4254E-02	7.3519E-02	6.0649E-02	4.7220E-02	3.4624E-02
29	8.8315E-02	8.1871E-02	7.2104E-02	6.0276E-02	4.7766E-02	3.5822E-02
31	8.5538E-02	7.9674E-02	7.0738E-02	5.9821E-02	4.8136E-02	3.6805E-02
33	8.3006E-02	7.7642E-02	6.9425E-02	5.9309E-02	4.8366E-02	3.7609E-02
35	8.0687E-02	7.5755E-02	6.8166E-02	5.8758E-02	4.8485E-02	3.8263E-02
37	7.8552E-02	7.3997E-02	6.6960E-02	5.8182E-02	4.8515E-02	3.8792E-02
39	7.6578E-02	7.2355E-02	6.5805E-02	5.7590E-02	4.8475E-02	3.9216E-02
41	7.4745E-02	7.0815E-02	6.4700E-02	5.6991E-02	4.8377E-02	3.9552E-02
43	7.3038E-02	6.9369E-02	6.3642E-02	5.6389E-02	4.8234E-02	3.9811E-02
45	7.1442E-02	6.8007E-02	6.2629E-02	5.5789E-02	4.8054E-02	4.0007E-02

Table 9: FMP2DT Flux Due to an Isotropic Pulsed Plane Source at  $x = 0$  in a Nonabsorbing Medium For Slab Geometry

TIME	1 MFP	2 MFPs	3 MFPs	4 MFPs	5 MFPs	6 MFPs
1	43.13	N/A	N/A	N/A	N/A	N/A
3	14.80	20.35	19.14	N/A	N/A	N/A
5	2.90	7.96	12.38	22.16	121.09	N/A
7	2.21	6.43	3.87	10.23	20.66	8.34
9	2.52	2.14	5.62	0.96	9.98	19.32
11	2.27	0.30	3.54	3.89	1.41	10.51
13	2.06	0.38	1.91	3.44	1.97	3.47
15	1.88	0.68	0.98	2.94	2.60	0.07
17	1.75	0.83	0.44	1.71	2.33	1.39
19	1.63	0.92	0.10	1.22	1.89	1.70
21	1.54	0.96	0.13	0.78	1.49	1.64
23	1.45	0.98	0.29	0.49	1.16	1.45
25	1.39	0.99	0.41	0.26	0.88	1.25
27	1.33	0.99	0.50	0.09	0.66	1.05
29	1.28	0.99	0.56	0.04	0.47	0.86
31	1.23	0.98	0.60	0.15	0.32	0.70
33	1.19	0.97	0.64	0.23	0.19	0.56
35	1.16	0.96	0.67	0.30	0.08	0.43
37	1.13	0.95	0.69	0.36	0.01	0.32
39	1.10	0.94	0.70	0.41	0.08	0.22
41	1.07	0.93	0.72	0.45	0.15	0.14
43	1.05	0.92	0.73	0.48	0.21	0.06
45	1.03	0.91	0.73	0.51	0.26	0.00

Table 10: The Percent Relative Error for the FMP2DT Slab Calculations

run	reflectors	$\Delta x$ or $\Delta r$ , $\Delta z$	$\Delta t$
1	no	1.0 cm	1.0 sec
2	yes	0.5 cm	1.0 sec
3	yes	0.5 cm	0.5 sec
4	yes	0.5 cm	0.25 sec
5	yes	1.0 cm	2.0 sec
6	yes	1.0 cm	1.0 sec
7	yes	1.0 cm	0.5 sec
8	yes	2.0 cm	4.0 sec
9	yes	2.0 cm	2.0 sec
10	yes	2.0 cm	1.0 sec

Table 11: Run Summary for the Infinite Slab and Cylindrical Geometries

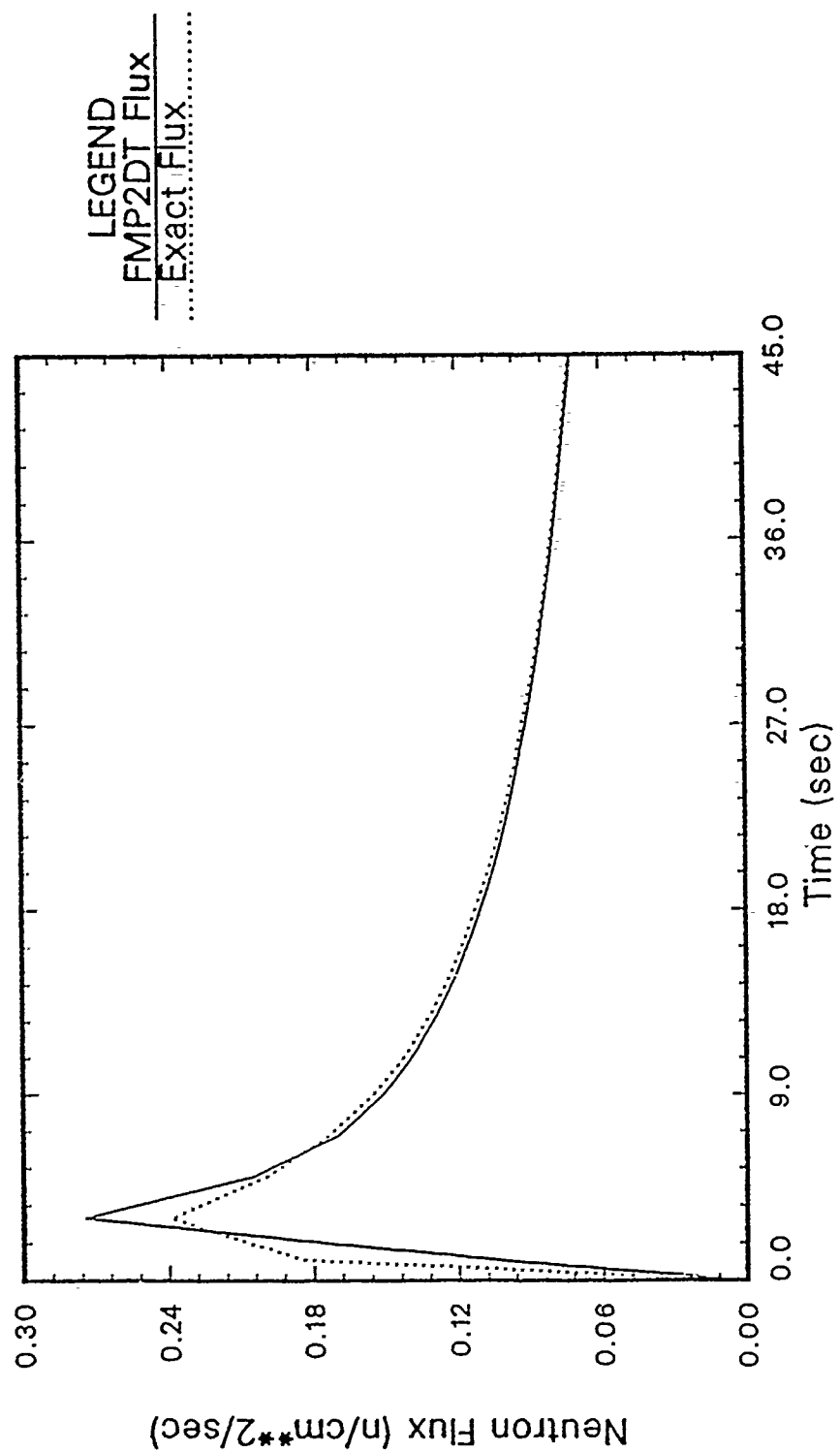


Figure 16: FMP2DT and Exact Flux, XZ Geometry 1 MFP From Boundary

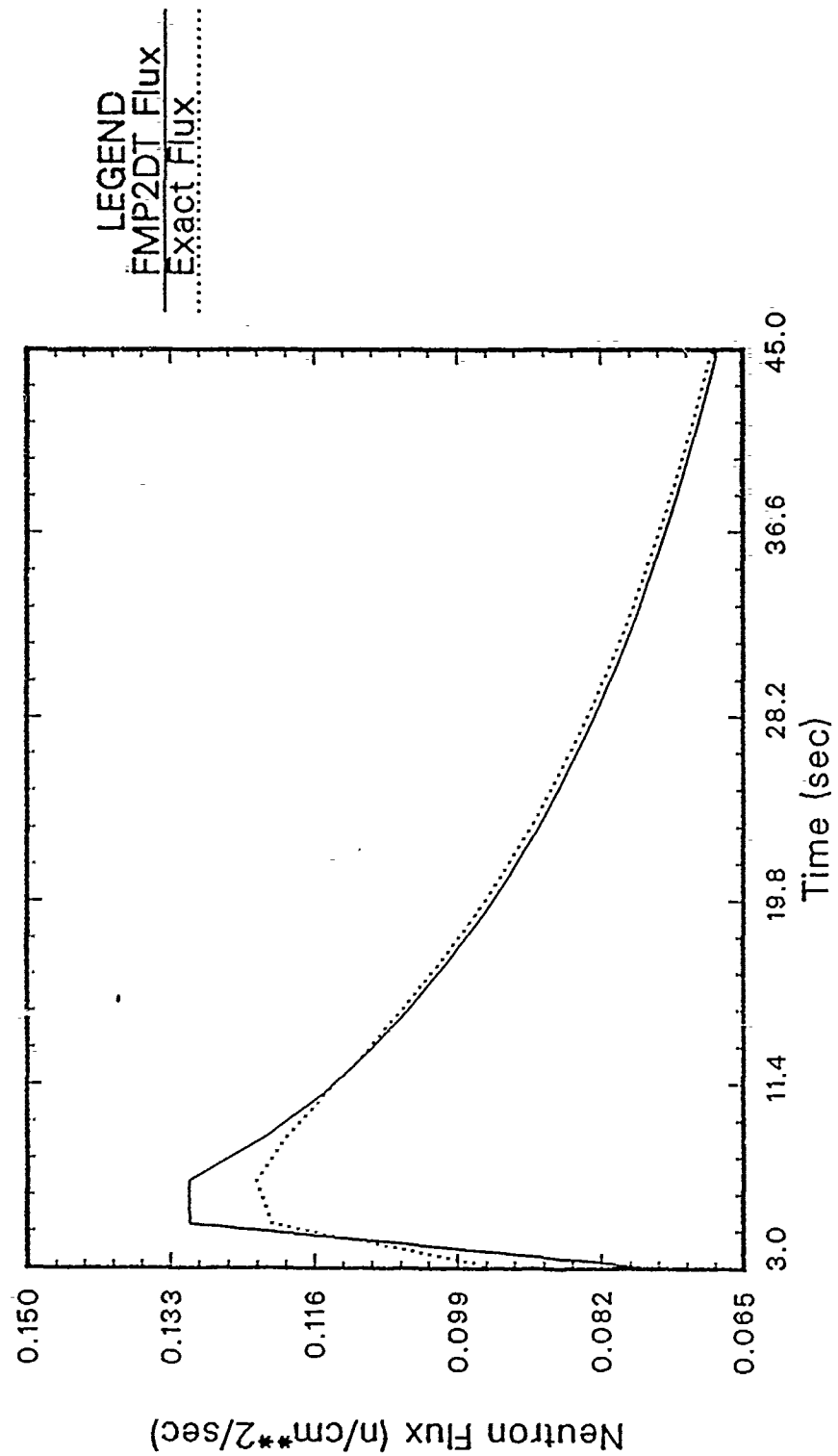


Figure 17: FMP2DT and Exact Flux, XZ Geometry 2 MFPs From Boundary

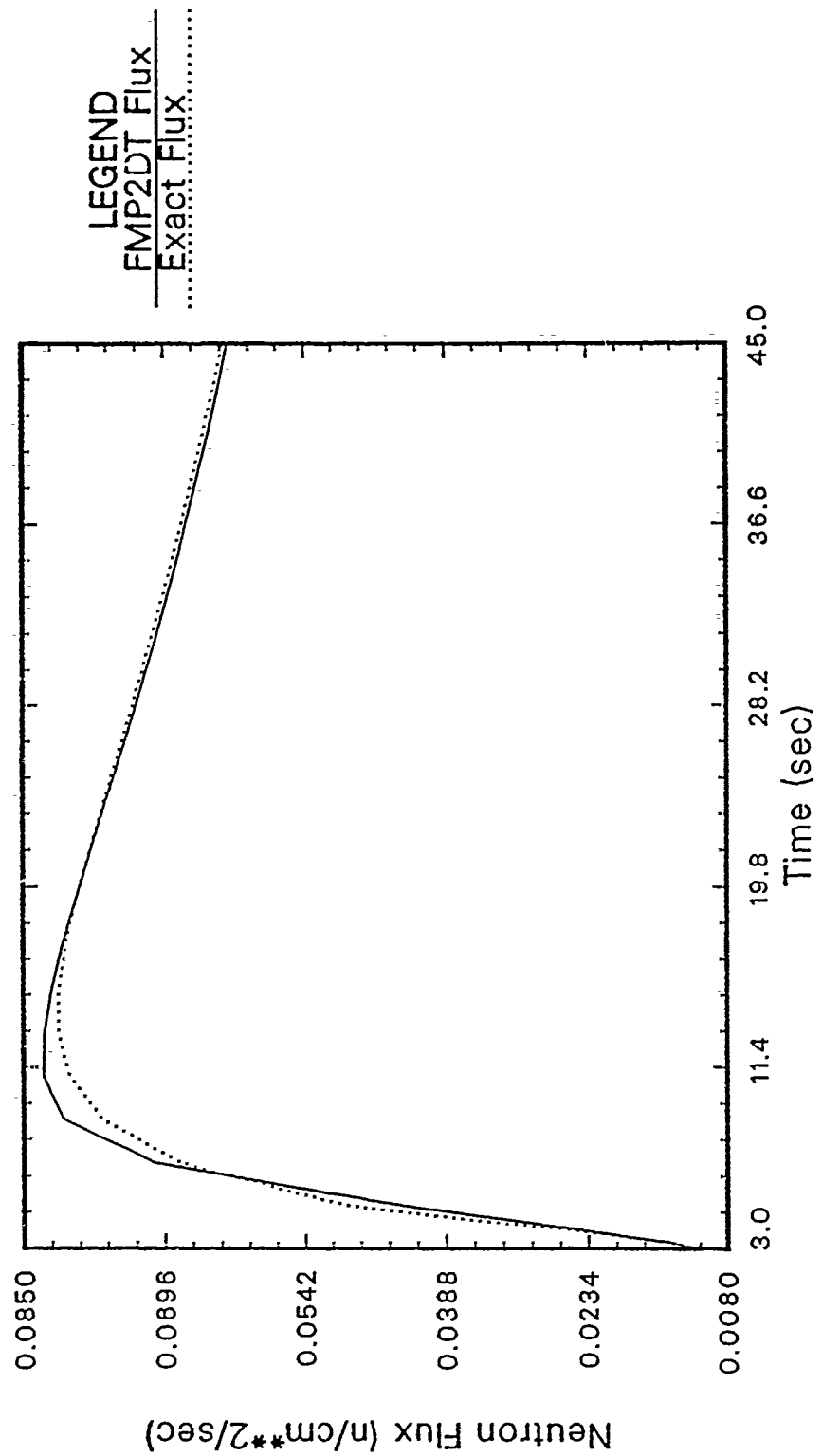


Figure 18: FMP2DT and Exact Flux, XZ Geometry 3 MFPs From Boundary

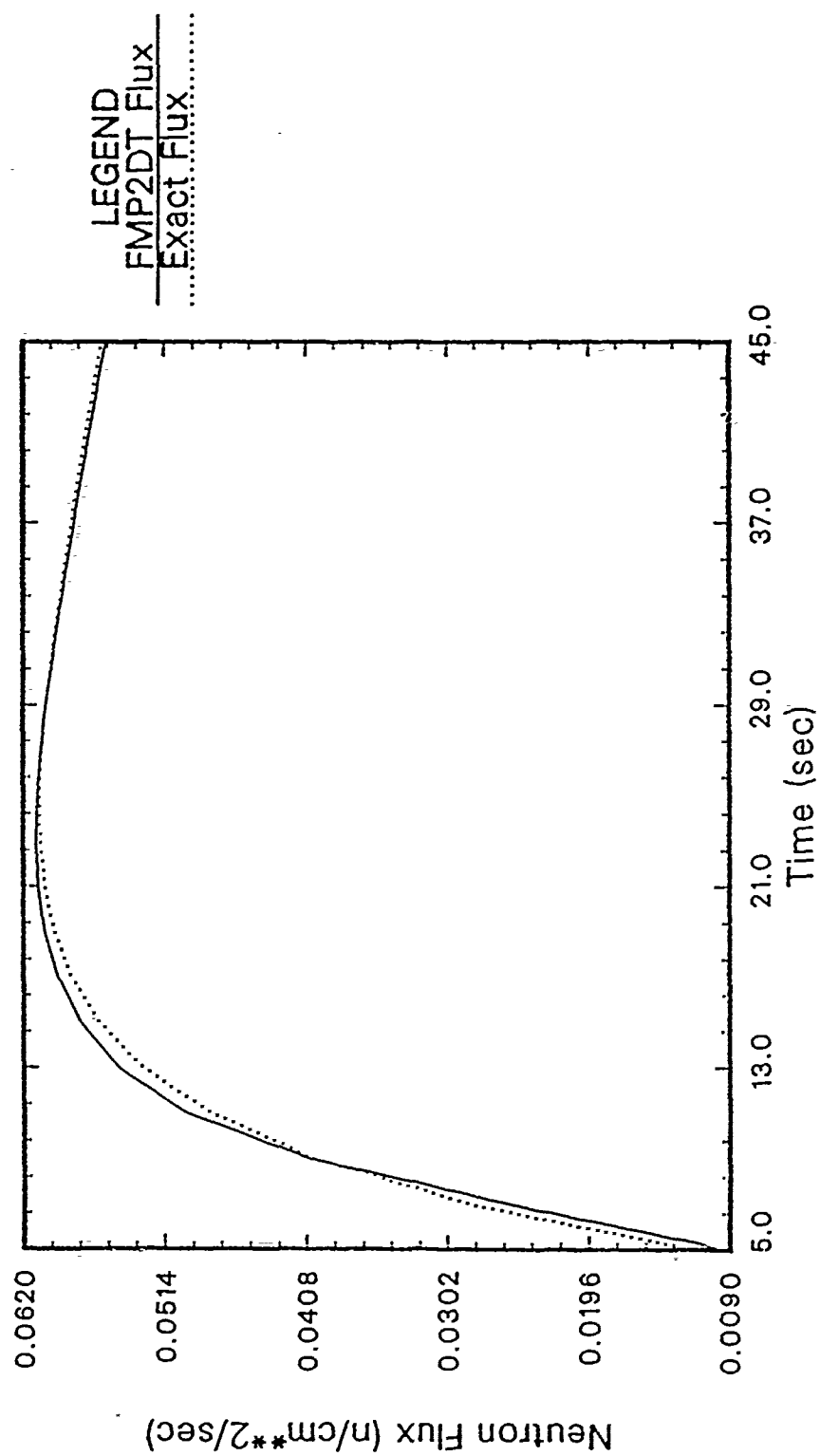


Figure 19: FMP2DT and Exact Flux, XZ Geometry 4 MFPs From Boundary

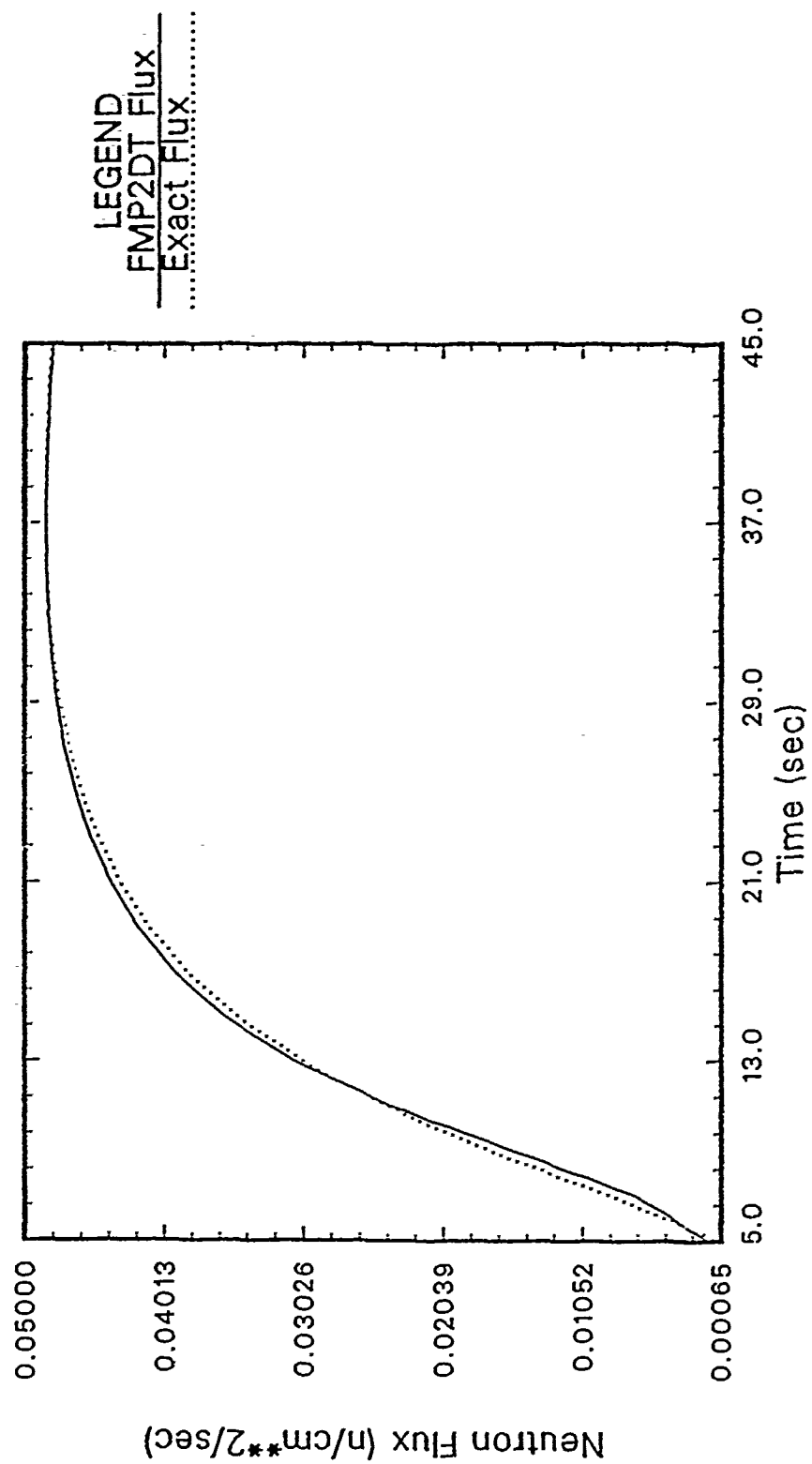


Figure 20: FMP2DT and Exact Flux, XZ Geometry 5 MFPs From Boundary



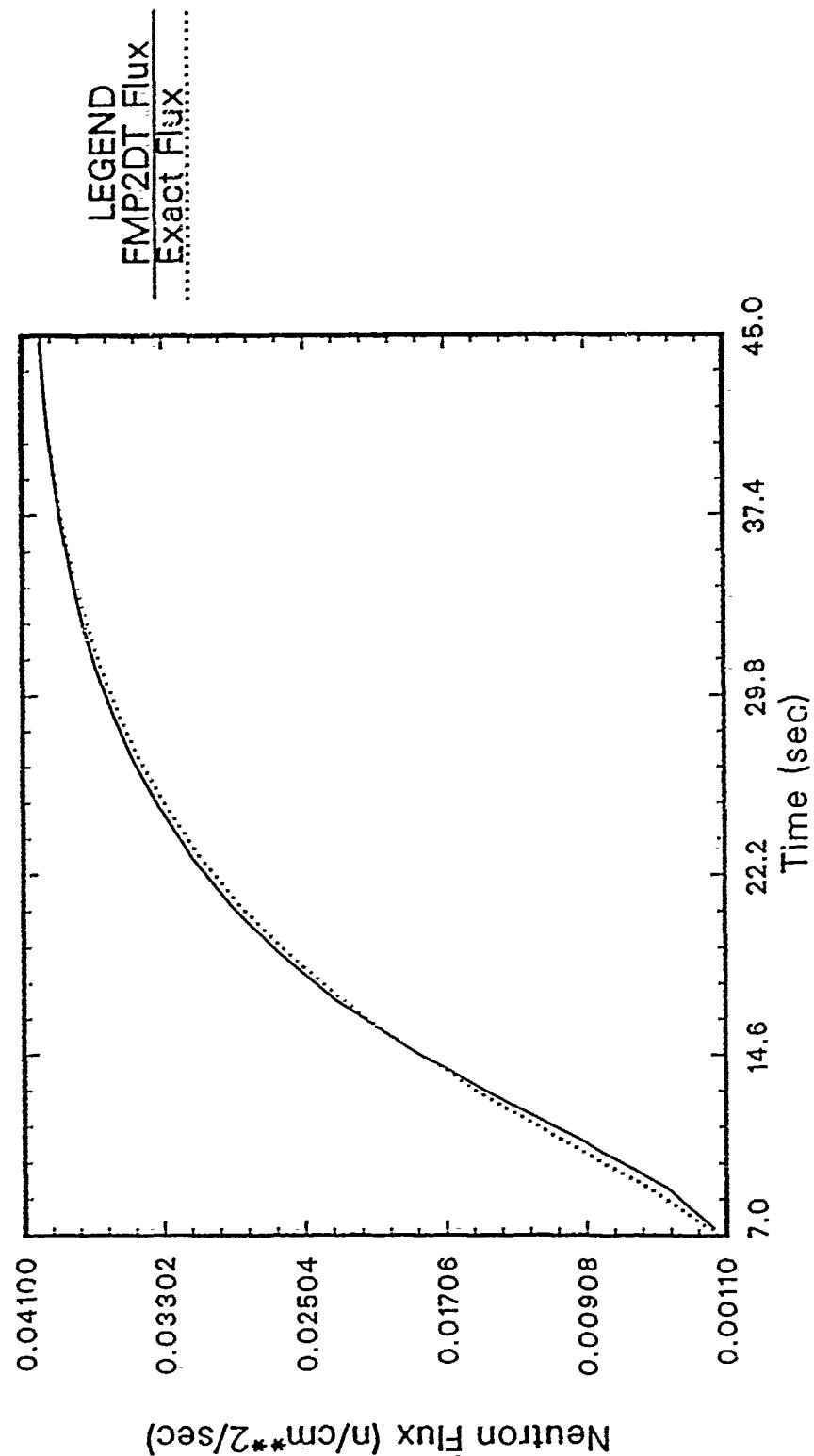


Figure 21: FMP2DT and Exact Flux, XZ Geometry 6 MFPs From Boundary

### 7.3 Infinite Cylindrical Geometry Benchmark

The Ganapol paper already cited also gave results for cylindrical geometry. Table 12 shows the exact flux due to an isotropic pulsed line source at  $r = 0$  cm in a nonabsorbing infinite medium.

As with XZ geometry, several different runs were made to insure convergence. The run summary is given in Table 11. For RZ geometry, there is a reflective boundary at the radial center, i.e. at  $r = 0$  cm. The rest of the boundary conditions for the different configurations are as described for the XZ calculations.

Again, just like the XZ case, FMP2DT calculated the flux with good agreement with the exact flux. Table 12 shows the exact flux, Table 13 shows the FMP2DT calculations, and Table 14 shows the percent relative error with respect to the exact flux. As with the XZ geometry, the line source had a small finite thickness, and the source was turned on and off with some small finite time. This introduces some error automatically that cannot be omitted.

Figures 22, 23, 24, 25, 26, and 27 show the graphs comparing the exact and FMP2DT fluxes at 1 MFP, 2 MFPs, 3 MFPs, 4 MFPs, 5 MFPs, and 6 MFPs respectively. As in the XZ geometry calculations, the worst error occurred at the earlier times. This is caused by the characteristic of the  $P_1$  approximation and the finite source configuration already stated. As the calculations moved away from the cylinder's center line, the FMP2DT flux was nearly identical to the exact flux reported by Ganapol.

TIME	1 MFP	2 MFPs	3 MFPs	4 MFPs	5 MFPs	6 MFPs
1	0.0000E+00	0.0000E+00	0.0000E+00	0.0000E+00	0.0000E+00	0.0000E+00
3	7.3987E-02	3.1734E-02	0.0000E+00	0.0000E+00	0.0000E+00	0.0000E+00
5	4.5977E-02	2.8563E-02	1.2285E-02	3.2456E-03	0.0000E+00	0.0000E+00
7	3.3254E-02	2.3830E-02	1.3458E-02	5.8172E-03	1.8173E-03	3.6050E-04
9	2.6027E-02	2.0134E-02	1.3033E-02	6.9753E-03	3.0260E-03	1.0291E-03
11	2.1376E-02	1.7346E-02	1.2201E-02	7.3928E-03	3.8227E-03	1.6628E-03
13	1.8133E-02	1.5205E-02	1.1312E-02	7.4409E-03	4.3012E-03	2.1729E-03
15	1.5744E-02	1.3521E-02	1.0476E-02	7.3063E-03	4.5721E-03	2.5552E-03
17	1.3911E-02	1.2165E-02	9.7197E-03	7.0842E-03	4.6998E-03	2.8295E-03
19	1.2460E-02	1.1053E-02	9.0465E-03	6.8239E-03	4.7367E-03	3.0193E-03
21	1.1282E-02	1.0125E-02	8.4492E-03	6.5515E-03	4.7150E-03	3.1447E-03
23	1.0308E-02	9.3393E-03	7.9191E-03	6.2809E-03	4.6558E-03	3.2218E-03
25	9.4893E-03	8.6659E-03	7.4470E-03	6.0192E-03	4.5731E-03	3.2630E-03
27	8.7907E-03	8.0825E-03	7.0250E-03	5.7700E-03	4.4761E-03	3.2775E-03
29	8.1878E-03	7.5723E-03	6.6462E-03	5.5346E-03	4.3711E-03	3.2722E-03
31	7.6623E-03	7.1224E-03	6.3047E-03	5.3135E-03	4.2620E-03	3.2523E-03
33	7.2002E-03	6.7228E-03	5.9955E-03	5.1062E-03	4.1518E-03	3.2218E-03
35	6.7907E-03	6.3654E-03	5.7144E-03	4.9122E-03	4.0423E-03	3.1836E-03
37	6.4252E-03	6.0441E-03	5.4579E-03	4.7306E-03	3.9347E-03	3.1399E-03
39	6.0971E-03	5.7535E-03	5.2229E-03	4.5606E-03	3.8298E-03	3.0924E-03
41	5.8008E-03	5.4895E-03	5.0071E-03	4.4014E-03	3.7281E-03	3.0423E-03
43	5.5320E-03	5.2487E-03	4.8080E-03	4.2520E-03	3.6299E-03	2.9907E-03
45	5.2870E-03	5.0280E-03	4.6240E-03	4.1119E-03	3.5352E-03	2.9382E-03

Table 12: Exact Flux Due to an Isotropic Pulsed Plane Source at  $r = 0$  in a Nonabsorbing Infinite Medium For RZ Geometry

TIME	1 MFP	2 MFPs	3 MFPs	4 MFPs	5 MFPs	6 MFPs
1	0.0000E+00	0.0000E+00	0.0000E+00	0.0000E+00	0.0000E+00	0.0000E+00
3	9.7929E-02	2.7334E-02	0.0000E+00	0.0000E+00	0.0000E+00	0.0000E+00
5	4.1467E-02	3.3692E-02	1.1495E-02	2.3169E-03	0.0000E+00	0.0000E+00
7	2.8879E-02	2.5258E-02	1.4980E-02	5.5035E-03	1.4101E-03	2.8067E-04
9	2.3720E-02	1.9766E-02	1.4075E-02	7.4456E-03	2.8511E-03	8.3037E-04
11	1.9968E-02	1.6787E-02	1.2558E-02	7.9142E-03	3.9532E-03	1.5492E-03
13	1.7160E-02	1.4727E-02	1.1371E-02	7.7737E-03	4.5339E-03	2.1888E-03
15	1.5027E-02	1.3124E-02	1.0431E-02	7.4895E-03	4.7768E-03	2.6427E-03
17	1.3360E-02	1.1832E-02	9.6363E-03	7.1807E-03	4.8536E-03	2.9345E-03
19	1.2023E-02	1.0770E-02	8.9485E-03	6.8702E-03	4.8472E-03	3.1170E-03
21	1.0928E-02	9.8828E-03	8.3475E-03	6.5671E-03	4.7933E-03	3.2283E-03
23	1.0015E-02	9.1301E-03	7.8188E-03	6.2770E-03	4.7102E-03	3.2910E-03
25	9.2419E-03	8.4836E-03	7.3509E-03	6.0029E-03	4.6097E-03	3.3192E-03
27	8.5794E-03	7.9223E-03	6.9342E-03	5.7457E-03	4.4994E-03	3.3224E-03
29	8.0052E-03	7.4305E-03	6.5610E-03	5.5055E-03	4.3813E-03	3.3077E-03
31	7.5029E-03	6.9961E-03	6.2251E-03	5.2815E-03	4.2677E-03	3.2799E-03
33	7.0598E-03	6.6095E-03	5.9213E-03	5.0727E-03	4.1519E-03	3.2429E-03
35	6.6661E-03	6.2634E-03	5.6452E-03	4.8780E-03	4.0381E-03	3.1993E-03
37	6.3138E-03	5.9516E-03	5.3934E-03	4.6965E-03	3.9272E-03	3.1511E-03
39	5.9969E-03	5.6694E-03	5.1628E-03	4.5269E-03	3.8199E-03	3.0999E-03
41	5.7162E-03	5.4126E-03	4.9508E-03	4.3684E-03	3.7164E-03	3.0468E-03
43	5.4496E-03	5.1780E-03	4.7554E-03	4.2199E-03	3.6169E-03	2.9927E-03
45	5.2118E-03	4.9629E-03	4.5747E-03	4.0807E-03	3.5213E-03	2.9382E-03

Table 13: FMP2DT Flux Due to an Isotropic Pulsed Plane Source at  $r = 0$  in a Nonabsorbing Infinite Medium For RZ Geometry

TIME	1 MFP	2 MFPs	3 MFPs	4 MFPs	5 MFPs	6 MFPs
3	32.36	13.87	N/A	N/A	N/A	N/A
5	9.81	18.66	6.43	28.61	N/A	N/A
7	13.16	5.99	11.31	5.29	22.41	22.14
9	8.86	1.83	7.76	6.74	5.78	19.31
11	6.59	3.22	2.93	7.05	3.41	6.83
13	5.37	3.14	0.52	4.47	5.34	0.73
15	4.55	2.94	0.43	2.51	4.48	3.42
17	3.96	2.74	0.86	1.36	3.27	3.71
19	3.51	2.56	1.08	0.68	2.33	3.24
21	3.14	2.39	1.20	0.24	1.66	2.66
23	2.84	2.24	1.27	0.06	1.17	2.15
25	2.61	2.10	1.29	0.27	0.80	1.72
27	2.40	1.98	1.29	0.42	0.52	1.37
29	2.23	1.87	1.28	0.53	0.30	1.08
31	2.08	1.77	1.26	0.60	0.13	0.85
33	1.95	1.69	1.24	0.66	~0.0	0.65
35	1.83	1.60	1.21	0.70	0.10	0.49
37	1.73	1.53	1.18	0.72	0.19	0.36
39	1.64	1.46	1.15	0.74	0.26	0.24
41	1.56	1.40	1.12	0.75	0.31	0.15
43	1.49	1.35	1.09	0.75	0.36	0.07
45	1.42	1.29	1.07	0.76	0.39	0.00

Table 14: The Percent Relative Error for the FMP2DT Cylindrical Calculations

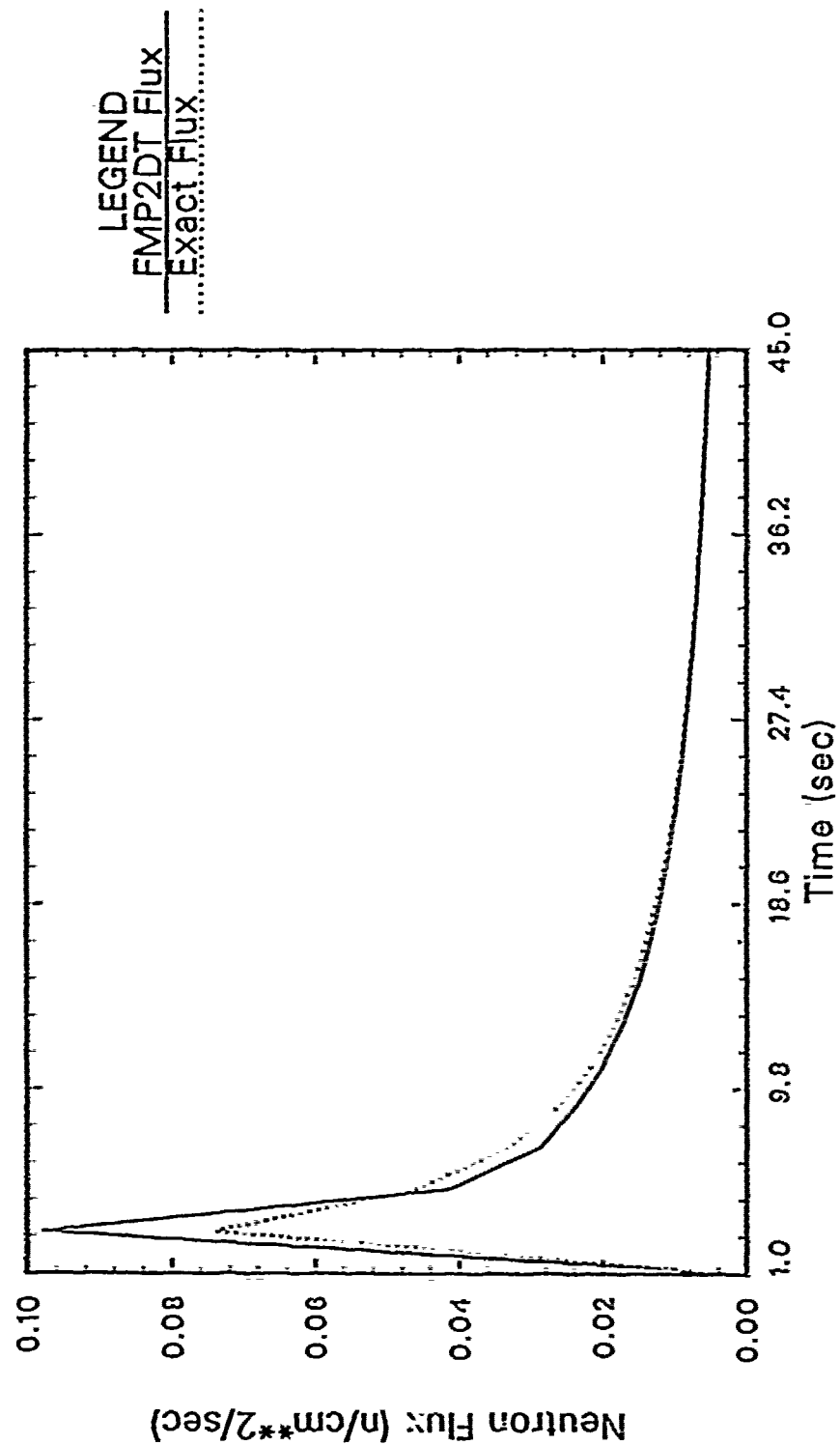


Figure 22: FMP2DT and Exact Flux, RZ Geometry 1 MFP From Boundary

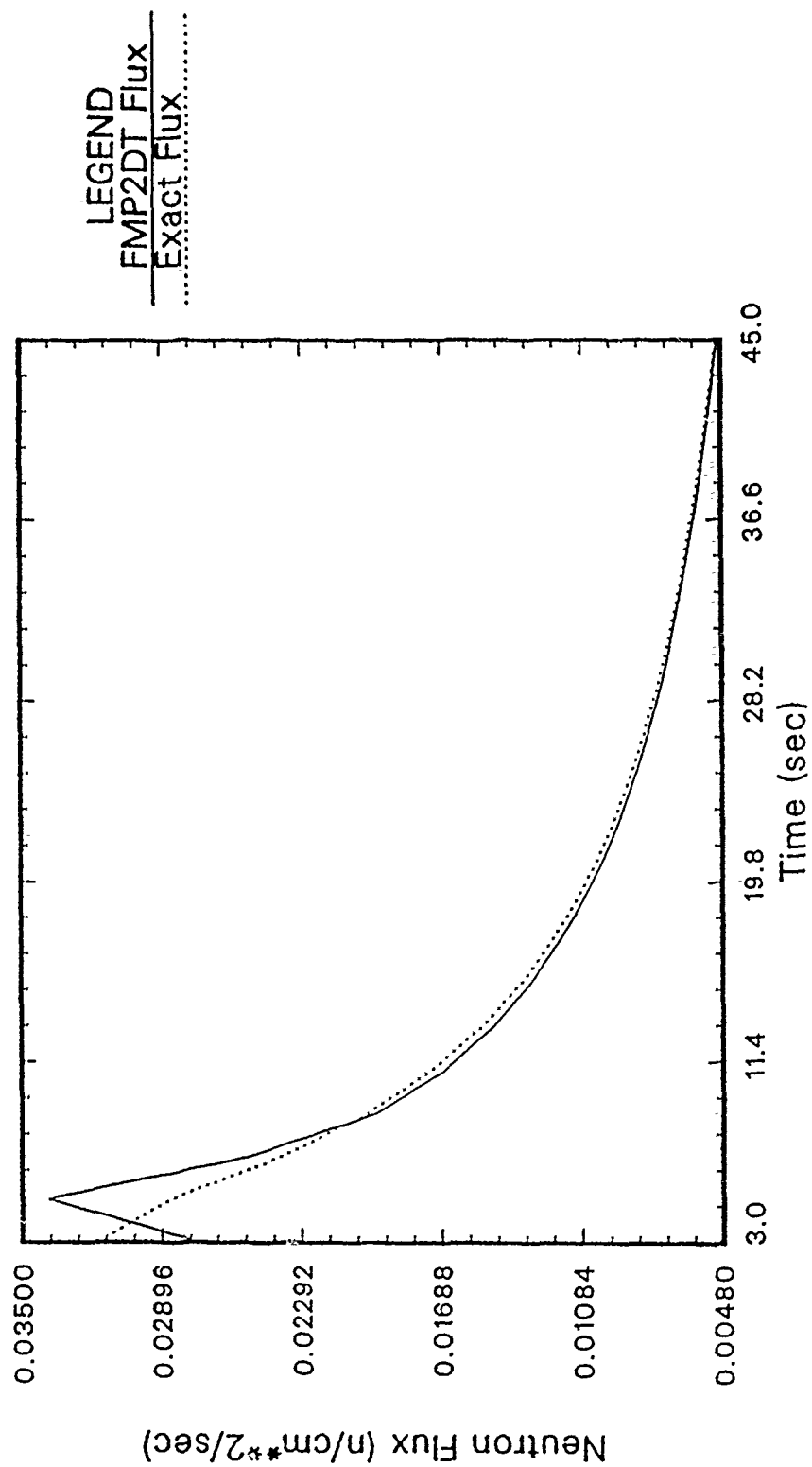


Figure 23: FMP2DT and Exact Flux, RZ Geometry 2 MFPs From Boundary

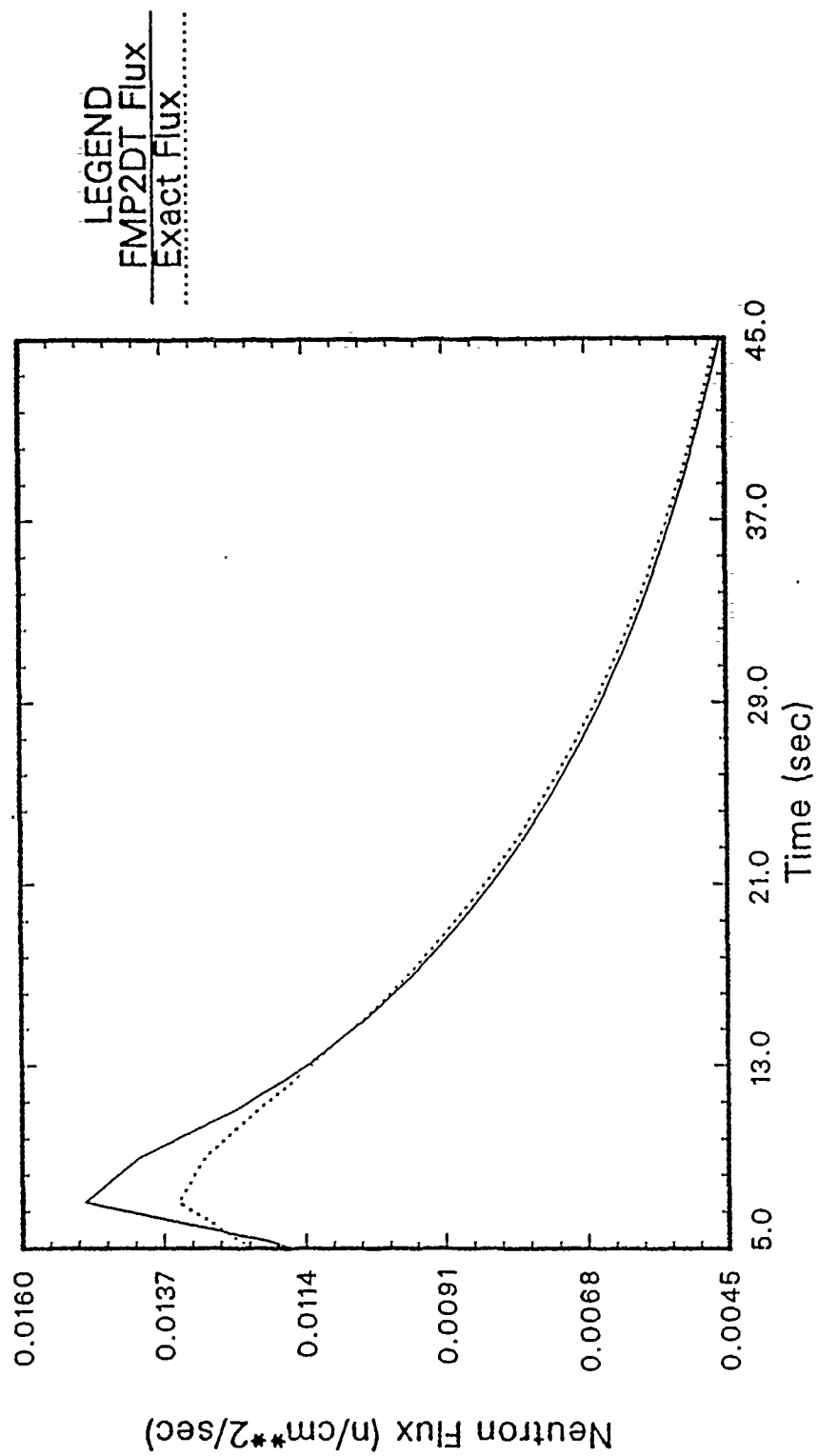


Figure 24: FMP2DT and Exact Flux, RZ Geometry 3 MFPs From Boundary

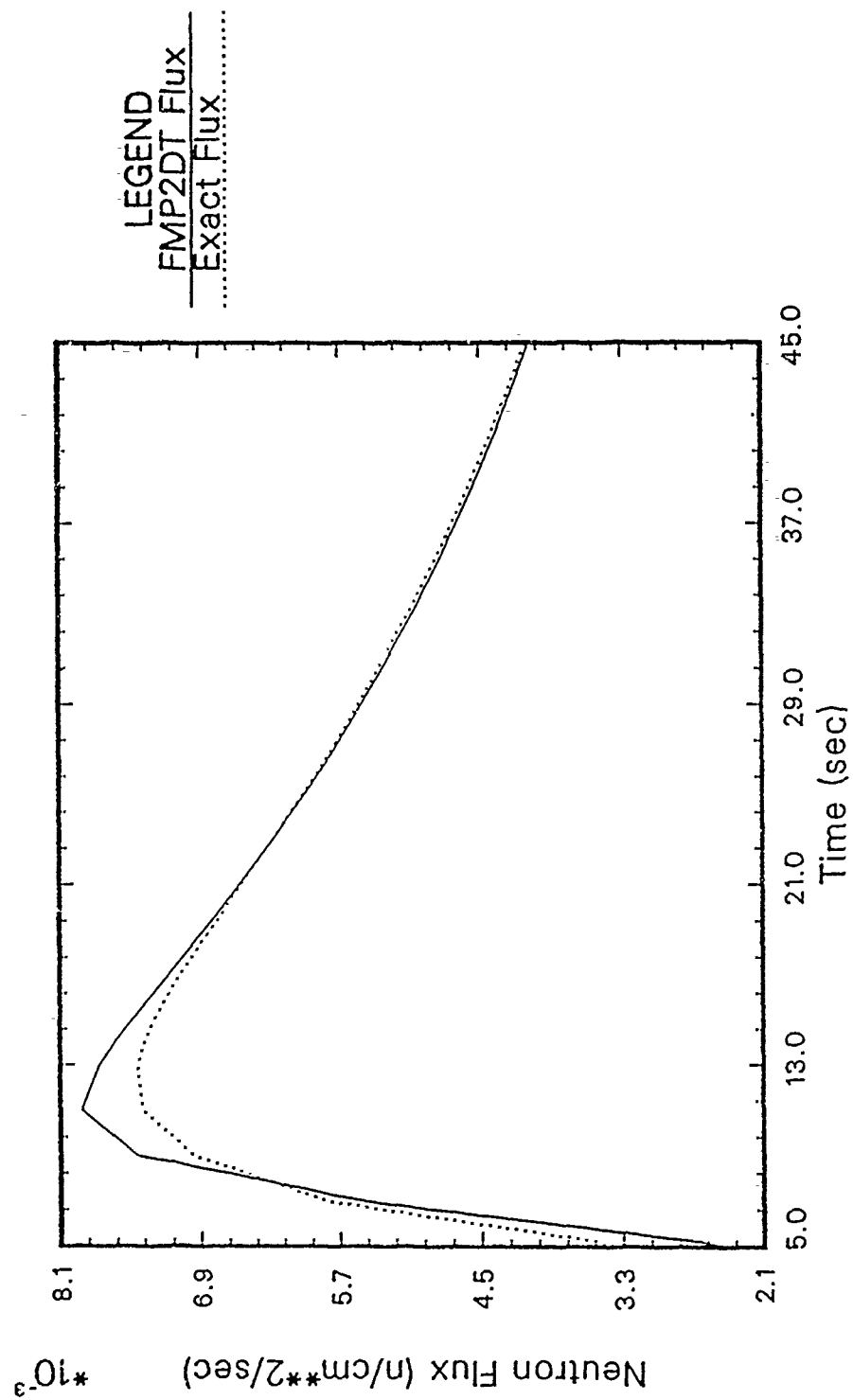


Figure 25: FMP2DT and Exact Flux, RZ Geometry 4 MFPs From Boundary



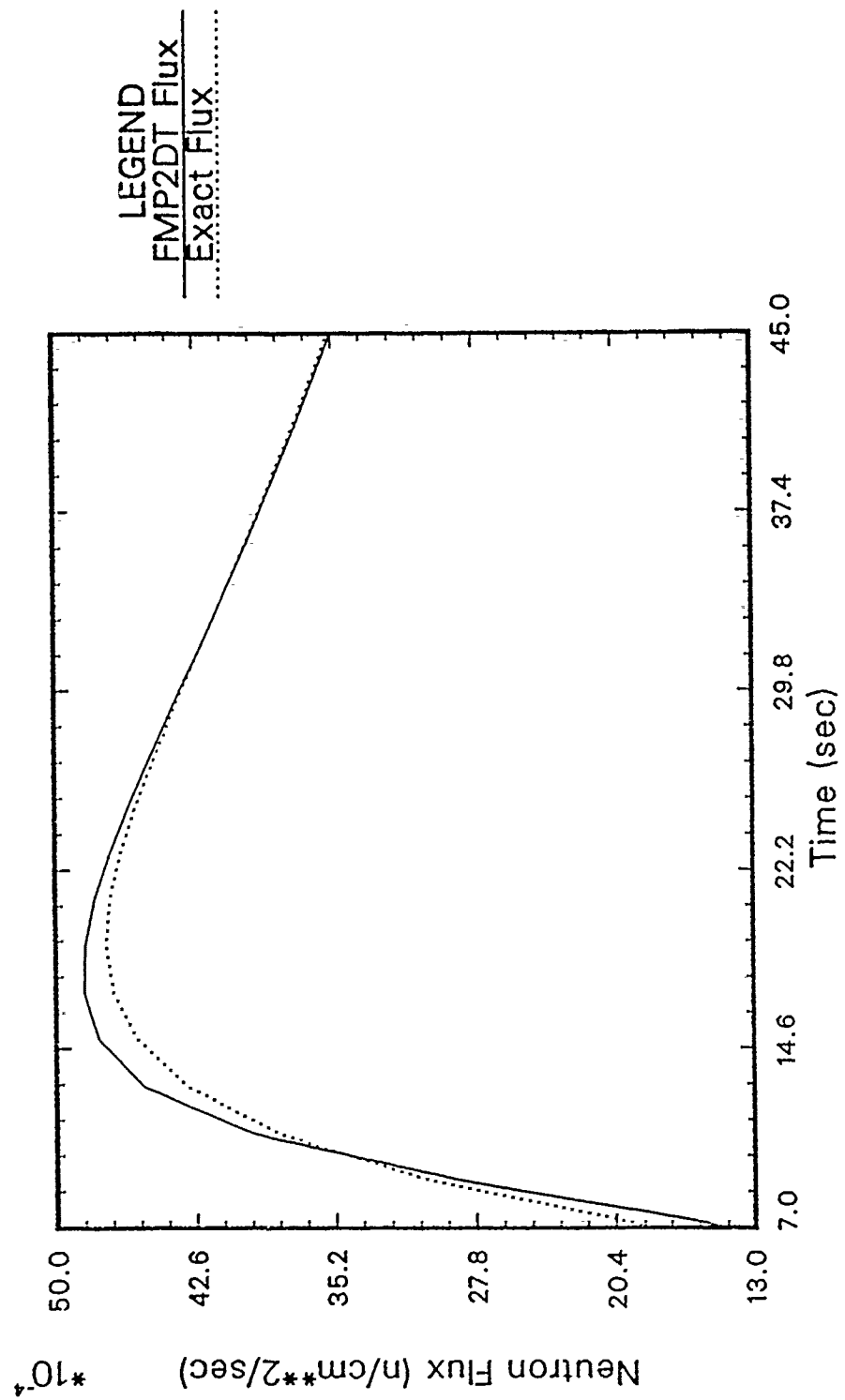


Figure 26: FMP2DT and Exact Flux, RZ Geometry 5 MFPs From Boundary

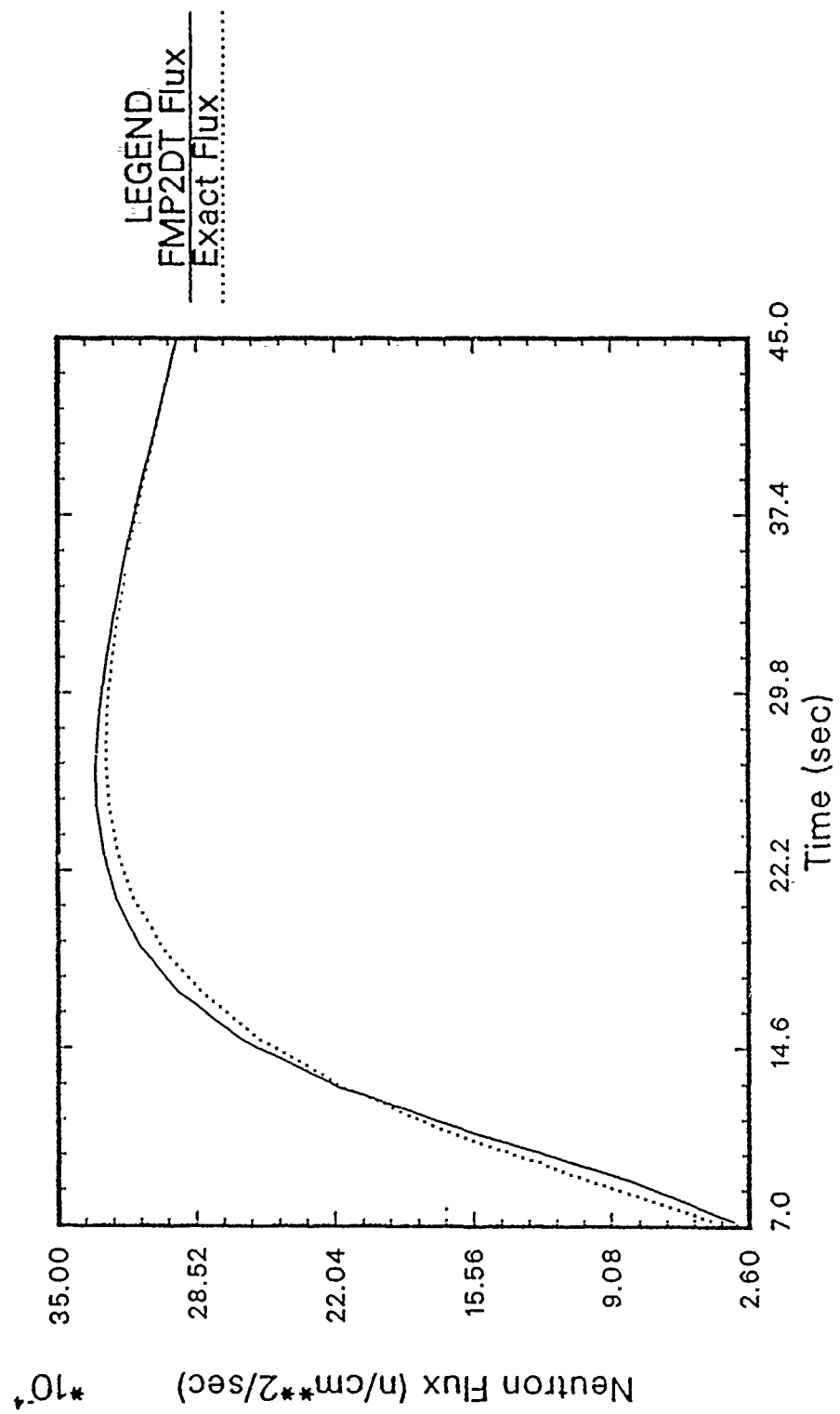


Figure 27: FMP2DT and Exact Flux, RZ Geometry 6 MFPs From Boundary

## 7.4 Benchmark Conclusions

FMP2DT could not be benchmarked with TWIGL. The TWIGL calculations were done with a much too coarse a mesh spacing. However, comparing FMP2DT with TWIGL's flux shape showed that the precursor contribution was at least generating a similar source vector as was TWIGL's source vector. And by presenting the TWIGL comparison, a demonstration of some of FMP2DT's input characteristics was accomplished. The benchmarks with the exact flux in infinite XZ and RZ geometries did establish FMP2DT's computation creditability.

Since a  $P_1$  approximation is most suspect near boundaries and strong sources, it is most likely that FMP2DT would show the greatest error nearest to the boundary or source. Figures 16 and 17 show this to be true. Angular flux approximations usually do not predict the early time behavior of the flux because the wave behavior of the flux is not fully accounted for [Ref. 29]. However, given time after the source is turned off, the error disappears, even in close proximity to the boundary. This implies that the flux has time to become more isotropic so that the  $P_1$  approximation is a better representation of the angular flux.

The fact that a  $P_1$  approximation has difficulty predicting the early behavior of the flux is compounded by the fact that the source was 0.0625 cm thick. This means that at one second, the leading edge of the wave is at 1.0625 cm because the neutron velocity is 1 cm/sec. Likewise, there is an offset in the leading edge at 3 and 5 sec. This implies that, at these times, the corresponding calculations at 1, 3, and 5 MFPs are not predicting the leading edge of the wave since it has already passed. Looking at the percent relative error for slab geometry in Table 10, the largest error for these MFPs is at times  $t = 1$ ,  $t = 3$ , and  $t = 5$  sec. Looking at Tables 8 and 9, at 3 and 5 MFPs, it appears that the flux is over predicted. This supports the fact

that the leading edge of the wave has already pass through.

For RZ geometry, similar behavior is true. There is an inherent radial dependency for cylindrical geometry that is more pronounced than for slab geometry. The largest errors are for the earlier time fluxes. Looking at Figures 23 and 24, the early time FMP2DT flux shape at 2 MFPs appear to be taking the shape of the 3 MFP flux shape. This again supports the suggestion that the leading edge of the wave has already passed through. Experiments with the mesh spacing also seemed to confirm this.

Overall, the benchmark results with the exact flux are remarkably good. Usually, comparisons between transport codes and exact answers given in literature are for several MFPs from the source and boundary. This is because most codes are diffusion codes, and diffusion theory breaks down near the boundary. Diffusion codes do not represent the anisotropic nature of the leading edge of the wave at early time steps. After a few MFPs, the flux becomes more isotropic because of resulting collisions, and diffusion theory becomes more valid. Normally, a  $P_1$  approximation gives a better representation of the anisotropic nature of the flux and is better representation of the leading edge of the wave at earlier time. If more accuracy is desired at early time, then a larger  $P_n$  approximation would be a better model for the angular flux. But as the  $P_n$  approximations are made and programmed, the computational costs rise substantially. Thus, the  $P_1$  approximation in FMP2DT still is economically attractive, and the early time errors may be acceptable for most computations.

In the next section, we examine some applications for FMP2DT, and identify some few group problems where FMP2DT can be used as an analytical tool.

## 8 FMP2DT Applications

FMP2DT has applications to many nuclear engineering problems of interest to a number of communities. For examples, two problems were chosen, both in RZ geometry. The first one can only be resolved with decay of a critical reactor after injection of a pulse of neutrons. This experiment is often used to determine neutron lifetime estimates in a new or research reactor. The second experiment is representative of most pulsed logging problems. Two dimensional effects can dominate the measurements to the extent that simpler one dimensional models are useless. These problems are only to demonstrate FMP2DT. Therefore, no detailed physics will be developed. For example, for the first sample problem, FMP2DT will show how it can aid in collecting flux data for a Rossi-alpha experiment. However, the actual value of alpha will not be calculated.

### 8.1 AGN-201 Rossi-Alpha Problem

The first example problem chosen entailed modeling the UNM AGN-201 reactor. The AGN-201 is a low-power thermal reactor used mostly for training purposes. It is a right cylinder core, 25 cm in diameter. The fuel is a mixture of 20% enriched  $\text{UO}_2$  and polyethylene. The critical mass of the reactor is about 665 grams of  $\text{U}^{235}$ .

The experiment modeled involved a pulsed source located at the center of the UNM AGN-201 reactor that was initially operating at a critical state. This type of experiment is known as a *Rossi-alpha* experiment. A pulse of neutrons is injected into the reactor with a spatial distribution that excites multiple spatial modes. After a period of time, all modes other than the fundamental mode die out. The decay of the fundamental mode then can be related to the neutron lifetime or generation time in the critical reactor. The crucial piece of information that the calculation can

provide is the time at which counters can be gated on to measure the fundamental mode decay. If the counters are gated on too soon, the fundamental mode will be contaminated by measurements of the higher modes. If the counters are gated on too late, the data will suffer from poor resolution.

The two dimensional time dependent calculation can be recorded at multiple locations. When the time history of the flux at all spatial locations has the same exponential decay on a semi-log plot, all higher modes have decayed out. At this time the counters can be gated on and the decay data recorded.

### 8.1.1 AGN Calculation Description

The geometry for this problem is shown in Figure 28. The source was turned on for one microsecond and then turned off. The source energy was set at 0.01 MeV. The magnitude of the source energy was chosen arbitrarily and poses no significance here. The mesh was about 1 cm in the core for the radial direction, and 1 cm in the axial direction. The  $\Delta t$  for this problem was 20 microseconds for 50 steps. The calculations were stopped at 1.001 millisecond. The initial flux was generated by a FEMP2D calculation. The data were taken at the axial center line which is at  $z=0$  cm in Figure 28. The radial values were at  $r=0.985, 2.954, 4.923, 6.982,$  and  $8.861$  cm. These radial positions are all in the core. The last position was chosen to stay away from the core and graphite interface since the reflection of the neutrons from the graphite changes the slope of the flux shape. A three group problem was modeled using cross section data from an AMPX library. This was because of the availability of the cross section set, and three groups are enough to demonstrate FEMP2DT's multigroup computational ability. Table 15 shows the energy group structure for this problem.

Group	E Max (eV)	E Min (eV)
1	1.7330E+07	1.0000E+07
2	1.0000E+07	9.9990E-02
3	9.9990E-02	1.0000E-05

Table 15: Three Group Energy Structure

### 8.1.2 AGN Results

Figure 29 shows the plot of the thermal flux at the stated core positions. From the graph, it can be seen that after about 0.27 milliseconds, the slopes of the thermal flux are the same for all the radial positions. This implies that all but the fundamental flux mode has died out. This is the time to gate the counters on and record the flux data. Any time previous would result in higher mode data contamination since the slope is not straight for all spatial points.

Next, we turn our attention to a uranium logging problem. It also entails observing neutron flux decay much like the Rossi-alpha observations done here.

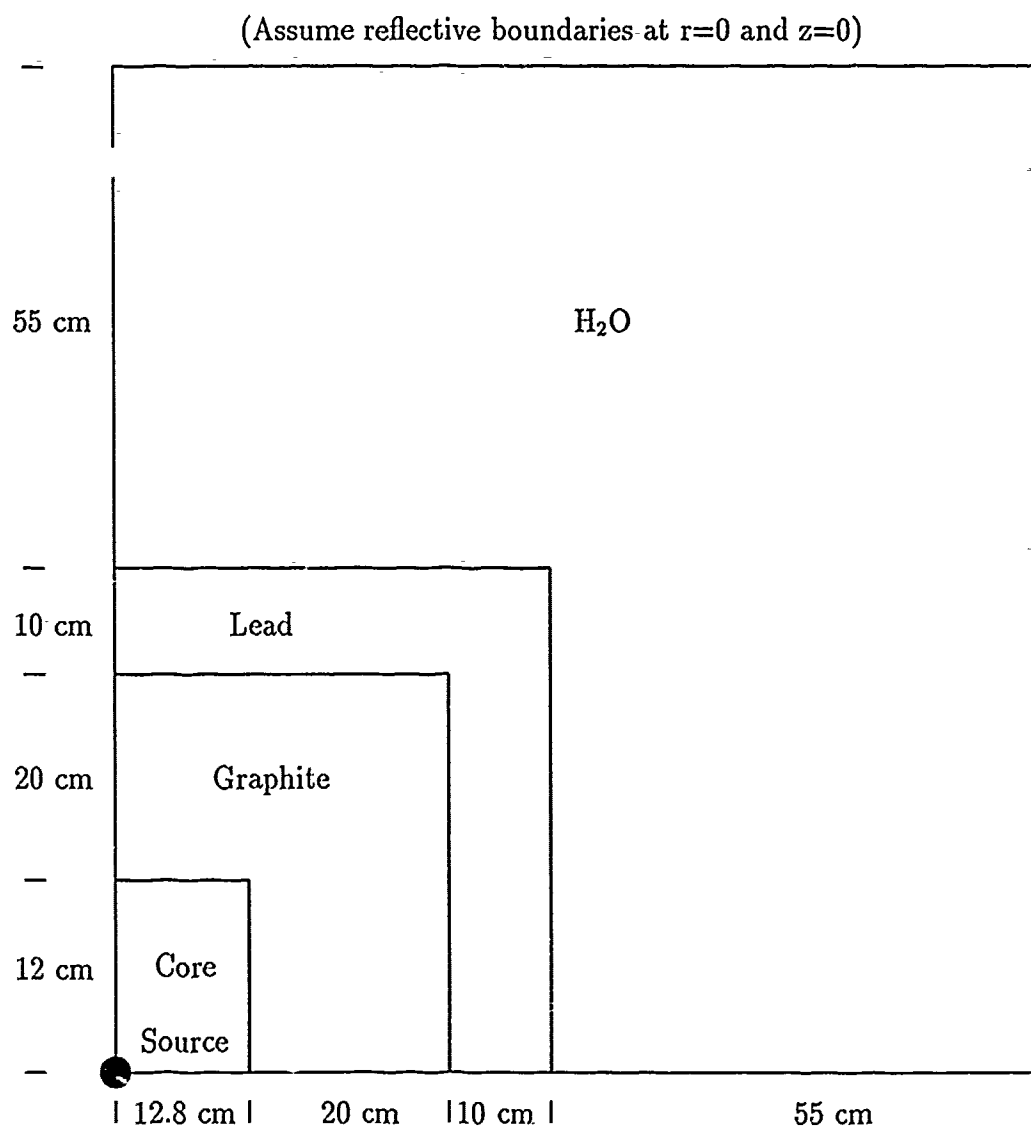


Figure 28: AGN Geometry



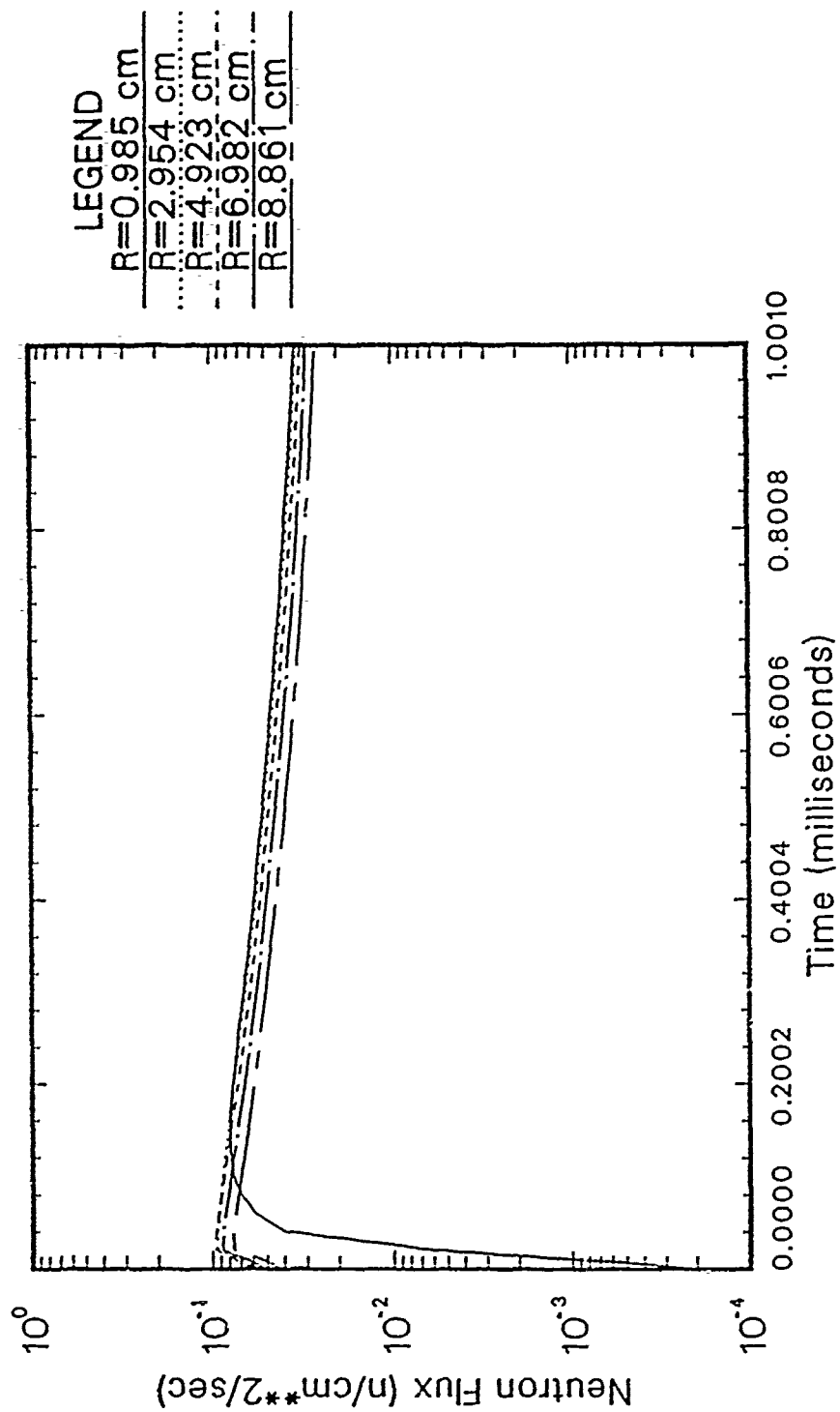


Figure 29: Flux Decay for the AGN-201 Reactor

## 8.2 Uranium Logging Problem

The search for uranium in soil is accomplished by what is called a uranium borehole logging procedure. A large hole is bored into ore-bearing rock formations, and either a pulsable source or some neutron source such as  $^{252}\text{Cf}$  is inserted. The resulting decay of prompt fission neutrons in epithermal energy region is observed. Rock formations with uranium present will show an increase for short time as a result of fission events, whereas formations without uranium will show a constant rate of epithermal neutron population decay.

The model chosen was the prompt neutron logging problem developed by James H. Renken [Ref. 32]. Renken's work was performed in one dimensional geometry and assumed that a 14 MeV source and a neutron detector were co-located. This is physically impossible. In fact they are separated by 10's of centimeters. Since this is true, diffusion of the thermal neutrons must be considered in the analysis as well as absorption. A two dimensional model provides a much better tool to analyze data from this physical problem.

When the logging problem is modeled, the fundamental problem that is correlated with the material properties of the interrogated rock is the long time (hundreds of microseconds) decay constant of the thermal neutron population. This decay constant will vary with distance from the source if thermal neutron diffusion is present. The analysis presented here demonstrates this to be the case and indicates that an individual probe must be calibrated for the source to detector spacing involved. This type of analysis can be useful for all pulsed logging systems.

### 8.2.1 Logging Calculation Description

The logging geometry is shown in Figure 30. A borehole is drilled into potential ore bearing rock. The borehole has a diameter of about 4 cm and is filled with water. A probe, about 3 cm in diameter and 60 cm in length, is inserted into the borehole. The detector is about 4 cm from the source. The source is about 1 cm in diameter and is located in the center of the probe as shown.

The same three group structure as used for the previous example is used for this problem. The group structure is shown in Table 15. The radial mesh was about 1 cm in the axial and radial directions. (Except where material interfaces occurred.) The source energy was 14 MeV, and it was turned on for 10 microseconds. The flux data were then tabulated for 590 microseconds with a  $\Delta t = 11.8$  microseconds for 50 time steps. The soil contains a mixture of  $^{235}\text{U}$ ,  $^{238}\text{U}$ ,  $\text{H}_2\text{O}$ , and  $\text{SiO}_2$ . The production of delayed neutrons is neglected because their numbers will be small during the short counting period. A reflective boundary condition is used at  $r = 0$  cm and vacuum boundary conditions are used at  $r = 35$  cm,  $z = 0$  cm, and  $z = 60$  cm.

### 8.2.2 Logging Problem Results

Figure 31 shows the graph of the flux decay at  $r = 0$  cm and axial positions of  $z = 38, 44, 50, 56$ , and  $59$  cm. The source, also located at  $r = 0$  cm, was between  $z = 31$  and  $32$  cm. As shown, the flux has different slopes for each axial position. This different slope data clearly show that each position does have a different decay constant. This must be taken into account in detector calibration to insure credible counting.



(Source is Between 31 and 32 cm)

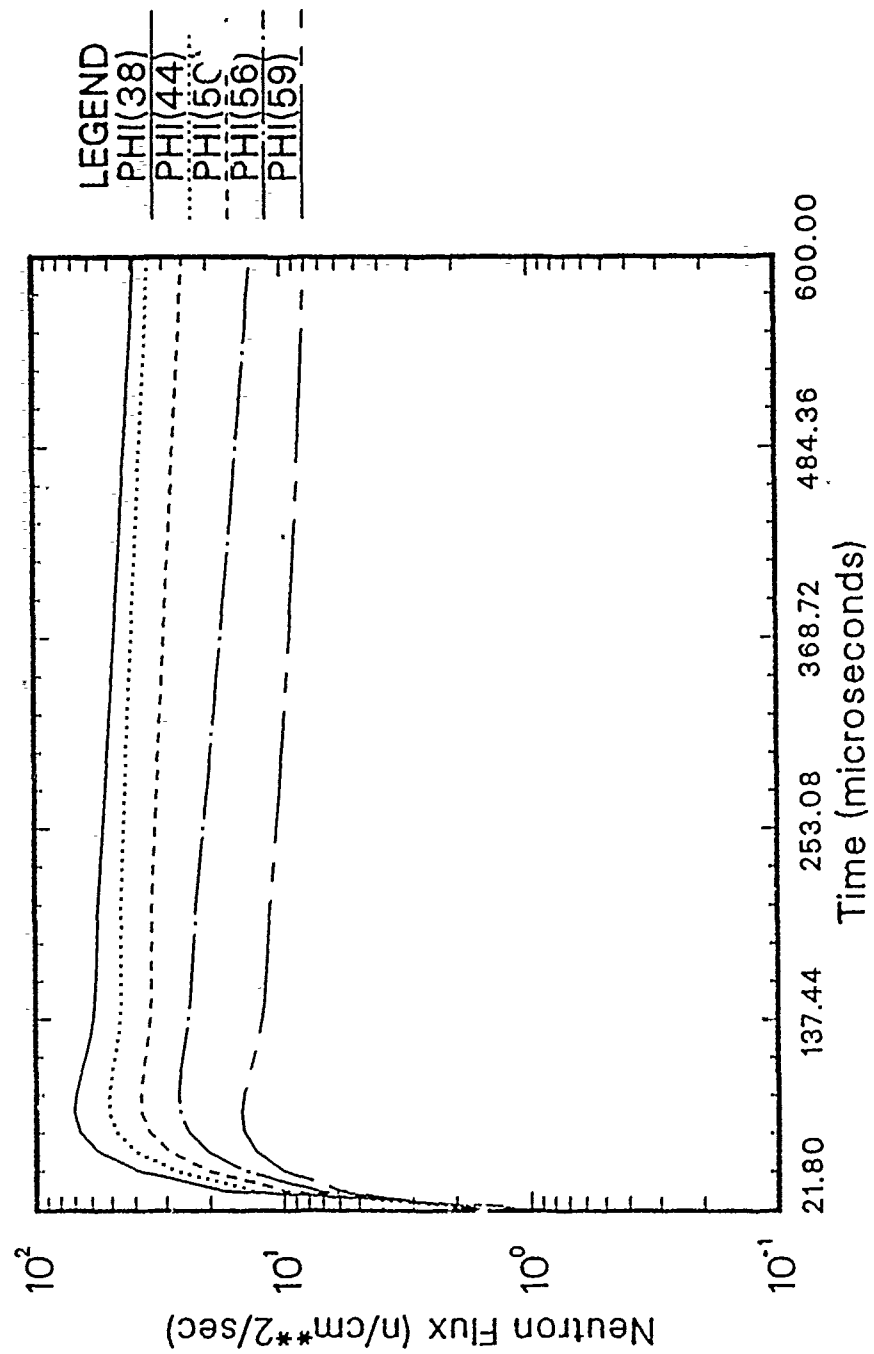


Figure 31: Flux Decay for the Logging Problem

## 9 Conclusions

The new code, FMP2DT, demonstrated most of the characteristics that were desired before this research began. Indeed, its benchmarking turned out to be better than expected. Its input deck, while somewhat tedious for source transients with many time steps, is fairly straight forward with respect to its sister FEMP codes. The following is to identify some of FMP2DT's characteristics.

The nature of having to calculate the radial and axial currents,  $\Psi_{10}$  and  $\Psi_{11}$ , means having to invert two matrices. Depending on the mesh size of the problem, and the number of energy groups considered, this can be a major, and very costly, operation. Also, the calculation of the precursor concentrations,  $C$ , can be even more computationally expensive depending on the number of precursor families to be modeled. All of these computations are magnified by the number of time steps chosen. Therefore, selecting the spatial mesh wisely, and using a group structure that is just fine enough to satisfy the problem physics is prudent. However, the user may not know these optimum configurations. In that event, a guess for an equal  $\Delta x$  and  $\Delta z$  may be selected and a  $\Delta t$  chosen to give a tolerable computational time. Then some variations from these values can be used to insure convergence. Determination of the proper group structure is subject to choosing the number of groups, running the problem, collapsing the groups, and observing the flux change.

As stated in earlier sections, the Euler backward differencing scheme for time discretization is inherently stable. However, the user should be careful not to assume convergence upon an initial run; *stability does not imply convergence*. This is especially true for time dependent problems. FMP2DT's answer needs to be compared with more than one run for any new problem.

The ability for a calculation of  $\chi_k^q$  is unique. These values are very difficult to

find. However, if data are available to establish the delayed group spectrum, then it can be entered in FMP2DT's input deck. In fact, if any cross section parameters are available, those may be entered likewise.

The benchmarking of FMP2DT established FMP2DT's computational accuracy. The errors shown in the early times for both XZ and RZ geometries are consistent with theory. With differing neutron energy groups, where the neutron velocities are much faster, the early time error may not be as pronounced.

The few group problems demonstrated some practical applications for FMP2DT. The AGN-201 problem demonstrated how an experiment, such as Rossi-alpha, would be accomplished by gating the counter in the proper time interval to insure credible data recording.

The uranium logging data showed that for different spatial points in the borehole, the flux decays at different rates. Therefore, for the detector to yield valuable information, it must be calibrated for the source to detector spacing. Thus, the two dimensional diffusion effects need to be accounted for.

FMP2DT can be enhanced in many ways. Here are a few suggestions for future work and research.

## **9.1 Future Research**

The first thing that could enhance FMP2DT is to program the ability to make the cross sections temperature dependent. This could be done by coupling the FMP2DT equations with some thermal-hydraulic equations, and/or possibly with equations describing heat generation due to particle interactions. Included with the particle interactions are the effects of gamma heating. Of course, because of computational cost and complexities, there are limits as to the detail for all of this. But at least some work of this nature could be feasible.

When doing the benchmarks with Ganapol's data for RZ and XZ geometries, the greatest error was at the early times. A  $P_n$  expansion of the angular flux with  $n > 1$  would be more accurate in describing the angular flux's anisotropic nature at those times. Also, it would permit a more accurate representation at boundaries and material interfaces. This might be the best enhancement for practical purposes.

Since we have a two dimensional time dependent code, it would be natural to develop a three dimensional version. The complexity of this effort is not trivial, even with the two dimensional schemes to use as a starting points. But a three dimensional version would allow computations with systems that do not possess azimuthal symmetry in the streaming physics.

Second, some small modifications to FMP2DT could be made. This could include the development of an option for  $R\theta$  geometry. Modifications to the input scheme could be done so that an inhomogeneous source that's turned on and off would not need an input entry describing its state for every time step. At present, this input is very lengthy. Also, it would be desirable to include an option in FMP2DT to calculate adjoint fluxes. These and several other minor options could serve as some sort of academic problem.



## Appendix A: Vector and Matrix Definitions

The vector Equations (61) and (74) are the result of applying the multigroup approximation to the transport equation. They have been defined for  $G$  energy groups.  $g = 1$  is defined as the highest energy group and  $g = G$  is defined as the lowest, sometimes referred as the thermal energy group. Therefore,  $g = 1, 2, \dots, G$ . We now will define the matrices and vectors used in the XZ and RZ geometry solutions. All the matrices are piece-wise constant in an interval  $\Delta x$  and  $\Delta z$  or  $\Delta r$ . For simplicity, their following definitions will not carry any spatial interval subscripts.

Define  $\Sigma^{00}$ :

$$\Sigma^{00} = \begin{Bmatrix} \Sigma_t^1 - \Sigma_{s_0}^{1 \rightarrow 1} + \frac{1}{v_1 \Delta t} & -\Sigma_{s_0}^{2 \rightarrow 1} & \dots & -\Sigma_{s_0}^{G \rightarrow 1} \\ -\Sigma_{s_0}^{1 \rightarrow 2} & \Sigma_t^2 - \Sigma_{s_0}^{2 \rightarrow 2} + \frac{1}{v_2 \Delta t} & \dots & -\Sigma_{s_0}^{G \rightarrow 2} \\ \vdots & \vdots & \ddots & \vdots \\ -\Sigma_{s_0}^{1 \rightarrow G} & -\Sigma_{s_0}^{2 \rightarrow G} & \dots & \Sigma_t^G - \Sigma_{s_0}^{G \rightarrow G} + \frac{1}{v_G \Delta t} \end{Bmatrix}$$

$\Sigma^{00}$  is a combination of  $\Sigma_t^g$ , the total cross section for the  $g^{th}$  energy group,  $\Sigma_{s_0}^{g' \rightarrow g}$ , the inscattering cross section for the  $g^{th}$  energy group, and the  $\frac{1}{v_g \Delta t}$  diagonal entries come from combining (addition) to the  $V$  matrix. The same similar combinations are made with the  $\Sigma^{10}$  and  $\Sigma^{11}$  matrices.

Define  $\Sigma^{10}$ :

$$\Sigma^{10} = \begin{Bmatrix} \Sigma_t^1 - \Sigma_{s_1}^{1 \rightarrow 1} + \frac{1}{v_1 \Delta t} & -\Sigma_{s_1}^{2 \rightarrow 1} & \dots & -\Sigma_{s_1}^{G \rightarrow 1} \\ -\Sigma_{s_1}^{1 \rightarrow 2} & \Sigma_t^2 - \Sigma_{s_1}^{2 \rightarrow 2} + \frac{1}{v_2 \Delta t} & \dots & -\Sigma_{s_1}^{G \rightarrow 2} \\ \vdots & \vdots & \ddots & \vdots \\ -\Sigma_{s_1}^{1 \rightarrow G} & -\Sigma_{s_1}^{2 \rightarrow G} & \dots & \Sigma_t^G - \Sigma_{s_1}^{G \rightarrow G} + \frac{1}{v_G \Delta t} \end{Bmatrix}$$

$$D^{10} = \{\Sigma^{10}\}^{-1} \text{ and } \bar{D}^{10} = \frac{1}{3} D^{10}$$

Define  $\Sigma^{11}$ :

$$\Sigma^{11} = \begin{pmatrix} \Sigma_t^1 - \Sigma_{s_1}^{1 \rightarrow 1} + \frac{1}{v_1 \Delta t} & -\Sigma_{s_1}^{2 \rightarrow 1} & \dots & -\Sigma_{s_1}^{G \rightarrow 1} \\ -\Sigma_{s_1}^{1 \rightarrow 2} & \Sigma_t^2 - \Sigma_{s_1}^{2 \rightarrow 2} + \frac{1}{v_2 \Delta t} & \dots & -\Sigma_{s_1}^{G \rightarrow 2} \\ \vdots & \vdots & \ddots & \vdots \\ -\Sigma_{s_1}^{1 \rightarrow G} & -\Sigma_{s_1}^{2 \rightarrow G} & \dots & \Sigma_t^G - \Sigma_{s_1}^{G \rightarrow G} + \frac{1}{v_G \Delta t} \end{pmatrix}$$

$$D^{11} = \{\Sigma^{11}\}^{-1} \text{ and } \bar{D}^{11} = \frac{1}{3} D^{11}$$

Define  $\Sigma^f$ :

$$\Sigma^f = \begin{pmatrix} \chi^1 \nu^1 \Sigma_f^1 & \chi^1 \nu^2 \Sigma_f^2 & \dots & \chi^1 \nu^G \Sigma_f^G \\ \chi^2 \nu^1 \Sigma_f^1 & \chi^2 \nu^2 \Sigma_f^2 & \dots & \chi^2 \nu^G \Sigma_f^G \\ \vdots & \vdots & \ddots & \vdots \\ \chi^G \nu^1 \Sigma_f^1 & \chi^G \nu^2 \Sigma_f^2 & \dots & \chi^G \nu^G \Sigma_f^G \end{pmatrix}$$

$\chi^g$  in  $\Sigma^f$  above is defined as:

$$\chi^g = \chi_p^g (1 - \beta) + \sum_{k=1}^n \chi_k^g \beta_k \left( \frac{1}{1 + \frac{1}{\lambda_k \Delta t}} \right)$$

The data for  $\Sigma^{00}$ ,  $\Sigma^{10}$ ,  $\Sigma^{11}$  and  $\Sigma^f$  are given in a cross section set that is determined experimentally.

Define  $V$ :

$$V = \begin{pmatrix} \frac{1}{v_1 \Delta t} & 0 & \dots & 0 \\ 0 & \frac{1}{v_2 \Delta t} & \dots & 0 \\ \vdots & \dots & \ddots & \vdots \\ 0 & \dots & \dots & \frac{1}{v_G \Delta t} \end{pmatrix}$$

$v_g$  is the neutron velocity related to the neutron energy.  $\Delta t$  is the time discretization or time step in consideration.

For the vector definitions, their spatial superscript  $i, j$  will refer to the  $ij^{th}$  mesh point. The superscript  $(N+1)$  will relate to the present time step  $(\Delta t)$  and  $(N)$  will relate to the previous time step. The energy group will be the number appearing under the time step designation.

Define the  $\Psi_{00}$  vectors:

$$\Psi_{00ij}^{(N+1)} = \begin{Bmatrix} \psi_{00ij}^{(N+1)1} \\ \psi_{00ij}^{(N+1)2} \\ \vdots \\ \psi_{00ij}^{(N+1)G} \end{Bmatrix} \quad \Psi_{00ij}^{(N)} = \begin{Bmatrix} \psi_{00ij}^{(N)1} \\ \psi_{00ij}^{(N)2} \\ \vdots \\ \psi_{00ij}^{(N)G} \end{Bmatrix}$$

Define the  $\Psi_{10}$  vectors:

$$\Psi_{10ij}^{(N+1)} = \begin{Bmatrix} \psi_{10ij}^{(N+1)1} \\ \psi_{10ij}^{(N+1)2} \\ \vdots \\ \psi_{10ij}^{(N+1)G} \end{Bmatrix} \quad \Psi_{10ij}^{(N)} = \begin{Bmatrix} \psi_{10ij}^{(N)1} \\ \psi_{10ij}^{(N)2} \\ \vdots \\ \psi_{10ij}^{(N)G} \end{Bmatrix}$$

Define the  $\Psi_{11}$  vectors:

$$\Psi_{11ij}^{(N+1)} = \begin{Bmatrix} \psi_{11ij}^{(N+1)1} \\ \psi_{11ij}^{(N+1)2} \\ \vdots \\ \psi_{11ij}^{(N+1)G} \end{Bmatrix} \quad \Psi_{11ij}^{(N)} = \begin{Bmatrix} \psi_{11ij}^{(N)1} \\ \psi_{11ij}^{(N)2} \\ \vdots \\ \psi_{11ij}^{(N)G} \end{Bmatrix}$$

Define the precursor source:

$$\overline{C}_{ij}^{(N)g} = \sum_{k=1}^n \frac{\chi_k^g \lambda_k C_{kij}^{(N)}}{1 + \lambda_k \Delta t}$$

Then the precursor vector may be defined as:

$$C_{ij}^{(N)} = \begin{Bmatrix} \bar{C}_{ij}^{(N)1} \\ \bar{C}_{ij}^{(N)2} \\ \vdots \\ \bar{C}_{ij}^{(N)G} \end{Bmatrix}$$

Define the inhomogeneous sources:

$$S_{00ij}^{(N+1)} = \begin{Bmatrix} S_{00ij}^{(N+1)1} \\ S_{00ij}^{(N+1)2} \\ \vdots \\ S_{00ij}^{(N+1)G} \end{Bmatrix} \quad S_{10ij}^{(N+1)} = \begin{Bmatrix} S_{10ij}^{(N+1)1} \\ S_{10ij}^{(N+1)2} \\ \vdots \\ S_{10ij}^{(N+1)G} \end{Bmatrix} \quad S_{11ij}^{(N+1)} = \begin{Bmatrix} S_{11ij}^{(N+1)1} \\ S_{11ij}^{(N+1)2} \\ \vdots \\ S_{11ij}^{(N+1)G} \end{Bmatrix}$$

Note: The  $\Sigma^{10}$  and the  $\Sigma^{11}$  matrices were presented in the derivation of the equations as if they were different. Examination of the entries show that they really are not. Thus, the diffusion matrices,  $D^{10}$  and  $D^{11}$  are also the same.

## Appendix B: Integration Summaries

The linear hat functions have different values depending on the interval in question. For example, for an interval in the  $x$  direction from  $i - 1$  to  $i + 1$ ,  $B_i(x)$  has two different values. This can be seen in Figure 1. Each interior  $B$ -spline then overlaps itself and its two nearest neighbors. Therefore, the  $B$  splines are defined:

In the  $x$  direction for  $p = i - 1, i$ , and  $i + 1$ :

$$\begin{aligned}
 B_{i-1}(x) &= \frac{x_i - x}{x_i - x_{i-1}} \quad \text{for } x_{i-1} \leq x \leq x_i & \frac{dB_{i-1}(x)}{dx} &= \frac{-1}{x_i - x_{i-1}} \\
 B_i(x) &= \frac{x - x_{i-1}}{x_i - x_{i-1}} \quad \text{for } x_{i-1} \leq x \leq x_i & \frac{dB_i(x)}{dx} &= \frac{1}{x_i - x_{i-1}} \\
 B_i(x) &= \frac{x_{i+1} - x}{x_{i+1} - x_i} \quad \text{for } x_i \leq x \leq x_{i+1} & \frac{dB_i(x)}{dx} &= \frac{-1}{x_{i+1} - x_i} \\
 B_{i+1}(x) &= \frac{x - x_i}{x_{i+1} - x_i} \quad \text{for } x_i \leq x \leq x_{i+1} & \frac{dB_{i+1}(x)}{dx} &= \frac{1}{x_{i+1} - x_i}
 \end{aligned}$$

In the  $z$  direction for  $q = j - 1, j$ , and  $j + 1$ :

$$\begin{aligned}
 B_{j-1}(z) &= \frac{z_j - z}{z_j - z_{j-1}} \quad \text{for } z_{j-1} \leq z \leq z_j & \frac{dB_{j-1}(z)}{dz} &= \frac{-1}{z_j - z_{j-1}} \\
 B_j(z) &= \frac{z - z_{j-1}}{z_j - z_{j-1}} \quad \text{for } z_{j-1} \leq z \leq z_j & \frac{dB_j(z)}{dz} &= \frac{1}{z_j - z_{j-1}} \\
 B_j(z) &= \frac{z_{j+1} - z}{z_{j+1} - z_j} \quad \text{for } z_j \leq z \leq z_{j+1} & \frac{dB_j(z)}{dz} &= \frac{-1}{z_{j+1} - z_j} \\
 B_{j+1}(z) &= \frac{z - z_j}{z_{j+1} - z_j} \quad \text{for } z_j \leq z \leq z_{j+1} & \frac{dB_{j+1}(z)}{dz} &= \frac{1}{z_{j+1} - z_j}
 \end{aligned}$$

The  $B$  splines in the  $z$  direction are the same for both XZ and RZ geometries.

In the  $r$  direction for  $p = i - 1, i,$  and  $i + 1$

$$B_{i-1}(r) = \frac{r_i - r}{r_i - r_{i-1}} \quad \text{for } r_{i-1} \leq r \leq r_i \quad \frac{d B_{i-1}(r)}{dr} = \frac{-1}{r_i - r_{i-1}}$$

$$B_i(r) = \frac{r - r_{i-1}}{r_i - r_{i-1}} \quad \text{for } r_{i-1} \leq r \leq r_i \quad \frac{d B_i(r)}{dr} = \frac{1}{r_i - r_{i-1}}$$

$$B_i(r) = \frac{r_{i+1} - r}{r_{i+1} - r_i} \quad \text{for } r_i \leq r \leq r_{i+1} \quad \frac{d B_i(r)}{dr} = \frac{-1}{r_{i+1} - r_i}$$

$$B_{i+1}(r) = \frac{r - r_i}{r_{i+1} - r_i} \quad \text{for } r_i \leq r \leq r_{i+1} \quad \frac{d B_{i+1}(r)}{dr} = \frac{1}{r_{i+1} - r_i}$$

Now define:

$h_{i-1} = x_i - x_{i-1}$  and  $h_i = x_{i+1} - x_i$  for XZ geometry.

$h_{i-1} = r_i - r_{i-1}$  and  $h_i = r_{i+1} - r_i$  for RZ geometry.

$h_{j-1} = z_j - z_{j-1}$  and  $h_j = z_{j+1} - z_j$  for both geometries.

For integration in the  $r$  direction with an  $r$  factor in the integrand:

Define:

$$\begin{aligned} R_1(i) &= \frac{1}{12} (r_i^2 - r_{i-1}^2) \\ R_2(i) &= \frac{1}{12} (3r_i^2 - 2r_i r_{i-1} - r_{i-1}^2) \\ R_3(i) &= \frac{1}{12} (r_{i+1}^2 + 2r_{i+1} r_i - 3r_i^2) \\ R_4(i) &= \frac{1}{12} (r_{i+1}^2 - r_i^2) = R_1(i-1) \\ R_5(i) &= \frac{-1}{2} \left( \frac{r_i + r_{i-1}}{r_i - r_{i-1}} \right) \\ R_6(i) &= \frac{1}{2} \left( \frac{r_i + r_{i-1}}{r_i - r_{i-1}} \right) = -R_5(i) \\ R_7(i) &= \frac{1}{2} \left( \frac{r_{i+1} + r_i}{r_{i+1} - r_i} \right) \\ R_8(i) &= \frac{-1}{2} \left( \frac{r_{i+1} + r_i}{r_{i+1} - r_i} \right) = -R_7(i) \\ R_9(i) &= \frac{1}{6} (r_i + 2r_{i-1}) \\ R_{10}(i) &= \frac{1}{6} (2r_i + r_{i-1}) \end{aligned}$$

$$R_{11}(i) = \left(\frac{-1}{6}\right) (r_{i+1} + 2r_i) = -R_9(i-1)$$

$$R_{12}(i) = \left(\frac{-1}{6}\right) (2r_{i+1} + r_i) = -R_{10}(i-1)$$

Each material matrix is piece-wise continuous in a given  $xz$  or  $rz$  interval. They possess subscripts identifying the specific interval where they belong. Consider the following example. Let  $\Sigma^{00}$  be the matrix in question. Figure 32 shows how it might fit in a two dimensional slab mesh scheme. Let  $M^1$ ,  $M^2$ ,  $M^3$  and  $M^4$  represent  $\Sigma^{00}$

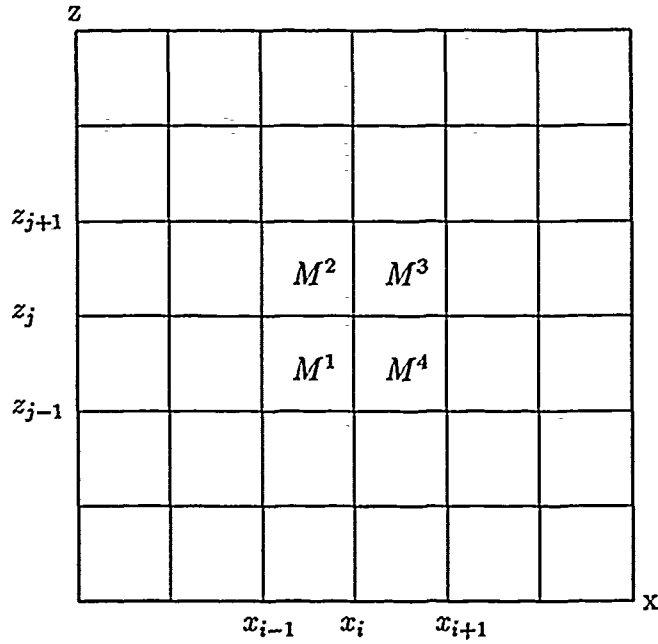


Figure 32: Piece-Wise Material Matrix Example

in the intervals shown. Then,

$$M^1 \equiv \Sigma_{i-1,j-1}^{00} \quad M^3 \equiv \Sigma_{i,j}^{00}$$

$$M^2 \equiv \Sigma_{i-1,j}^{00} \quad M^4 \equiv \Sigma_{i,j-1}^{00}$$

Thus,  $\Sigma_{i-1,j-1}^{00}$  is continuous in the interval  $h_{i-1}$  and  $h_{j-1}$ ,  $\Sigma_{i-1,j}^{00}$  is continuous in the interval  $h_{i-1}$  and  $h_j$ ,  $\Sigma_{i,j}^{00}$  is continuous in the interval  $h_i$  and  $h_j$ , and  $\Sigma_{i,j-1}^{00}$  is continuous in the interval  $h_i$  and  $h_{j-1}$ . All other material matrices are likewise

determined. Now the integrations are addressed.

In the  $x$  direction:

$$\int_{x_{i-1}}^{x_i} \frac{d B_{i-1}(x)}{dx} \frac{d B_i(x)}{dx} dx = \frac{-1}{h_{i-1}}$$

$$\int_{x_{i-1}}^{x_i} \frac{d B_i(x)}{dx} \frac{d B_i(x)}{dx} dx = \frac{1}{h_{i-1}}$$

$$\int_{x_i}^{x_{i+1}} \frac{d B_i(x)}{dx} \frac{d B_i(x)}{dx} dx = \frac{1}{h_i}$$

$$\int_{x_i}^{x_{i+1}} \frac{d B_i(x)}{dx} \frac{d B_i(x)}{dx} dx = \frac{-1}{h_i}$$

$$\int_{x_{i-1}}^{x_i} B_{i-1}(x) B_i(x) dx = \frac{h_{i-1}}{6}$$

$$\int_{x_{i-1}}^{x_i} B_i(x) B_i(x) dx = \frac{h_{i-1}}{3}$$

$$\int_{x_i}^{x_{i+1}} B_i(x) B_i(x) dx = \frac{h_i}{3}$$

$$\int_{x_i}^{x_{i+1}} B_{i+1}(x) B_i(x) dx = \frac{h_i}{6}$$

$$\int_{x_{i-1}}^{x_i} B_{i-1}(x) \frac{d B_i(x)}{dx} dx = \frac{1}{2}$$

$$\int_{x_{i-1}}^{x_i} B_i(x) \frac{d B_i(x)}{dx} dx = \frac{1}{2}$$

$$\int_{x_i}^{x_{i+1}} B_i(x) \frac{d B_i(x)}{dx} dx = \frac{-1}{2}$$

$$\int_{x_i}^{x_{i+1}} B_{i+1}(x) \frac{d B_i(x)}{dx} dx = \frac{-1}{2}$$



In the  $z$  direction:

$$\int_{z_{j-1}}^{z_j} \frac{dB_{j-1}(z)}{dz} \frac{dB_j(z)}{dz} dz = \frac{-1}{h_{j-1}}$$

$$\int_{z_{j-1}}^{z_j} \frac{dB_j(z)}{dz} \frac{dB_j(z)}{dz} dz = \frac{1}{h_{j-1}}$$

$$\int_{z_j}^{z_{j+1}} \frac{dB_j(z)}{dz} \frac{dB_j(z)}{dz} dz = \frac{1}{h_j}$$

$$\int_{z_j}^{z_{j+1}} \frac{dB_j(z)}{dz} \frac{dB_j(z)}{dz} dz = \frac{-1}{h_j}$$

$$\int_{z_{j-1}}^{z_j} B_{j-1}(z) B_j(z) dz = \frac{h_{j-1}}{6}$$

$$\int_{z_{j-1}}^{z_j} B_j(z) B_j(z) dz = \frac{h_{j-1}}{3}$$

$$\int_{z_j}^{z_{j+1}} B_j(z) B_j(z) dz = \frac{h_j}{3}$$

$$\int_{z_j}^{z_{j+1}} B_{j+1}(z) B_j(z) dz = \frac{h_j}{6}$$

$$\int_{z_{j-1}}^{z_j} B_{j-1}(z) \frac{dB_j(z)}{dz} dz = \frac{1}{2}$$

$$\int_{z_{j-1}}^{z_j} B_j(z) \frac{dB_j(z)}{dz} dz = \frac{1}{2}$$

$$\int_{z_j}^{z_{j+1}} B_j(z) \frac{dB_j(z)}{dz} dz = \frac{-1}{2}$$

$$\int_{z_j}^{z_{j+1}} B_{j+1}(z) \frac{dB_j(z)}{dz} dz = \frac{-1}{2}$$

In the  $r$ -direction:

$$\int_{r_{i-1}}^{r_i} B_{i-1}(r) B_i(r) r dr = R_1(i)$$

$$\int_{r_{i-1}}^{r_i} B_i(r) B_i(r) r dr = R_2(i)$$

$$\int_{r_i}^{r_{i+1}} B_i(r) B_i(r) r dr = R_3(i)$$

$$\int_{r_i}^{r_{i+1}} B_{i+1}(r) B_i(r) r dr = R_4(i)$$

$$\int_{r_{i-1}}^{r_i} \frac{d B_{i-1}(r)}{dr} \frac{d B_i(r)}{dr} r dr = R_5(i)$$

$$\int_{r_{i-1}}^{r_i} \frac{d B_i(r)}{dr} \frac{d B_i(r)}{dr} r dr = R_6(i)$$

$$\int_{r_i}^{r_{i+1}} \frac{d B_i(r)}{dr} \frac{d B_i(r)}{dr} r dr = R_7(i)$$

$$\int_{r_i}^{r_{i+1}} \frac{d B_i(r)}{dr} \frac{d B_i(r)}{dr} r dr = R_8(i)$$

$$\int_{r_{i-1}}^{r_i} B_{i-1}(r) \frac{d B_i(r)}{dr} r dr = R_9(i)$$

$$\int_{r_{i-1}}^{r_i} B_i(r) \frac{d B_i(r)}{dr} r dr = R_{10}(i)$$

$$\int_{r_i}^{r_{i+1}} B_i(r) \frac{d B_i(r)}{dr} r dr = R_{11}(i)$$

$$\int_{r_i}^{r_{i+1}} B_{i+1}(r) \frac{d B_i(r)}{dr} r dr = R_{12}(i)$$

Continued on the next page.

Some of the integrands in the radial direction did not have a  $r$  factor in them because it was canceled out by a  $\frac{1}{r}$  factor in the same integrand.

$$\int_{r_{i-1}}^{r_i} B_{i-1}(r) \frac{d B_i(r)}{dr} dr = \frac{1}{2}$$

$$\int_{r_{i-1}}^{r_i} B_i(r) \frac{d B_i(r)}{dr} dr = \frac{1}{2}$$

$$\int_{r_i}^{r_{i+1}} B_i(r) \frac{d B_i(r)}{dr} dr = \frac{-1}{2}$$

$$\int_{r_i}^{r_{i+1}} B_{i+1}(r) \frac{d B_i(r)}{dr} dr = \frac{-1}{2}$$

Finally there is a case that is opposite from the preceding one.

$$\int_{r_{i-1}}^{r_i} \frac{d B_{i-1}(r)}{dr} B_i(r) dr = \frac{-1}{2}$$

$$\int_{r_{i-1}}^{r_i} \frac{d B_i(r)}{dr} B_i(r) dr = \frac{1}{2}$$

$$\int_{r_i}^{r_{i+1}} \frac{d B_i(r)}{dr} B_i(r) dr = \frac{-1}{2}$$

$$\int_{r_i}^{r_{i+1}} \frac{d B_{i+1}(r)}{dr} B_i(r) dr = \frac{1}{2}$$

## Appendix C: TWIGL Cross Section Data

The following is a summary of the cross sections used to set up the FEMP calculations for the TWIGL problem. Consider a two group problem with a  $P_1$  approximation. The  $P_0$  transfer matrix is defined as:

$$\Sigma^{00} = \begin{bmatrix} \Sigma_t^1 - \Sigma_{s_0}^{1 \rightarrow 1} + \frac{1}{v_1 \Delta t} & -\Sigma_{s_0}^{2 \rightarrow 1} \\ -\Sigma_{s_0}^{1 \rightarrow 2} & \Sigma_t^2 - \Sigma_{s_0}^{2 \rightarrow 2} + \frac{1}{v_2 \Delta t} \end{bmatrix}$$

And the  $P_1$  transfer matrix is defined as:

$$(3) \Sigma^{10} = (3) \Sigma^{11} = (3) \begin{bmatrix} \Sigma_t^1 - \Sigma_{s_1}^{1 \rightarrow 1} + \frac{1}{v_1 \Delta t} & -\Sigma_{s_1}^{2 \rightarrow 1} \\ -\Sigma_{s_1}^{1 \rightarrow 2} & \Sigma_t^2 - \Sigma_{s_1}^{2 \rightarrow 2} + \frac{1}{v_2 \Delta t} \end{bmatrix}$$

For steady state calculations, the  $\frac{1}{v_g \Delta t}$  values are set to zero. The values to compute these matrices are either read in by a cross section tape, tape 16, or read in the input data from tape 5. Consider that there are two materials, and their cross section data are read in the input deck (tape 5) in the 20\*\*, 21\*\*, and 22\*\* arrays. Each material must have input for these arrays. For the TWIGL problem, the following pages show the input for the steady state calculations. For the FMP2DT calculations at time  $t = 0$ , another set of these arrays must be included for material 3. In that case, material 3's arrays would be exactly like material 1's. This will change for  $t > 0.005$  sec where other 20\*\*, 21\*\*, and 23\*\* arrays must be entered, one for each time step, reflecting the  $\Delta \Sigma$  for each entry (as described in the text).

Material 1:

20\*\*ARRAY:

$$\Sigma_t^1 = 0.2398$$

$$\Sigma_t^2 = 0.6410$$

$$\nu \Sigma_f^1 = 0.02555562$$

$$\nu \Sigma_f^2 = 0.73259410$$

$$\Sigma_a^1 = 0.00$$

$$\Sigma_a^2 = 0.43$$

$$\chi^1 = 1.0$$

$$\chi^2 = 0.0$$

21\*\*ARRAY

$$\Sigma_{s_0}^{1 \rightarrow 1} = 0.2148$$

$$\Sigma_{s_0}^{1 \rightarrow 2} = 0.0060$$

$$\Sigma_{s_0}^{2 \rightarrow 1} = 0.0000$$

$$\Sigma_{s_0}^{2 \rightarrow 2} = 0.2110$$

22\*\*ARRAY

$$(3) \Sigma_{s_1}^{1 \rightarrow 1} = 0.0$$

$$(3) \Sigma_{s_1}^{1 \rightarrow 2} = 0.0$$

$$(3) \Sigma_{s_1}^{2 \rightarrow 1} = 0.0$$

$$(3) \Sigma_{s_1}^{2 \rightarrow 2} = 0.0$$

Material 2:

20\*\*ARRAY:

$$\Sigma_t^1 = 0.2801$$

$$\Sigma_t^2 = 0.4762$$

$$\nu \Sigma_f^1 = 0.00511112$$

$$\nu \Sigma_f^2 = 0.08518539$$

$$\Sigma_a^1 = 0.00$$

$$\Sigma_a^2 = 0.13$$

$$\chi^1 = 1.0$$

$$\chi^2 = 0.0$$

21\*\*ARRAY

$$\Sigma_{s_0}^{1 \rightarrow 1} = 0.2641$$

$$\Sigma_{s_0}^{1 \rightarrow 2} = 0.0060$$

$$\Sigma_{s_0}^{2 \rightarrow 1} = 0.0000$$

$$\Sigma_{s_0}^{2 \rightarrow 2} = 0.3462$$

22\*\*ARRAY

$$(3) \Sigma_{s_1}^{1 \rightarrow 1} = 0.0$$

$$(3) \Sigma_{s_1}^{1 \rightarrow 2} = 0.0$$

$$(3) \Sigma_{s_1}^{2 \rightarrow 1} = 0.0$$

$$(3) \Sigma_{s_1}^{2 \rightarrow 2} = 0.0$$

We want to calculate for both materials:

$$\Sigma^{00} = \begin{bmatrix} \Sigma_t^1 - \Sigma_{s_0}^{1 \rightarrow 1} & -\Sigma_{s_0}^{2 \rightarrow 1} \\ -\Sigma_{s_0}^{1 \rightarrow 2} & \Sigma_t^2 - \Sigma_{s_0}^{2 \rightarrow 2} \end{bmatrix}$$

(Here we are only considering steady state conditions.)

Material 1:

$$\Sigma_t^1 - \Sigma_{s_0}^{1 \rightarrow 1} = 0.2398 - 0.2148$$

$$-\Sigma_{s_0}^{1 \rightarrow 2} = -0.006$$

$$-\Sigma_{s_0}^{2 \rightarrow 1} = 0.0$$

$$\Sigma_t^2 - \Sigma_{s_0}^{2 \rightarrow 2} = 0.6410 - 0.2110$$

Thus:

$$\Sigma^{00} = \begin{bmatrix} 0.0250 & 0.0000 \\ -0.006 & 0.4300 \end{bmatrix}$$

Note, it is no accident that the last entry,  $\Sigma_t^2 - \Sigma_{s_0}^{2 \rightarrow 2} = 0.4300 = \Sigma_a^2$ . The diffusion matrix for a  $P_1$  approximation is defined as:

$$\overline{D}^{10} = \overline{D}^{11} = D = \left\{ (3) \begin{bmatrix} \Sigma_t^1 - \Sigma_{s_1}^{1 \rightarrow 1} & -\Sigma_{s_1}^{2 \rightarrow 1} \\ -\Sigma_{s_1}^{1 \rightarrow 2} & \Sigma_t^2 - \Sigma_{s_1}^{2 \rightarrow 2} \end{bmatrix} \right\}^{-1}$$

$$3 \left( \Sigma_t^1 - \Sigma_{s_1}^{1 \rightarrow 1} \right) = 3 (0.2398 - 0.0)$$

$$3 \left( \Sigma_t^2 - \Sigma_{s_1}^{2 \rightarrow 2} \right) = 3 (0.6410 - 0.0)$$

Therefore;

$$D = \begin{bmatrix} 0.7194 & 0.0000 \\ 0.0000 & 1.9230 \end{bmatrix}^{-1} = \begin{bmatrix} 1.3900 & 0.0000 \\ 0.0000 & 0.5200 \end{bmatrix}$$

Material 2:

$$\Sigma_t^1 - \Sigma_{s_0}^{1 \rightarrow 1} = 0.2801 - 0.2641$$

$$- \Sigma_{s_0}^{1 \rightarrow 2} = -0.006$$

$$- \Sigma_{s_0}^{2 \rightarrow 1} = 0.0$$

$$\Sigma_t^2 - \Sigma_{s_0}^{2 \rightarrow 2} = 0.4762 - 0.3462$$

Thus:

$$\Sigma^{\infty} = \begin{bmatrix} 0.0160 & 0.0000 \\ -0.006 & 0.1300 \end{bmatrix}$$

Note, the last entry,  $\Sigma_t^2 - \Sigma_{s_0}^{2 \rightarrow 2} = 0.1300 = \Sigma_a^2$ . The diffusion matrix for a  $P_1$  approximation is defined as:

$$3 \left( \Sigma_t^1 - \Sigma_{s_1}^{1 \rightarrow 1} \right) = 3 (0.2801 - 0.0)$$

$$3 \left( \Sigma_t^2 - \Sigma_{s_1}^{2 \rightarrow 2} \right) = 3 (0.4762 - 0.0)$$

Therefore;

$$D = \begin{bmatrix} 0.8403 & 0.0000 \\ 0.0000 & 1.4286 \end{bmatrix}^{-1} = \begin{bmatrix} 1.1901 & 0.0000 \\ 0.0000 & 0.7000 \end{bmatrix}$$



The FEMP codes also calculate the diffusion lengths and mean free paths for each material and each group. For 1 group theory, the diffusion length is defined as:

$$L = \sqrt{\frac{D}{\Sigma_a}} \quad \text{and} \quad D = \frac{1}{3 \Sigma_s (1 - \bar{\mu}_0)}$$

Note for our thermal group,  $\Sigma_t^2 - \Sigma_{s_0}^{2 \rightarrow 2} = \Sigma_a^2$ . Here, we define

$$D_g = \frac{1.0}{3 (\Sigma_t^g - \Sigma_{s_1}^{g \rightarrow g})}$$

Then,

$$L_g = \sqrt{\frac{\frac{1.0}{3 (\Sigma_t^g - \Sigma_{s_1}^{g \rightarrow g})}}{\Sigma_t^g - \Sigma_{s_0}^{g \rightarrow g}}} = \sqrt{\frac{1.0}{3 (\Sigma_t^g - \Sigma_{s_1}^{g \rightarrow g}) (\Sigma_t^g - \Sigma_{s_0}^{g \rightarrow g})}}$$

The mean free paths are calculated by the FEMP codes as:

$$\lambda_g = \frac{1.0}{\Sigma_t^g}$$

The MFP values yield the sensitivity for the spatial mesh spacing in the FEMP codes.

Material 1:

$$D_1 = \frac{1.0}{3 (\Sigma_t^1 - \Sigma_{s_1}^{1 \rightarrow 1})} = \frac{1.0}{3 (0.2398 - 0.000)} = 1.3900$$

Note, this is the D(1,1) entry in the diffusion matrix.

$$L_1 = \sqrt{\frac{D_1}{\Sigma_t^1 - \Sigma_{s_0}^{1 \rightarrow 1}}} = \sqrt{\frac{1.3900}{0.2398 - 0.2148}} = \sqrt{\frac{1.3900}{0.0250}} = 7.4565$$

Note the removal cross section for group 1,  $\Sigma_r^1 = 0.0250$ .

$$\lambda_1 = \frac{1.0}{\Sigma_t^1} = \frac{1.0}{0.2398} = 4.1701$$

$$D_2 = \frac{1.0}{3 (\Sigma_t^2 - \Sigma_{s_1}^{2 \rightarrow 2})} = \frac{1.0}{3 (0.6410 - 0.000)} = 0.5200$$

Note, this is the D(2,2) entry in the diffusion matrix.

$$L_2 = \sqrt{\frac{D_2}{\Sigma_t^2 - \Sigma_{s_0}^{2 \rightarrow 2}}} = \sqrt{\frac{0.5200}{0.6410 - 0.2110}} = \sqrt{\frac{0.5200}{0.4300}} = 1.0997$$

Note the removal cross section for group 2,  $\Sigma_r^2 = 0.4300 = \Sigma_a^2$ .

$$\lambda_2 = \frac{1.0}{\Sigma_t^2} = \frac{1.0}{0.6410} = 1.5601$$

Material 2:

$$D_1 = \frac{1.0}{3 (\Sigma_t^1 - \Sigma_{s_1}^{1 \rightarrow 1})} = \frac{1.0}{3 (0.2801 - 0.000)} = 1.1901$$

Note, this is the D(1,1) entry in the diffusion matrix.

$$L_1 = \sqrt{\frac{D_1}{\Sigma_t^1 - \Sigma_{s_0}^{1 \rightarrow 1}}} = \sqrt{\frac{1.1901}{0.2801 - 0.2641}} = \sqrt{\frac{1.1901}{0.0160}} = 8.6243$$

Note the removal cross section for group 1,  $\Sigma_r^1 = 0.0160$ .

$$\lambda_1 = \frac{1.0}{\Sigma_t^1} = \frac{1.0}{0.2801} = 3.5702$$

$$D_2 = \frac{1.0}{3 (\Sigma_t^2 - \Sigma_{s_1}^{2 \rightarrow 2})} = \frac{1.0}{3 (0.4762 - 0.000)} = 0.7000$$

Note, this is the D(2,2) entry in the diffusion matrix.

$$L_2 = \sqrt{\frac{D_2}{\Sigma_t^2 - \Sigma_{s_0}^{2 \rightarrow 2}}} = \sqrt{\frac{0.7000}{0.4762 - 0.3462}} = \sqrt{\frac{0.7000}{0.1300}} = 2.3205$$

Note the removal cross section for group 2,  $\Sigma_r^2 = 0.1300 = \Sigma_a^2$ .

$$\lambda_2 = \frac{1.0}{\Sigma_t^2} = \frac{1.0}{0.4762} = 2.1000$$

Attached are FEMP2D and FMP2DT input decks showing the 20\*\*, 21\*\*, and 22\*\* array input for the TWIGL problem.

# FEMP2D Sample Input Deck (See FEMP2D Manual for details.)

X-Z Slab Problem: FEMP2D: TWIGL mesh spacing.	TITLE
1\$S	
1	NGEOM
3	NOUTR
0	MADJ
1	LPN
2	NMAT
2	NNG
0	NPG
1	MPN
0	IHT
0	IHS
0	LTBL
2	MTL
2	MCRD
0	MANSN
0	MAMPX
1	NBYTE
21	NX
4	NY
5	NZONE
0	IB(1)
0	IB(2)
0	IB(3)
0	IB(4)
2	ISTR
4	KSOLV
500	ITMX1
200	ITMX3
0	IACC
0	NPOW
0	NUPS
0	NS
1	IPX
38	NPOUT
1	IPFLX
0	NRF
2**	
1.0E-6	EPS
1.0E-5	EPSK
1.0	XK
8.37702E+16	SNORM
T	
10\$S	(Material Numbers)
1 2	
11\$S	(Nuclide Numbers)
1 2	
12**	(Number Densities)
1.0 1.0	
13\$S	(Nuclide IDs)
1 2	
14**	(Prompt Chi Spectrum)
1.0	$\chi_p^1$
0.0	$\chi_p^5$
17**	(Group Velocities)
5.0E+06	$v_1$
2.0E+05	$v_2$
20**	Material 1
0.2398	$\Sigma_1^1$
0.6410	$\Sigma_1^2$
2.555562E-02	$\nu\Sigma_1^1$
7.325943E-01	$\nu\Sigma_1^2$
0.0	$\Sigma_a^1$
0.43	$\Sigma_a^2$
1.0	$\chi_p^1$

0.0	$x_p^2$
21**	
0.2148	$\Sigma_{s_0}^{1-1}$
0.006	$\Sigma_{s_0}^{1-2}$
0.0	$\Sigma_{s_0}^{2-1}$
0.2110	$\Sigma_{s_0}^{2-2}$
22**	
0.0	$(3)\Sigma_{s_1}^{1-1}$
0.0	$(3)\Sigma_{s_1}^{1-2}$
0.0	$(3)\Sigma_{s_1}^{2-1}$
0.0	$(3)\Sigma_{s_1}^{2-2}$
T	
20**	Material 2
0.2801	$\Sigma_t^1$
0.4762	$\Sigma_t^2$
5.11112E-03	$\nu\Sigma_f^1$
8.518539E-02	$\nu\Sigma_f^2$
0.0	$\Sigma_a^1$
0.13	$\Sigma_a^2$
1.0	$x_p^1$
0.0	$x_p^2$
21**	
0.2641	$\Sigma_{s_0}^{1-1}$
0.006	$\Sigma_{s_0}^{1-2}$
0.0	$\Sigma_{s_0}^{2-1}$
0.3462	$\Sigma_{s_0}^{2-2}$
22**	
0.0	$(3)\Sigma_{s_1}^{1-1}$
0.0	$(3)\Sigma_{s_1}^{1-2}$
0.0	$(3)\Sigma_{s_1}^{2-1}$
0.0	$(3)\Sigma_{s_1}^{2-2}$
T	
30**	X Points
0.0 10.0 20.0 30.0 40.0 50.0	
60.0 70.0 80.0 90.0 100.0 110.0	
120.0 130.0 140.0 150.0 160.0 170.0	
180.0 190.0 200.0	
31**	Y Points
0.0 14.142 28.284 42.426	
34\$\$	
1 1 1 2 2 2 2 3 3 3 3 3 4 4 4 4 5 5 5	
1 1 1 2 2 2 2 3 3 3 3 3 4 4 4 4 5 5 5	
1 1 1 2 2 2 2 3 3 3 3 3 4 4 4 4 5 5 5	
35**	
F0.0	
36**	X Print
10.0 20.0 30.0 40.0 50.0	
60.0 70.0 80.0 90.0 100.0 110.0	
120.0 130.0 140.0 150.0 160.0 170.0	
180.0 190.0	
10.0 20.0 30.0 40.0 50.0	
60.0 70.0 80.0 90.0 100.0 110.0	
120.0 130.0 140.0 150.0 160.0 170.0	
180.0 190.0	
37**	Y Print
14.142 14.142 14.142 14.142 14.142 14.142	
14.142 14.142 14.142 14.142 14.142 14.142	
14.142 14.142 14.142 14.142 14.142 14.142	
14.142	
28.284 28.284 28.284 28.284 28.284 28.284	
28.284 28.284 28.284 28.284 28.284 28.284	
28.284 28.284 28.284 28.284 28.284 28.284	
28.284	
T	

# FMP2DT Sample Input Deck (See FMP2DT Manual for details.)

X-Z TWIGL Problem: (FMP2DT-run; TWIGL mesh)	TITLE
1\$\$\$	
1	NGEOM
2	NINT
1	ICOLD
6	LAM
3	NOUTR
0	MADJ
1	LPN
3	NMAT
2	NNG
0	NPG
1	MPN
0	IHT
0	IHS
0	LTBL
3	MTL
3	MCRD
0	MANSN
0	MAMPX
1	NBYTE
21	NX
4	NY
5	NZONE
0	IB(1)
0	IB(2)
0	IB(3)
0	IB(4)
2	ISTRT
4	KSOLV
500	ITMX1
200	ITMX3
0	IACC
0	NPOW
6	NUPS
1	IPX
33	NPOUT
1	IPFLX
0	NRF
0	IBAL
2**	
0.0	TSTRT
1.0E-3	EPS
1.0E-4	EPSK
1.026358	XK
8.37702E+16	SNORM
T	
5\$\$\$	(Material Numbers)
1 2 3	
6\$\$\$	(Nuclide Numbers)
1 2 3	
7**	(Number Densities)
1.0 1.0 1.0	
8\$\$\$	(Nuclide Ids)
1 2 3	
9**	(Prompt Chi Spectrum)
1.0	$\chi_p^1$
0.0	$\chi_p^2$
12**	(Group Velocities)
5.0E+06	$v_1$
2.0E+05	$v_2$
13**	(Delayed Neutron Fractions)
2.4700E-04	$\beta_1$
1.3845E-03	$\beta_2$
1.2220E-03	$\beta_3$

2.6455E-03  
 8.3200E-04  
 1.6900E-04  
 14\*\*  
 0.0127  
 0.0317  
 0.1150  
 0.3110  
 1.4000  
 3.8700  
 15\*\*  
 1.0  
 1.0  
 1.0  
 1.0  
 1.0  
 1.0  
 0.0  
 0.0  
 0.0  
 0.0  
 0.0  
 0.0  
 0.0  
 0.0  
 20\*\*  
 0.2398  
 0.6410  
 2.555562E-02  
 7.325943E-01  
 0.0  
 0.43  
 1.0  
 0.0  
 21\*\*  
 0.2148  
 0.006  
 0.0  
 0.2110  
 22\*\*  
 0.0  
 0.0  
 0.0  
 0.0  
 T  
 20\*\*  
 0.2801  
 0.4762  
 5.11112E-03  
 8.518539E-02  
 0.0  
 0.13  
 1.0  
 0.0  
 21\*\*  
 0.2641  
 0.006  
 0.0  
 0.3462  
 22\*\*  
 0.0  
 0.0  
 0.0  
 0.0

$\beta_4$   
 $\beta_5$   
 $\beta_6$   
 (Decay Constants)  
 $\lambda_1$   
 $\lambda_2$   
 $\lambda_3$   
 $\lambda_4$   
 $\lambda_5$   
 $\lambda_6$   
 (Delayed Chi Spectrum)  
 $x_1^1$   
 $x_2^1$   
 $x_3^1$   
 $x_4^1$   
 $x_5^1$   
 $x_6^1$   
 $x_1^2$   
 $x_2^2$   
 $x_3^2$   
 $x_4^2$   
 $x_5^2$   
 $x_6^2$   
 Material 1  
 $\Sigma_1^1$   
 $\Sigma_2^1$   
 $\nu\Sigma_1^1$   
 $\nu\Sigma_2^1$   
 $\Sigma_1^2$   
 $\Sigma_2^2$   
 $\Sigma_{10}^1-1$   
 $\Sigma_{10}^1-2$   
 $\Sigma_{10}^2-1$   
 $\Sigma_{10}^2-2$   
 $(3)\Sigma_{11}^1-1$   
 $(3)\Sigma_{11}^1-2$   
 $(3)\Sigma_{11}^2-1$   
 $(3)\Sigma_{11}^2-2$   
 Material 2  
 $\Sigma_1^1$   
 $\Sigma_2^1$   
 $\nu\Sigma_1^1$   
 $\nu\Sigma_2^1$   
 $\Sigma_1^2$   
 $\Sigma_2^2$   
 $\Sigma_{10}^1-1$   
 $\Sigma_{10}^1-2$   
 $\Sigma_{10}^2-1$   
 $\Sigma_{10}^2-2$   
 $(3)\Sigma_{11}^1-1$   
 $(3)\Sigma_{11}^1-2$   
 $(3)\Sigma_{11}^2-1$   
 $(3)\Sigma_{11}^2-2$

T	
20**	Material 3
0.2398	$\Sigma_1^1$
0.6410	$\Sigma_1^2$
2.555562E-02	$\nu \Sigma_1^1$
7.325943E-01	$\nu \Sigma_1^2$
0.0	$\Sigma_1^1$
0.43	$\Sigma_1^2$
1.0	$\chi_p^1$
0.0	$\chi_p^2$
21**	
0.2148	$\Sigma_{10}^{1 \rightarrow 1}$
0.006	$\Sigma_{10}^{1 \rightarrow 2}$
0.0	$\Sigma_{10}^{2 \rightarrow 1}$
0.2110	$\Sigma_{10}^{2 \rightarrow 2}$
22**	
0.0	$(3)\Sigma_{11}^{1 \rightarrow 1}$
0.0	$(3)\Sigma_{11}^{1 \rightarrow 2}$
0.0	$(3)\Sigma_{11}^{2 \rightarrow 1}$
0.0	$(3)\Sigma_{11}^{2 \rightarrow 2}$
T	
30**	X Points
0.0 10.0 20.0 30.0 40.0 50.0	
60.0 70.0 80.0 90.0 100.0 110.0	
120.0 130.0 140.0 150.0 160.0 170.0	
180.0 190.0 200.0	
31**	Y Points
0.0 14.142 28.284 42.426	
34\$\$	
1 1 1 2 2 2 2 3 3 3 3 3 4 4 4 4 5 5 5	
1 1 1 2 2 2 2 3 3 3 3 3 4 4 4 4 5 5 5	
1 1 1 2 2 2 2 3 3 3 3 3 4 4 4 4 5 5 5	
35**	
F0.0	
36**	X Print
10.0 20.0 30.0 40.0 50.0	
60.0 70.0 80.0 90.0 100.0 110.0	
120.0 130.0 140.0 150.0 160.0 170.0	
180.0 190.0	
10.0 20.0 30.0 40.0 50.0	
60.0 70.0 80.0 90.0 100.0 110.0	
120.0 130.0 140.0 150.0 160.0 170.0	
180.0 190.0	
37**	Y Print
14.142 14.142 14.142 14.142 14.142 14.142	
14.142 14.142 14.142 14.142 14.142 14.142	
14.142 14.142 14.142 14.142 14.142 14.142	
14.142	
28.284 28.284 28.284 28.284 28.284 28.284	
28.284 28.284 28.284 28.284 28.284 28.284	
28.284 28.284 28.284 28.284 28.284 28.284	
28.284	
T	
40\$\$	INT=1
0	NS
1	NTIM
0	IXSEC
41**	
0.005	TFIN
T	
40\$\$	INT=2
0	NS
5	NTIM
1	IXSEC
41**	
0.010	TFIN



T  
 20\*\*  
 0.0  
 0.0  
 0.0  
 0.0  
 0.0  
 -0.002  
 0.0  
 0.0  
 21\*\*  
 0.0  
 0.0  
 0.0  
 0.002  
 22\*\*  
 F0.0  
 T  
 20\*\*  
 F0.0  
 21\*\*  
 F0.0  
 22\*\*  
 F0.0  
 T  
 20\*\*  
 F0.0  
 21\*\*  
 F0.0  
 22\*\*  
 F0.0  
 T  
 20\*\*  
 0.0  
 0.0  
 0.0  
 0.0  
 0.0  
 -0.002  
 0.0  
 0.0  
 21\*\*  
 0.0  
 0.0  
 0.0  
 0.002  
 22\*\*  
 F0.0  
 T  
 20\*\*  
 F0.0  
 21\*\*  
 F0.0  
 22\*\*  
 F0.0  
 T  
 20\*\*  
 F0.0  
 21\*\*  
 F0.0  
 22\*\*  
 F0.0  
 T  
 20\*\*  
 0.0  
 0.0

Material 1 (ITT=1)

$\Sigma_i^1$   
 $\Sigma_i^2$   
 $\nu \Sigma_f^1$   
 $\nu \Sigma_f^2$   
 $\Sigma_a^1$   
 $\Sigma_a^2$   
 $\chi_p^1$   
 $\chi_p^2$

$\Sigma_{s0}^{1-1}$   
 $\Sigma_{s0}^{1-2}$   
 $\Sigma_{s0}^{2-1}$   
 $\Sigma_{s0}^{2-2}$

Material 2 (ITT=1)

Material 3 (ITT=1)

Material 1 (ITT=2)

$\Sigma_i^1$   
 $\Sigma_i^2$   
 $\nu \Sigma_f^1$   
 $\nu \Sigma_f^2$   
 $\Sigma_a^1$   
 $\Sigma_a^2$   
 $\chi_p^1$   
 $\chi_p^2$

$\Sigma_{s0}^{1-1}$   
 $\Sigma_{s0}^{1-2}$   
 $\Sigma_{s0}^{2-1}$   
 $\Sigma_{s0}^{2-2}$

Material 2 (ITT=2)

Material 3 (ITT=2)

Material 1 (ITT=3)

$\Sigma_i^1$   
 $\Sigma_i^2$

0.0  
 0.0  
 0.0  
 -0.002  
 0.0  
 0.0  
 21\*\*  
 0.0  
 0.0  
 0.0  
 0.002  
 22\*\*  
 F0.0  
 T  
 20\*\*  
 F0.0  
 21\*\*  
 F0.0  
 22\*\*  
 F0.0  
 T  
 20\*\*  
 F0.0  
 21\*\*  
 F0.0  
 22\*\*  
 F0.0  
 T  
 20\*\*  
 0.0  
 0.0  
 0.0  
 0.0  
 0.0  
 -0.002  
 0.0  
 0.0  
 21\*\*  
 0.0  
 0.0  
 0.0  
 0.002  
 22\*\*  
 F0.0  
 T  
 20\*\*  
 F0.0  
 21\*\*  
 F0.0  
 22\*\*  
 F0.0  
 T  
 20\*\*  
 F0.0  
 21\*\*  
 F0.0  
 22\*\*  
 F0.0  
 T  
 20\*\*  
 0.0  
 0.0  
 0.0  
 0.0  
 0.0  
 -0.002

$\nu \Sigma_1^1$   
 $\nu \Sigma_1^2$   
 $\Sigma_a^1$   
 $\Sigma_a^2$   
 $X_p^1$   
 $X_p^2$

$\Sigma_{s_0}^{1-1}$   
 $\Sigma_{s_0}^{1-2}$   
 $\Sigma_{s_0}^{2-1}$   
 $\Sigma_{s_0}^{2-2}$

Material 2 (ITT=3)

Material 3 (ITT=3)

Material 1 (ITT=4)

$\Sigma_1^1$   
 $\Sigma_1^2$   
 $\nu \Sigma_1^1$   
 $\nu \Sigma_1^2$   
 $\Sigma_a^1$   
 $\Sigma_a^2$   
 $X_p^1$   
 $X_p^2$

$\Sigma_{s_0}^{1-1}$   
 $\Sigma_{s_0}^{1-2}$   
 $\Sigma_{s_0}^{2-1}$   
 $\Sigma_{s_0}^{2-2}$

Material 2 (ITT=4)

Material 3 (ITT=4)

Material 1 (ITT=5)

$\Sigma_1^1$   
 $\Sigma_1^2$   
 $\nu \Sigma_1^1$   
 $\nu \Sigma_1^2$   
 $\Sigma_a^1$   
 $\Sigma_a^2$

0.0  
 0.0  
 21\*\*  
 0.0  
 0.0  
 0.0  
 0.002  
 22\*\*  
 F0.0  
 T  
 20\*\*  
 F0.0  
 21\*\*  
 F0.0  
 22\*\*  
 F0.0  
 T  
 20\*\*  
 F0.0  
 21\*\*  
 F0.0  
 22\*\*  
 F0.0  
 T

$x_p^1$   
 $x_p^2$   
 $x_p^3$   
 $\Sigma_{s_0}^{1 \rightarrow 1}$   
 $\Sigma_{s_0}^{1 \rightarrow 2}$   
 $\Sigma_{s_0}^{2 \rightarrow 1}$   
 $\Sigma_{s_0}^{2 \rightarrow 2}$

Material 2 (ITT=5)

Material 3 (ITT=5)

Note: ITT=TIME INTERVAL; ITT=1,..., NINT

INT=TIME STEP IN THAT INTERVAL; INT=1,..., NTIM

## References

- [Ref. 1] Henry, Allan F. **Nuclear-Reactor Analysis**. Cambridge: The MIT Press, 1975.
- [Ref. 2] Davison, B. **Neutron Transport Theory**. Oxford, Great Britain: Oxford University Press, Amen House, London E.C.4, 1957.
- [Ref.3] Kardestuncer, H. and Norrie, D. H. **Finite Element Handbook**. New York: McGraw-Hill Book Company, 1987.
- [Ref. 4] Duderstadt, James J. and Martin, William R. **Transport Theory**. New York: John Wiley & Sons, Inc., 1979.
- [Ref. 5] Pauling, Linus and Wilson, E. Bright. **Introduction to Quantum Mechanics with Applications to Chemistry**. New York: McGraw-Hill Book Company, Inc., 1935.
- [Ref. 6] Whittaker, E. T. and Watson, G. N. **A Course of Modern Analysis**. Cambridge: At the University Press, 1950.
- [Ref. 7] Lewis, E. E. and Miller, W. F., Jr. **Computational Methods of Neutron Transport**. New York: John Wiley & Sons, 1984.
- [Ref. 8] Bell, George I. and Glasstone, Samuel. **Nuclear Reactor Theory**. Malabar, Florida: Robert E. Krieger Publishing Co., Inc., 1970.
- [Ref. 9] Weinberg, Alvin M. and Wigner, Eugene P. **The Physical Theory of Neutron Chain Reactors**. Chicago: The University of Chicago Press, 1958.
- [Ref. 10] Duderstadt, James J. and Hamilton, L. J. **Nuclear Reactor Analysis**. New York: Wiley, 1976.

- [Ref. 11] Fletcher, J. K. *The Solution of the Multigroup Neutron Transport Equation Using Spherical Harmonics*. Nuclear Science and Engineering: 84, 33-46 (1983).
- [Ref. 12] O'Dell, R. Douglas and Alcouffe, Raymond E. *Transport Calculations for Nuclear Analyses: Theory and Guidelines for Effective Use of Transport Codes*. LA-10983-MS, Los Alamos National Laboratory, September 1987.
- [Ref. 13] Huebner, Kenneth H. **The Finite Element Method for Engineers**. Second Edition, New York: John Wiley & Sons, 1982.
- [Ref. 14] Nelsen, James M. *Derivation of Finite Element Conductivity and Capacitance Matrices for 2- and 3-Dimensional Conduction Heat Transfer*. SAND85-0479 TTC 0545, Sandia National Laboratories, 1985.
- [Ref. 15] Meghreblian, Robert V. and Holmes, David K. **Reactor Analysis**. New York: McGraw-Hill Book Company, 1960.
- [Ref. 16] Marshak, R. E. *Note on the Spherical Harmonic Method As Applied to the Milne Problem for a Sphere*. Phys. Rev., 71, 443-6 (April 1, 1947).
- [Ref. 17] Greenspan, H. Kelber, C. N., and Okrent, D. **Computing Methods in Reactor Physics**. New York: Gordon and Breach Science Publishers, 1968.
- [Ref. 18] Golub, Gene H. and Van Loan, Charles F. **Matrix Computations**. The Johns Hopkins University Press, 1983.
- [Ref. 19] Dean, Virginia Ann Frederick. *The Application of Perturbation Theory to a Small Epithermal Reactor*. Ph.D. dissertation, Nuclear Engineering, The University of New Mexico, 1988.
- [Ref. 20] Leon, Steven J. **Linear Algebra With Applications**. New York: Macmillan Publishing Co., Inc., 1980.

- [Ref. 21] Strang, Gilbert and Fix, George J. **An Analysis of the Finite Element Method**. Englewood Cliffs, New Jersey: Prentice-Hall, Inc., 1973.
- [Ref. 22] Fletcher, J. K. *The solution of the multigroup neutron transport equation using spherical harmonics*. TRG-Report-2 547 (R), United Kingdom Atomic Energy Authority, 1974.
- [Ref. 23] Hobson, E. W. **The Theory of Spherical and Ellipsoidal Harmonics**. New York: Chelsea Publishing Company, 1955.
- [Ref. 24] Barattino, John William. *Coupled Radiation Transport/Thermal Analysis of the Radiation Shield for a Space Nuclear Reactor*. Ph.D. dissertation, Nuclear Engineering, The University of New Mexico, 1985. Technical Report, DTIC, AD-A158 180.
- [Ref. 25] Gallup, Donald Robert. *TDF1D: A Time-Dependent, One-Dimensional, Radiation Transport Code*. Ph.D. dissertation, The University of New Mexico.
- [Ref. 26] Lambert, J. D. **Computational Methods in Ordinary Differential Equations**. New York: John Wiley & Sons, 1983.
- [Ref. 27] Arfken, George. **Mathematical Methods for Physicists**. New York: Academic Press, Inc., 1985.
- [Ref. 28] Yasinsky, J. B., Natelson, M., and Hageman, L. A. *TWIGL - A Program To Solve the Two-Dimensional, Two-Group, Space-Time Neutron Diffusion Equations with Temperature Feedback*. Technical Report, WAPD-TM-743, Federal Scientific and Technical Information. February 1968.

- [Ref. 29] Ganapol, B. D., and McKenty, P. W. *The Generation of Time-Dependent Neutron Transport Solutions in Infinite Media*. Nuclear Science and Engineering: 64, 317-331 (1977).
- [Ref. 30] Lewins, Jeffery. *Nuclear Reactor Kinetics and Control*. New York: Pergamon Press, 1978.
- [Ref. 31] Keepin, G. R. *Physics of Nuclear Kinetics*. Reading, Massachusetts: Addison-Wesley, 1965.
- [Ref. 32] Renken, James H. *Prediction of Time-Dependent Neutron Fluxes Encountered in Pulsed-Neutron Uranium Logging Experiments*. Nuclear Technology, Vol. 31 October 1976.
- [Ref. 33] Press, William H., Flannery, Brian P., Teukolsky, Saul A., and Vetterling, William T. *Numerical Recipes; The Art of Scientific Computing*. New York: Cambridge University Press, 1986.
- [Ref. 34] Watt, B. E. Phys. Rev., 87, 1037. (1952).
- [Ref. 35] L. Cranberg, *et al.* Phys. Rev., 103, 662. (1956).
- [Ref. 36] B. P. Blizard, *et al.* *Engineering Compendium on Radiation Shielding*. Volume I. New York: Springer-Verlan, 1968.
- [Ref. 37] Hornbeck, Robert W. *Numerical Methods*. Englewood Cliffs, New Jersey: Prentice-Hall, Inc., 1975.